



**HAL**  
open science

# Statistics of dislocations at low temperature in pure metals with body centered cubic symmetry

Anshuman Choudhury

► **To cite this version:**

Anshuman Choudhury. Statistics of dislocations at low temperature in pure metals with body centered cubic symmetry. General Physics [physics.gen-ph]. Université Paris Saclay (COMUE), 2018. English. NNT : 2018SACLS569 . tel-02100533

**HAL Id: tel-02100533**

**<https://theses.hal.science/tel-02100533>**

Submitted on 16 Apr 2019

**HAL** is a multi-disciplinary open access archive for the deposit and dissemination of scientific research documents, whether they are published or not. The documents may come from teaching and research institutions in France or abroad, or from public or private research centers.

L'archive ouverte pluridisciplinaire **HAL**, est destinée au dépôt et à la diffusion de documents scientifiques de niveau recherche, publiés ou non, émanant des établissements d'enseignement et de recherche français ou étrangers, des laboratoires publics ou privés.

NNT: 2018SACLS569

# Statistics of dislocations at low temperature in pure metals with body centered cubic symmetry

Thèse de doctorat de l'Université Paris-Saclay  
préparée à l'Université Paris-Sud

École doctorale n°564 Physique en Ile-de-France (EDPIF)  
Spécialité de doctorat : Physique

Thèse présentée et soutenue à Saclay, le 11 Décembre 2018, par

**Anshuman Choudhury**

Composition du Jury :

|   |                    |
|---|--------------------|
| Jérôme Creuze<br>Professeur, ICMMO, Université Paris-Sud                              | Président          |
| Daniel Caillard<br>Directeur de Recherche, CEMES (CNRS), Toulouse                     | Rapporteur         |
| Laurent Pizzagalli<br>Directeur de Recherche, Institut Pprime, Université de Poitiers | Rapporteur         |
| Laurent Proville<br>Ingénieur de Recherche, CEA Saclay (SRMP)                         | Directeur de thèse |

## Acknowledgements

I would like to thank the jury members for presiding over my PhD defense and for their invaluable insights and inputs. I would like to express my immense gratitude to my supervisor and thesis director, Dr Laurent Proville for giving me the opportunity to work under him in such a wonderful project, for his guidance, insight and patience. I would also like to thank the chief of my laboratory Dr Jean-Luc Bechade for his regular interactions to check our progress and his ever motivating words. I also thank Patricia Matysiak, the secretary of our lab for helping with all the complicated administrative processes and for providing information on different topics whenever I have approached her.

I would like to thank my friend Ashish Rajyaguru who first helped me with all the information, links and fine details associated with the process of applying for a PhD in France and for his constant encouragement during the course of my PhD. I would like to thank my friends and fellow PhD students from the lab namely Marie Landeiro Dos Reis, Elric Barbe, Anton Schneider, Denise Carpentier without whose regular help I would be handicapped with my very limited knowledge of the French language. I would also like to express my gratitude to my soul-friend Veronica Atzei and to Sandrina, my French professor for their constant help, encouragement and for all the good memories.

I would like to thank the few people I had confided in and my doctor (Psychiatrist), Dr Miloud Brahim for helping me in overcoming aggravated anxiety and depression.

Thanks honestly and sincerely to each and every person (young, old, children) who I have ever met/exchanged words/spent time, at any stage of my life. I have learned something from all of you.

Finally, I can't thank enough my parents for everything they have done for me. I can't express my gratitude in words.



## Dedication

Dedicated to Mrs Nobody (Nirala Choudhury), my mother and Mr Nobody (Nitya Choudhury), my father, parents of Mr Somebody now.

Dedicated also to the millions of middle/lower-middle class Indian parents who without the liberty of engaging in most materialistic comforts (considered basic in global terms), work tirelessly and selflessly their entire lives, only for a better future for their children.

Dedicated to the great and majestic city of Paris. I have re-found my soul here and found finally, the purpose of my life.

Dedicated finally to the undying human spirit that has helped humanity fight/overcome famine, drought, poverty, oppression, wars and more modern problems like economic recession, marital complicacies, stress related disorders like anxiety and depression amongst many others.



# Contents

|  |           |
|--|-----------|
| <b>Acknowledgements</b>  | <b>i</b>  |
| <b>1 Introduction</b>  | <b>1</b>  |
| 1.1 Historical background and related terminologies . . . . .                        | 2         |
| 1.1.1 Dislocation glide mechanism . . . . .  | 3         |
| 1.1.2 Experimental and Computational observations of the past years . . . . .        | 6         |
| 1.2 Motivation behind the thesis: experimental observations of D. Caillard . . . . . | 9         |
| <b>2 Description of Computations</b>   | <b>17</b> |
| 2.1 Description of the model for interaction between atoms . . . . .                 | 17        |
| 2.1.1 EAM : Embedded Atom Method interatomic potentials . . . . .                    | 19        |
| 2.2 Construction of Simulation Cells . . . . .                                       | 22        |
| 2.3 Algorithms used for our computations . . . . .                                   | 26        |
| 2.3.1 Quenching - Relaxation of the simulation cell . . . . .                        | 27        |
| 2.3.2 Molecular Dynamics - Verlet and Velocity Verlet algorithm . . . . .            | 28        |
| 2.3.3 NEB method to estimate the MEP . . . . .                                       | 30        |
| 2.4 Simulation cell extension . . . . .  | 34        |

|          |  |           |
|----------|--|-----------|
| <b>3</b> | <b>Atomic scale study of the screw dislocation glide in bcc Iron</b>   | <b>38</b> |
| 3.1      | Kink propagation in standard Peierls Nabarro mechanism . . . . .   | 38        |
| 3.1.1    | Simulations for $T = (0 + \epsilon)$ K . . . . .   | 39        |
| 3.1.2    | Simulations at $T = 5$ K and $T = 10$ K . . . . .  | 43        |
| 3.1.3    | Plot of kink velocity as a function of time . . . . .  | 45        |
| 3.2      | Kink propagation at high stress level . . . . .  | 54        |
| 3.3      | Investigation of the energetics responsible for jerky motion . . . . .   | 59        |
| <b>4</b> | <b>Atomistic scale study of the screw dislocation glide in bcc Tungsten</b>                                    | <b>64</b> |
| 4.1      | Introduction . . . . .   | 64        |
| 4.2      | Details of the simulation cell, algorithms, and the different steps of simulations .                           | 66        |
| 4.2.1    | Simulation cell . . . . .  | 66        |
| 4.2.2    | Quenching and NEB calculations . . . . .   | 66        |
| 4.2.3    | The extended simulation cell . . . . .   | 67        |
| 4.2.4    | The EAM potential used for our simulations . . . . .   | 69        |
| 4.3      | MD simulation results . . . . .  | 71        |
| 4.3.1    | Simulations at $T = (0 + \epsilon)$ K . . . . .  | 72        |
| 4.3.2    | Simulations with the application of temperature . . . . .  | 74        |
| 4.4      | Plot of kink pair formation enthalpy and kinetic energy of traveling kinks against<br>applied stress . . . . . | 74        |
| 4.5      | Comparison of the jerky motions observed in bcc iron and tungsten . . . . .                                    | 76        |
| 4.6      | Experimental observations of Dr. Caillard for Tungsten . . . . .   | 76        |

|          |  |           |
|----------|--|-----------|
| 4.7      | Comparison of our simulations with Dr. Caillards experimental observations . . | 78        |
| <b>5</b> | <b>Conclusion</b>  | <b>79</b> |
| 5.1      | Summary of results . . . . .   | 79        |
| 5.2      | Future perspective . . . . .   | 82        |
| <b>6</b> | <b>Resumé</b>  | <b>84</b> |
|          | <b>Bibliography</b>  | <b>90</b> |



# List of Tables

2.1 Values of the lattice parameter,  $a_0$  and the cohesive forces between the atoms,  
 $E_{coh}$  for different EAMs and as obtained in experiments . . . . . 22



# List of Figures

|     |  |    |
|-----|--|----|
| 1.1 | Sketch of the plan view of a (1 1 0) crystal plane (glide plane) showing the process of kink pair formation along a screw dislocation and stages of kink propagation along the dislocation line which finally results in the glide of the screw dislocation  | 5  |
| 1.2 | Temperature dependence of the yield stress $\tau$ (projected on the most stressed (110) plane) of pure Fe. Tensile tests by Kuramoto et al. [86] (crosses) and Brunner and Diehl [49, 88] (circles), straining axis close to $\langle 148 \rangle$ . The corresponding activation areas, $A$ , are shown in large dashed lines [87] and dotted lines [88].   | 12 |
| 1.3 | Comparison of dislocation kinetics at 110 K and 300 K. (a) At 110 K, dislocation jumps between $t = 0$ and $t = 0.04$ s, and between $t = 0.88$ s and $t = 0.92$ s, whereas no motion occurs between $t = 0.04$ s and $t = 0.88$ s (seen in difference-images). The inset shows that the black/white contrasts of the difference-image are sharp and widely separated, in agreement with a jerky motion with no acceleration/deceleration phases. (b) At 300 K, the moving dislocation has a fuzzy contrast and the black/white contrasts of the difference-image are adjacent, in agreement with a steady motion. | 14 |
| 2.1 | Snapshots of all the essential elements of the simulation cell we used for simulating a $a_0/2[111](\bar{1}10)$ screw dislocation in BCC Fe as considered in [126]   | 25 |

|     |   |    |
|-----|---|----|
| 2.2 | a) Profile of the dislocation in different NEB images. b) Minimum energy path (MEP) between the initial and final dislocation states with the corresponding saddle state. . . . .   | 33 |
| 2.3 | a) Typical NEB simulation cell used to compute the saddle state of the dislocation and b) Extended simulation cell with NEB saddle state placed at the center and straight dislocation segments placed on both sides several times. . . . .   | 35 |
| 2.4 | Left and right kinks attaining steady state velocity at positions that justify the simulation cell extension. . . . .   | 36 |
| 3.1 | Plot of temperature per unit atom as a function of time for two different extended simulation cells i.e. 5 and 7 times the original cell, at different applied shear stresses, $\tau_{yz} = 100$ MPa, $\tau_{yz} = 200$ MPa and $\tau_{yz} = 300$ MPa respectively for temperature close to 0 K i.e. $T = (0 + \epsilon)$ K, for EAM1 [107]. . . . .                  | 40 |
| 3.2 | MD profiles of simulations of kink propagation for temperature close to 0 K, i.e. $T = (0 + \epsilon)$ K for (a) EAM1 [107] performed at an applied shear stress, $\tau_{yz} = 300$ MPa (b) EAM2 [99] performed at an applied shear stress, $\tau_{yz} = 500$ MPa and (c) EAM3 [98] performed at an applied shear stress, $\tau_{yz} = 800$ MPa respectively. . . . . | 42 |
| 3.3 | MD profiles of simulations of kink propagation for temperature, $T = 5$ K for (a) EAM1 [107] performed at an applied shear stress, $\tau_{yz} = 300$ MPa and (b) EAM2 [99] performed at an applied shear stress, $\tau_{yz} = 500$ MPa and (c) EAM3 [98] performed at an applied shear stress, $\tau_{yz} = 800$ MPa respectively. . . . .                            | 44 |
| 3.4 | MD profiles of simulations of kink propagation for temperature, $T = 10$ K for (a) EAM1 [107] performed at an applied shear stress, $\tau_{yz} = 300$ MPa and (b) EAM2 [99] performed at an applied shear stress, $\tau_{yz} = 500$ MPa and (c) EAM3 [98] performed at an applied shear stress, $\tau_{yz} = 800$ MPa respectively. . . . .                           | 45 |

- 3.5 Plot of kink velocity as a function of time for three different temperatures,  $T = (0 + \epsilon)$  K,  $T = 5$  K and  $T = 10$  K for (a) EAM1 [107] at an applied shear stress,  $\tau_{yz} = 300$  MPa, (b) EAM2 [99] at an applied shear stress,  $\tau_{yz} = 500$  MPa and (c) EAM3 [98] at an applied shear stress,  $\tau_{yz} = 800$  MPa. . . . . 46
- 3.6 Asymptotic Kink velocity plotted as a function of increasing applied shear stress for EAM1 [107]. (EAM Chamati et al.) . . . . . 49
- 3.7 MD profiles of simulations for kink propagation with EAM1 [107] showing: (a) Secondary kink pair nucleation at an applied shear stress,  $\tau_{yz} = 450$  MPa and temperature,  $T = (0 + \epsilon)$  K (b) Jerky motion at an applied shear stress,  $\tau_{yz} = 450$  MPa and temperature,  $T = 5$  K (c) Jerky motion at an applied shear stress,  $\tau_{yz} = 400$  MPa and temperature,  $T = 30$  K. . . . . 54
- 3.8 MD profiles of simulations for kink propagation with EAM2 [99] showing Jerky motion (a) at an applied shear stress,  $\tau_{yz} = 600$  MPa and temperature,  $T = (0 + \epsilon)$  K (b) at an applied shear stress,  $\tau_{yz} = 550$  MPa and temperature,  $T = 5$  K and (c) at an applied shear stress,  $\tau_{yz} = 500$  MPa and temperature,  $T = 20$  K. 56
- 3.9 MD profiles of simulations for kink propagation with EAM2 [99] after proper relaxation of the starting unstable profile taken from NEB computations showing: (a) Standard Peierls [9] process at an applied shear stress,  $\tau_{yz} = 600$  MPa and  $T = (0 + \epsilon)$  K (previously Jerky motion was observed instead with these same parameters) (b) Jerky motion at an applied shear stress,  $\tau_{yz} = 650$  MPa (instead of 600 MPa as previously seen) and temperature,  $T = (0 + \epsilon)$  K (c) Jerky motion at an applied shear stress,  $\tau_{yz} = 600$  MPa and temperature,  $T = 30$  K and (d) Jerky motion at an applied shear stress,  $\tau_{yz} = 550$  MPa and temperature,  $T = 30$  K. . . . . 57

- 3.10 MD profiles of simulations for kink propagation with EAM3 [98] showing Jerky motion (a) at an applied shear stress  $\tau_{yz} = 920$  MPa and temperature  $T = (0 + \epsilon)$  K; b) at an applied shear stress  $\tau_{yz} = 875$  MPa and temperature  $T = 25$  K; c) at an applied shear stress  $\tau_{yz} = 850$  MPa and temperature  $T = 30$  K and (d) at an applied shear stress  $\tau_{yz} = 800$  MPa and temperature  $T = 40$  K . . . . . 58
- 3.11 MD profiles of simulations for kink propagation with EAM1 [107] showing Jerky motion at temperature  $T = (0 + \epsilon)$  K ;(a) at an applied shear stress  $\tau_{yz} = 450$  MPa and (b) at an applied shear stress  $\tau_{yz} = 550$  MPa. The initial state of MD is represented by the kinked profile in red, computed by the NEB method. Dashed arrows indicate the distance between the primary kink pair and the second kink pair nucleation. The black arrows are used to point out the instant of occurrence of secondary kink pairs. . . . . 60
- 3.12 Results from NEB computations at different levels of applied shear stresses using EAM1 [107] showing: (a) The MEP undertaken by the 50 NEB images between the initial and the final straight screw dislocation states (b) Different MEPs of the NEB images at different levels of applied shear stress,  $\tau_{yz}$  (c) zoomed in view of (b) showing also the corresponding values of kink-pair formation energies for different values of the applied shear stress,  $\tau_{yz}$  (d) Variation of the kink pair formation energy over the entire range of the applied shear stress for our simulations . . . . . 62
- 3.13 Kinetic energy transfer from kink motion and kink pair activation enthalpy against the applied shear stress  $\tau_{yz}$ . The symbols represent values from atomistic simulations and the curves are according to analytical fits. Blue line : activation enthalpy for the nucleation of a kink pair  $H_{kp}$  ; Red line : steady value of the kinetic energy transfer  $Q_{kp}$ . The analytical fit for the kink pair formation enthalpy is :  $H_{kp} = H_0[1 - (\frac{\tau_{yz}}{\tau_P})^{0.95}]^{1.96}$  and that for the kinetic energy along the dislocation segments is :  $Q_{kp} = 0.03\frac{\tau_{yz}}{\tau_P}$ . . . . . 63

|     |  |    |
|-----|--|----|
| 4.1 | Plot of enthalpy along the minimum energy path for screw dislocations obtained with NEB computations showing : (a) the local maximas corresponding to the kink nucleation at different applied shear stress levels, $\tau_{yz}$ (b) Zoomed in version of the profiles plotted in (a) specifying the energy associated with the kink pair nucleation at different levels of applied shear stress, $\tau_{yz}$ (c) A plot of the variation of the kink-pair energies with the applied shear stress, $\tau_{yz}$ . . . . .  | 68 |
| 4.2 | MD profiles of simulations of kink propagation for temperature close to 0 K, i.e. $T = (0 + \epsilon)$ K for EAM4 [1] performed at an applied shear stress, $\tau_{yz} = 1$ GPa. .   | 71 |
| 4.3 | MD profiles of simulations of kink propagation for temperature close to 0 K, i.e. $T = (0 + \epsilon)$ K for EAM4 [1] performed at an applied shear stress, $\tau_{yz} = 1.54$ GPa.  | 72 |
| 4.4 | MD profiles of simulations of kink propagation for temperature close to 0 K, i.e. $T = 50$ K for EAM4 [1] performed at an applied shear stress, $\tau_{yz} = 1.48$ GPa. .  | 73 |
| 4.5 | Kinetic energy transfer from kink motion against $\tau_{yz}$ . Black line : activation enthalpy for the nucleation of a kink pair $H_{kp}$ ; Red line : steady value of the kinetic energy transfer $Q_{kp}$ . The symbols represent values from atomistic simulations and the curves are according to analytical fits. Blue line : activation enthalpy for the nucleation of a kink pair $H_{kp}$ ; Red line : steady value of the kinetic energy transfer $Q_{kp}$ . The analytical fit for the kink pair formation enthalpy is : $H_{kp} = H_0[1 - (\frac{\tau_{yz}}{\tau_P})^{0.78}]^{1.42}$ and that for the kinetic energy along the dislocation segments is : $Q_{kp} = 0.06\frac{\tau_{yz}}{\tau_P}$ . . . . . | 75 |

5.1 MD profiles of simulations for kink propagation with EAM2 [99] showing: (a) Jerky motion at an applied shear stress,  $\tau_{yz} = 600$  MPa and  $T = (0 + \epsilon)$  K (b) Orientation A [87, 101] of the crystal. (c) Jerky motion at an applied principal stress  $\tau = 999.24$  MPa, resolved shear stress component,  $\tau_{yz} = 500$  MPa, and resolved compressive stress component,  $\tau_{zz} = 482.18$  MPa at temperature,  $T = (0 + \epsilon)$  K and (d) Jerky motion at an applied principal stress  $\tau = 899.31$  MPa, resolved shear stress component,  $\tau_{yz} = 450$  MPa, and resolved compressive stress component,  $\tau_{zz} = 434$  MPa at temperature,  $T = (0 + \epsilon)$  K. . . . . 82

# Chapter 1

## Introduction

With the gradual advent of science and technology over the centuries, engineers all over the world, at different times have deciphered and relied on the individual and distinct nature of matter in order to control the deformation of materials during their use. The most commonly used materials, without an ounce of doubt are the metals owing to their strong structural and mechanical properties. Iron is the most widely used of all the metals, accounting for over 90% of worldwide metal production. Since pure Iron is quite soft, it is most commonly combined with carbon and some other alloying elements to make steel. The addition of other elements can provide steel with other useful qualities. For instance, nickel increases its durability and makes it more resistant to heat and acids, manganese makes it more durable, whereas tungsten helps it maintain hardness at high temperatures. Its low cost and high strength make it indispensable in industrial and engineering applications like structural components for buildings, construction of machinery and machine tools, heavy industries like shipping, automobile and aeronautics and so on. Thus in order to safely predict the structural integrity of components, an accurate understanding of the plastic behaviour of iron is of utmost importance. Thence it has been a popular field of investigation and research for different individuals and scientific teams all over the world. The most common way in which deformation [1-3] takes place is due to the presence and movement of crystal defects called dislocations. Iron has a body centered cubic (bcc) structure and it has been established over the years that the laws governing the plastic

behaviour of bcc metals are quite different compared to the laws applicable for face-centered cubic (fcc) and hexagonal close packed (hcp) materials. A detailed overview of the above mentioned laws and the gradual advances in research pertaining to explaining the structure and deformation behaviour of Fe and other bcc metals is provided in the following section.

## 1.1 Historical background and related terminologies

From around the early part of the 20th century, the first studies [4-6] of single crystals in order to determine their mechanical properties were made for the hexagonal close packed (hcp) and face-centered cubic (fcc) metals. The main outcomes of such studies established an athermal nature of the deformation by crystallographical slip and a governing law for slip known as the Schmid's law [4]. This law predicted that for a certain material, the yield on the slip plane takes place at a constant value of the shear stress acting on the plane known as the critical resolved shear stress (CRSS). The CRSS value is independent of the slip system or the slip sense and it is assumed that the resolved shear stress on the activated slip system in the direction of slip is the only stress component responsible for the plastic deformation. However the research work of G.I. Taylor and his collaborators on  $\alpha$ -iron [7] and  $\beta$ -brass [8] predicted a very different slip behaviour in body-centered cubic (bcc) materials as compared to hcp and fcp structures, thus limiting the universality of Schmid's law.

The most important features of the plastic behaviour of bcc materials relating to properties of screw dislocations are the dependence of the flow stress on temperature and strain-rate i.e. there is quite a brisk increase of the yield and flow stresses with decrease in temperature and increase in the strain rate; and the variation of the CRSS with the sense of shear called the twinning-antitwinning asymmetry of the yield and flow stresses [9-11]. These features have been found in a variety of transition metals [12-20], alkali metals [21-24] and even in the molecular crystal hexamine that crystallizes in the bcc structure [25]. In the year 1960, Basinski and Christian [26] made the extremely precious observation, that the sensitivities of the flow and yield stresses to strain rate and temperature do not vary in an orderly manner with the strain.

This means that the increase in the energy barriers that are being overcome with the help of thermal activation is not monotonic with respect to straining. Whereas on the contrary in fcc metals it increases monotonically with increasing strain [27, 28]. This is one of the prime findings that led to the belief that some other intrinsic factor is the driving force for temperature and strain-rate dependence of the flow stress in bcc metals. This intrinsic factor was later found to be the core of the  $\frac{a_0}{2} \langle 111 \rangle$  screw dislocations that may spread into several planes of the  $\langle 111 \rangle$  region. This was first proposed by Hirsch in 1960 [29] and later affirmed strongly by many experimental and theoretical research performed thereafter. Thence the dislocation core is responsible not only for the high lattice friction stress but also for the rest of the intriguing features of the slip geometry and dependency of the yield stress on orientation [9, 11, 30-32]. This basic characteristic of screw dislocations relates to the crystallography of the bcc lattice and hence is common for all bcc crystals.

### 1.1.1 Dislocation glide mechanism

The thermally activated glide of screw dislocations in body-centered-cubic (bcc) crystals proceeds through the formation and propagation of kink pairs by means of the Peierls' mechanism [9] named after Peierls for his early work on dislocation theory. The motion of screw dislocations occurs in and is controlled by a periodic potential originating from their non-planar core structure which is commonly known as the Peierls' potential [9]. Peierls also proposed the standard Peierls Nabarro mechanism [9] which is accepted as the standard process of dislocation glide. Herein, the dislocation moves in steps from one Peierls' valley [9] to the adjacent and so on, resulting in an overall glide from one part of the crystal to another. Such a step involves first the formation of a pair of kinks on the dislocation by the movement of some of the atoms to the next Peierls valley [9]. This is followed by the propagation of the kinks outwards along the dislocation line, i.e. the atoms move along the direction of the burger's vector parallel to the dislocation line and more atoms start moving in the crystal rows contiguous to the dislocation line. Finally the entire dislocation moves to the next Peierls valley [9] when the kinks have traversed the entire length of the dislocation. For this process, the dislocations need to

overcome an energetic barrier called Peierls' barrier [9]. Both the applied shear stress along the dislocation glide plane and temperature in the crystal play a part in this process by providing the necessary forces and energies to the atoms, first for the formation of kink pairs and then for the propagation of kinks along the dislocation line, which leads to the glide of the entire dislocation in a direction perpendicular to the motion of kinks.

This phenomenon has been schematically represented in Fig. 1.1 for clarity, where we have reduced the extension of a kink to one interatomic distance along the line. In Fig. 1.1 (a), we can see the plan view of a perfect crystal plane where atoms and their positions are represented by small circles. A perfect crystal has no dislocations and there is perfect registry of the atoms along the atomic rows. The next figure, Fig. 1.1 (b), shows the plan view of a crystal with some lattice distortion, enough to create a straight screw dislocation (shown more or less at the center of the crystal). The dislocation is created due to the de-registry between two parts of the crystal resulting from lattice distortion. This de-registry is visible along the atomic rows in the form of slight perpendicular displacement of atoms in one part with respect to the original atomic directions. The next step is shown in Fig. 1.1 (c), where a kink pair is formed at the center of the screw dislocation along the dislocation line. This proceeds by the movement of the central pair (vertically) of atoms of the de-registered part (right part in the figure) at the interface with the perfect part, to new atomic positions. These movements have been shown with arrows and the old positions of the atoms are represented by striped circles and new positions with the usual circles. The new atomic positions are perfect lattice positions of the original perfect crystal and hence this small central portion of the crystal has perfect registry with the left part. As a result, the top portion of the crystal experiences some tension in the surroundings of the atoms moving apart. However in the bottom portion of the crystal, the atoms move closer to each other resulting in a compression of the crystal around these atoms. The next step is shown in Fig. 1.1 (d). It shows the first step of the propagation of the kink pair, which occurs outward along the dislocation line. The pair of atoms just next to the central kink pair on both sides then move to new atomic positions, which again correspond to perfect lattice positions of the original perfect crystal (left part). Thus there is further re-registry of this portion of the crystal with the portion on the left. Thus the kinks continue to propagate further along

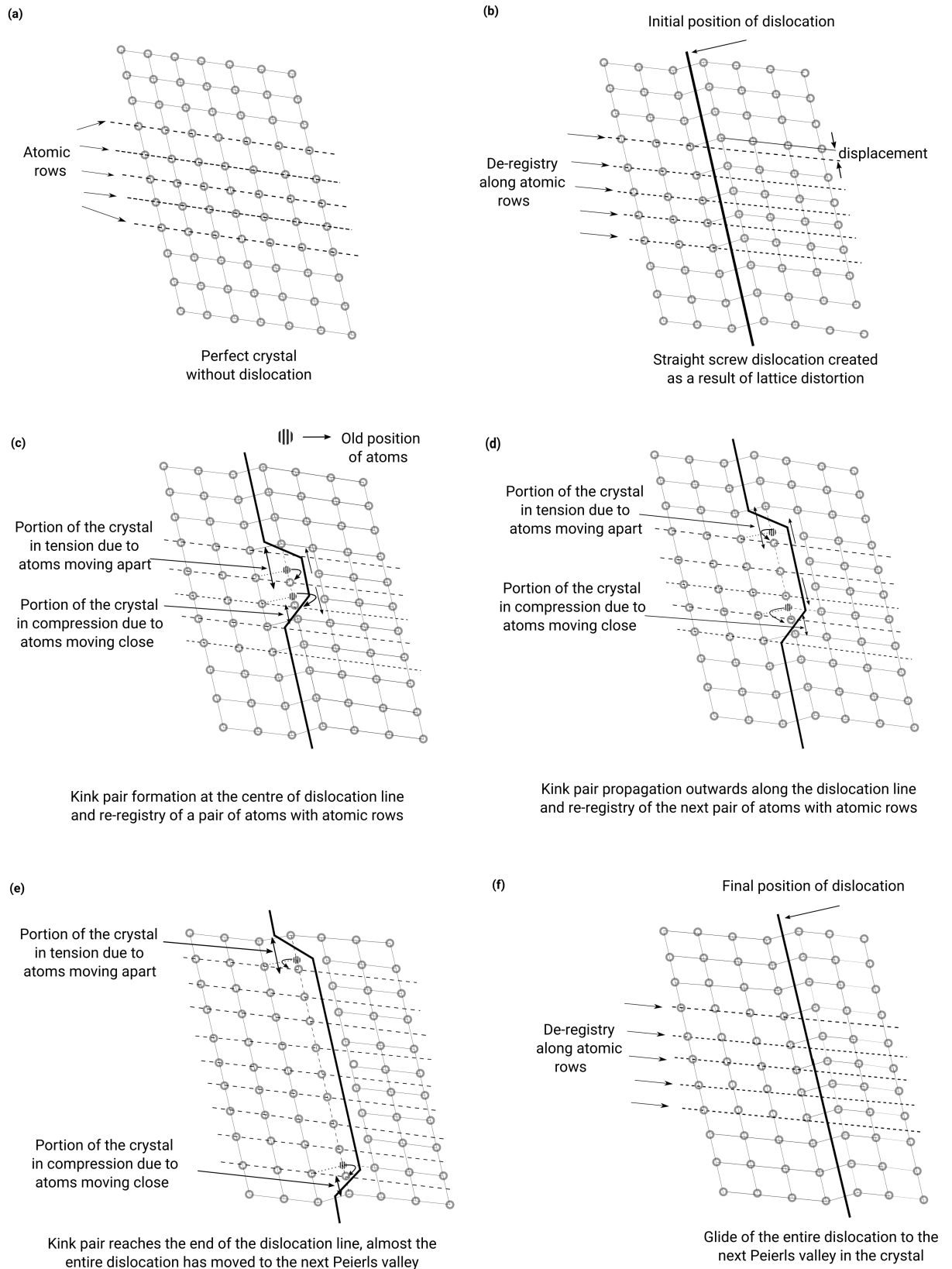


Figure 1.1: Sketch of the plan view of a (1 1 0) crystal plane (glide plane) showing the process of kink pair formation along a screw dislocation and stages of kink propagation along the dislocation line which finally results in the glide of the screw dislocation

the dislocation in this step wise manner till it finally reaches the end of the dislocation line, as shown in Fig. 1.1 (e). At this point, almost the entire dislocation has moved to the next Peierls valley in the crystal. Finally the entire dislocation is in the next Peierls valley and in the form of a straight screw dislocation once again. This step is shown in Fig. 1.1 (f). At this point, the interface of de-registry between the two crystal portions has moved to the right, i.e. a portion of the crystal on the right has now re-registered with perfect lattice positions of the original crystal on the left. The whole process repeats again with the formation of a new kink pair and this is how the dislocation glides along a crystal plane in a step-wise manner.

### 1.1.2 Experimental and Computational observations of the past years

Numerous experimental studies in order to examine the elementary characteristics of slip deformation in iron at low temperatures have been performed over the years [26, 33-43]. However it was only in 1981 that the fundamental aspects of dislocation plasticity, such as the yield stress for slip or the operating slip systems, were examined in the entire range of temperature. Aono and his collaborators [44] carried out a thoroughly planned study of deformation in single crystals of Fe to temperatures as low as 4.2 K. They succeeded in showing that the deformation mode depended on the size of the specimen being tested and were able to plastically deform specimens of relatively small sizes and study the elementary properties of deformation by slip. They also observed the twinning-antitwinning effect during the course of their research.

In the pioneering work of Seeger, the variation of the yield stress as a function of temperature and orientation showed that the deformation behavior of bcc crystals can be divided into three temperature ranges:  $T < 100K$ ,  $100K < T < 250K$ , and  $250K < T < 340 K$  [45-46]. Above 340 K lies the athermal region in which the value of yield stress was around 15 MPa independent of loading orientation. The regime between 250 K and 340 K is assigned to the fully developed kink-pairs governed by the elastic-interaction (EI) approximation [47]. Below 100 K it is governed by the formation of kink-pairs in a manner of bow-out on the primary (110) slip plane according to the line-tension (LT) approximation [48]. In the temperature zone between 100 K and 250 K, there is a discrepancy in the basic slip mechanism. Seeger, from

his dedicated studies came upon the conclusion that the kink-pair formation takes place on the (112) planes [47] whereas Diehl and Brunner [49] were of the opinion that the glide takes place on the (110) planes. The pioneering efforts to establish the basic slip mechanisms of the screw dislocation are however attributed to the research work of Taylor and Elam [7], who proposed something known as the pencil glide mechanism. Herein it was supposed that the slip occurs along the  $\langle 111 \rangle$  direction but the main slip occurred along the plane with the maximum value of resolved shear stress.

Following these first attempts, several contradicting observations have been reported about the orientation and directions of active slip planes in bcc crystals [50]. Gough [51] and Barrett *et al.* [52] stated that the slip takes place on the (110), (112), and (123) families of crystallographic planes. More recent studies suggest that the elementary slip at the microscopic level takes place exclusively on the (110) planes, and the apparent slip on both the (112) and (123) planes is actually composed of multiple elementary slip steps on two non-parallel (110) planes [53]. A systematic observation of the slip planes in single crystal iron was also presented by Aono *et al.* [44]. According to their results, the deformation below 200 K is clearly governed by the screw dislocations whose slip plane is exclusively the (101) plane at liquid He temperature for any loading orientation with straight slip lines parallel to each other. However, as temperature being increased, the macroscopically observed slip plane approaches the maximum shear stress plane. Another interesting feature observed in experiments was the phenomenon of anomalous slip [54,55]. The anomalous slip occurs in bcc crystals at low and moderate plastic strains when the deformation proceeds on a set of (110) planes on which the resolved shear stress is substantially lower than that on the primary, i.e. with the highest Schmid factor, (110) slip plane. All these experimentally observed phenomena can not be fully understood without knowledge of microscopic processes associated with the glide of the screw dislocations. In order to establish a link between the macroscopic mechanical properties and the dislocation core structure, our first task is to determine the elementary slip behavior of the  $\frac{a_0}{2} \langle 111 \rangle$  screw dislocation in iron at the atomic scale. Unfortunately, direct observations of the atomic core structures of the  $\frac{a_0}{2} \langle 111 \rangle$  screw dislocation in bcc metals are difficult and only very few attempts have been made so far [56,57]. This is because the atoms around a screw dislocation are displaced

primarily along the dislocation line direction while their displacements perpendicular to the dislocation line, which can be detected by the modern high-resolution transmission electronic microscopy (HRTEM), are usually very small (their magnitude is given by the elastic anisotropy of the material). Thus, the understanding of the screw dislocation behaviour at the atomic level relies ultimately on the modelling and simulation techniques.

Different atomistic scale studies have been carried out for  $\frac{a_0}{2} \langle 111 \rangle$  screw dislocation in bcc metals. A variety of methods and techniques have been employed over the years like : pair potentials [22, 58, 59-63], many-body central force potentials [30, 32, 64], tight-binding and other approaches that include explicitly the electronic structure [65-70] and most recently by ab-initio density functional theory (DFT)-based methods [71-74]. All these studies revealed non-planar cores and the twinning-antitwinning asymmetry of the critical stress at which the dislocation starts to move. However, two distinct core configurations were found in different studies of nominally the same materials. In both cases the core spreads into three (110) planes of the [111] zone but, in one case, it is unique and invariant with respect to the  $[10\bar{1}]$  diad, a symmetry operation of the bcc lattice and, in the second case, two distinct configurations exist that are related by the diad operation [10,30]. Depending on the details of atomic interactions, either of these two structures can be found. Significant advances have been recently established towards describing the dislocation core structures under stress, by Duesberry and Vitek [30], Domain and Monnet [75], Chaussidon et al. [76], Ventelon and Willaime [77], Groger et al. [78-80], Clouet et al. [81], and Ventelon [82]. Using density functional theory (DFT) based calculations, some important facts that were previously debatable have recently been laid to rest. These include the nondegenerate dislocation core structure [83], the (110) glide plane and the single-hump Peierls barrier [77]. Another significant step in the field of atomistic simulations has been the prediction of the kink-pair formation enthalpy on screw dislocations for  $\alpha$  - iron by Proville *et al.* [84]. They employed a line tension model parametrized by using EAM interatomic potentials and derived the kink-pair formation enthalpies using DFT calculations. However, the entire link to predict accurately the mechanical properties based on the dislocation core structure are yet to be established.

In the following section, we describe in brief the experiments performed by D. Caillard and the

corresponding interesting observations that lay the foundation for this thesis work.

## 1.2 Motivation behind the thesis: experimental observations of D. Caillard

In spite of all the experimental and simulation work carried out over the years, some important questions about the dislocation core structure remained unanswered. D. Caillard identified some very important points [85] that remained unsolved. The first was regarding the exact elementary slip plane of screw dislocations. It was still not established exactly if it was the (110) plane as predicted by recent atomistic calculations yielding non-degenerate compact cores, or (112), in agreement with previous conclusions based on the existence of two types of degenerate cores. It was also still unknown if there is a change of elementary slip plane at 200-250 K as postulated by Brunner and Diehl in Fe [49]. Secondly Dr. Caillard identified the obscurity regarding the origin of the discontinuity observed in the temperature dependence of the activation area of several bcc metals. In Fe, this discontinuity had been observed at 200-250 K by Quenel et al. [86], Kuramoto et al. [87], Aono et al. [44], and Brunner and Diehl [88]. It was still unclear if it was due to a specific shape of the Peierls potential profile, as suggested by Takeuchi [89], Aono et al. [44], and Koizumi et al. [90]; or due to a change of kink nucleation plane as proposed by Brunner and Diehl [49]; or due to another change of dislocation mechanism [91]. The third basic mystery was regarding the explanation that could be proposed for the large difference between the Peierls stress deduced from atomistic calculations, and the flow stress extrapolated to 0 K. It could probably be due to pile-up effects, as suggested recently by Gröger and Vitek [92], or some other unexpected softening mechanism at low temperature. Fourthly there was a need to find some simple explanations for the various effects of interstitial and substitutional alloying elements. For instance, the origin of the complex effect of carbon atoms in iron, i.e. hardening below 150 K, and softening between 150 K and 250 K [87]. Answers to these questions require a good knowledge of the dynamic properties of dislocations, which can be deduced from in situ observations. Several in situ experiments were carried out in the 1970s, in Fe and Fe alloys,

by Furubayashi [93], Kubin and Louchet [94], and in Nb by Ikeno and Furubayashi [95] and Louchet *et al.* [96]. However, the resolution of the high-voltage electron microscopes used at that time was too poor to reveal all the details of the dislocation glide mechanism.

Hence Dr. Caillard planned a series of experiments with the aim to re-investigate the dynamic properties of dislocations in Fe and Fe alloys, at various temperatures, and as a function of stress. He performed two sets of experiments wherein in the first part, the properties of dislocations in pure Fe were investigated at room temperature, and described in terms of the kink-pair mechanism. In the second part their evolution upon decreasing the temperature to 100 K were studied and the results, thoroughly analysed. Using the obtained results, explanations were given to answer the four problems identified above. For carrying out the experiments, Dr. Caillard obtained a large-grain polycrystal of pure iron from J. Le Coze, Ecole des Mines of St. Etienne, France. This sample was of very high purity with the amount of residual C, N, O and Si atoms between 2.5-4 ppm-wt respectively and 15 ppm-wt when accounted as a whole. Other elements combined were less than 2 ppm-wt. The initial dislocation density was quite low:  $\rho_d = 10^7 \text{ cm}^{-2}$ . A number of rectangles of size 3 mm by 1 mm and thickness 50  $\mu\text{m}$  were cut by spark erosion to be used as specimens. Then they were polished mechanically followed by a process wherein they were electrochemically polished to perforation at their centre. A GATAN room temperature straining holder was employed for the specimens to be glued on, and a JEOL 2010 HC transmission electron microscope was utilised to observe them. A Megaview III video camera that operated at 25 images per second was employed to record the sequence of unfolding events during the experimentation. The deformation of the microsamples were carried out in the microscope by a series of deformations and relaxations carried out at constant strain-rates. The average strain rate was around,  $\dot{\epsilon} = 10^{-6} - 10^{-5} \text{ s}^{-1}$ . The plane normals for the grain was  $[\bar{1} 2 3]$ , and the direction of straining was along  $[1 \bar{4} 3]$ . The diffraction vector for all the images taken was  $[220]$  and the angle of tilt was set to  $-8$  deg. Next, in order to analyze the motion of dislocations, the intensities of two superimposed images were subtracted because of which there is disappearance of the background and the immobile dislocations. The moving dislocations appeared in positive (previous position) and negative (latest position) contrasts and the dislocations moving very swiftly demonstrated fuzzy images. The widths of these

images were equal to the displacement undergone during the time of exposure. With these conditions, a fuzzy contrast with homogeneity signified a constant velocity, whereas a contrast with inhomogeneity implied a varying instantaneous velocity [97].

From the first set of experiments conducted at room temperature, Dr. Caillard was able to draw a number of conclusions [85] from the analysis of the results. With regards to the screw dislocations, it was observed that the velocities of screw dislocations are proportional to their lengths. Dr. Caillard was able to infer the elemental slip planes to be (110). He also measured a microscopic activation area of  $23b^2$  on a single dislocation, a value slightly lower than the macroscopic value. More importantly, all the results were consistent with a kink-pair mechanism wherein the critical separation of kinks was too short to be described by a Coulombic elastic interaction as proposed in theory.

The second set of experiments were carried out at low temperatures in between 100 K and 300 K in order to investigate the mechanism change observed at around 250 K. By plotting the temperature variation of the yield stress  $\tau$  for pure Fe single crystal (measured by Kuramoto *et al.* [87] and Brunner and Diehl [49]), the discontinuity in temperature variation of yield stress and a huge difference between the theoretical Peierls stress and the yield stress extrapolated to 0 K can be noticed as seen in Fig. 1.2 [85]. The yield stress increases from very low values at 330 K (athermal regime) to about 370 MPa at 0 K, whereas the theoretical Peierls stress deduced from atomistic calculations available in literature at that point of time were much higher : 1200-1800 MPa [76] and 1300-1900 MPa [82]. However, different works independent of Dr. Caillards observations but published at a later time have deduced much lower Peierls stresses : 400 MPa [98] , 800 MPa [99] and 300-500 MPa [101]). Still, all these values are much higher compared to experimental values. A change of slope is observed in the plot at a stress  $\tau_{yz} = 50$  MPa and temperature  $T = 250$  K. This corresponds to a local minima in the stress dependence of the respective activation areas represented by A. Such discontinuity basically indicates a possible change in the dislocation mechanism that needed to be explained. The only difference in the set-up of the second set of experiments in comparison with the first was the use of a low-temperature straining holder. This device was also constructed by GATAN, and was borrowed from the Paul Sherrer Institute of Willigen in Switzerland. Using this device, one

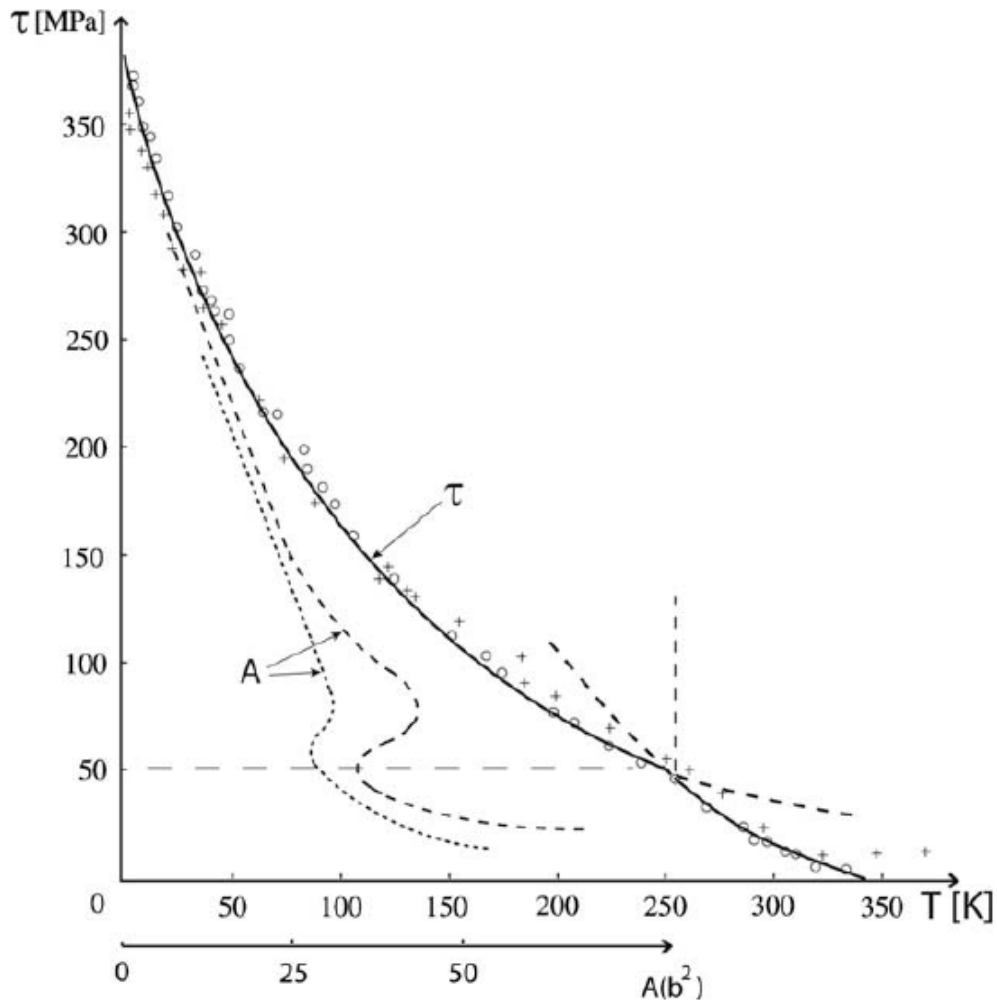


Figure 1.2: Temperature dependence of the yield stress  $\tau$  (projected on the most stressed (110) plane) of pure Fe. Tensile tests by Kuramoto et al. [86] (crosses) and Brunner and Diehl [49, 88] (circles), straining axis close to  $\langle 148 \rangle$ . The corresponding activation areas,  $A$ , are shown in large dashed lines [87] and dotted lines [88].

could strain microsamples from 100 K to 300 K. Most results were obtained in three samples, each strained at various temperatures. The Schmid law was approximately verified in the microsamples, i.e. all mobile dislocations had high Schmid factors, when the local stress axis was considered to be parallel to the applied one. As in the first set of experiments, difference-images were largely employed to improve the resolution of the measurements. It was observed that in the lower temperature range, straight screw segments have a jerky type of motion in (110) planes, quite different from the classical Peierls mechanism seen at room temperatures. The jerky motion refers to an observed phenomenon during experiments wherein the dislocation instead of gliding gradually from one Peierls valley to the adjacent, makes a long jump of several Peierls valleys. Each jump is followed by a waiting time during which the dislocation is pinned more or less to the same position, followed by another long jump and so on. The distributions of waiting times in locked positions, jump distances, the temperature variation of the average jump distance, and the stress/temperature variation of the macroscopic activation areas were inconsistent with the kink-pair mechanism observed above 250 K. Dr. Caillard explains this phenomenon in terms of a locking-unlocking mechanism, that has previously been proposed for hexagonal closed packed (hcp) metals. This change of mechanism is able to account for the extremely low flow stress when extrapolated to 0 K. The jerky motion can be understood well from Fig. 1.2 which has reproduced from Dr. Caillard's work [100].

Fig. 1.3 (a) shows various stages of the jerky motion of a dislocation at 110 K. In between the first two and the last two frames reproduced from the video recording, we can observe some instantaneous jumps equivalent to the distance between several Peierls valleys, whereas we observe no motion whatsoever during the 21 intermediate frames as visible from the corresponding difference-images in Fig. 1.3 (a). The average values of jump lengths were found to be  $k = 0.85$  nm (almost 4 Peierls valleys) at 110 K, and  $k = 0.45$  nm (almost 2 Peierls valleys) at 160 K (another sample). In addition, a sharp contrast is observed between the initial and final positions of a jump (which has been enlarged and reproduced in Fig. 1.3). This conveys that the dislocation remains immobile for the majority of the time separating the two images. A comparison is drawn with the images of a steady motion at room temperature, shown in Fig. 1.3 (b). Here it can be seen that the image of the dislocation is blurred giving us an

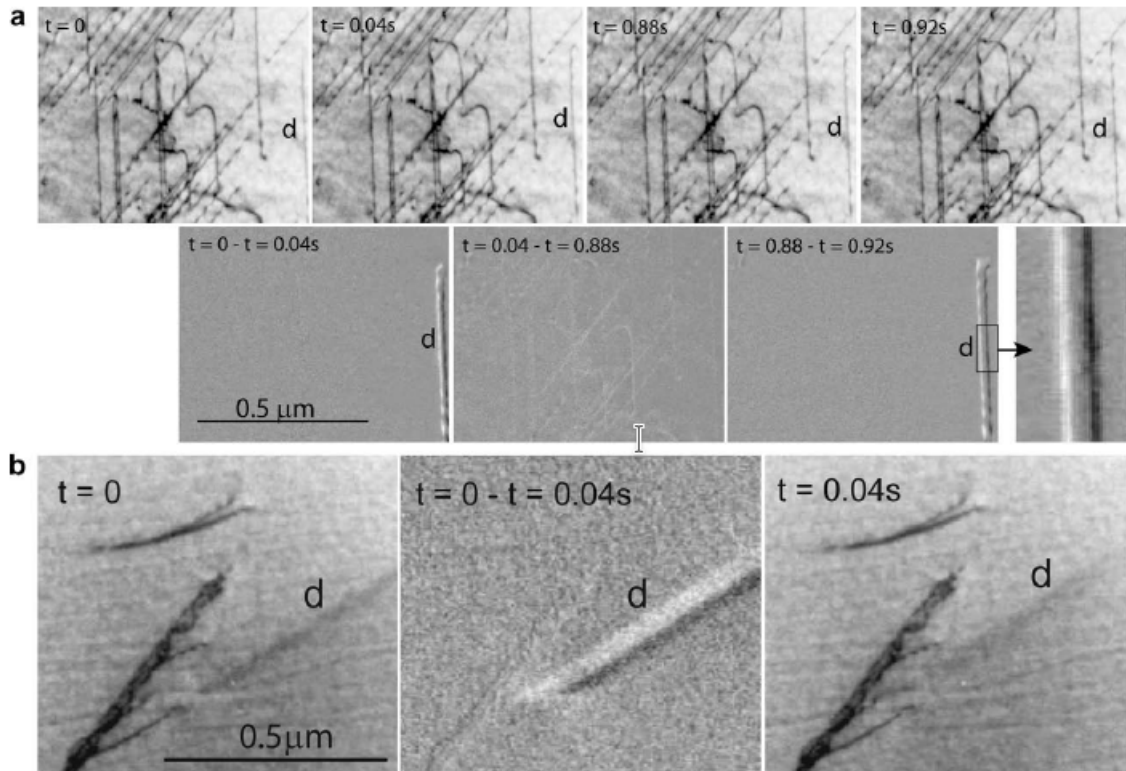


Figure 1.3: Comparison of dislocation kinetics at 110 K and 300 K. (a) At 110 K, dislocation  $d$  jumps between  $t = 0$  and  $t = 0.04$  s, and between  $t = 0.88$  s and  $t = 0.92$  s, whereas no motion occurs between  $t = 0.04$  s and  $t = 0.88$  s (seen in difference-images). The inset shows that the black/white contrasts of the difference-image are sharp and widely separated, in agreement with a jerky motion with no acceleration/deceleration phases. (b) At 300 K, the moving dislocation has a fuzzy contrast and the black/white contrasts of the difference-image are adjacent, in agreement with a steady motion.

idea about its motion during the time of exposure. It can also be observed that the difference between two successive frames shows a pair of adjacent black and white fuzzy contrasts. It was established in previous works [97] that the images like in Fig. 1.3 (a) convey that there is a variation in the instantaneous velocity by a factor of around 40,000. This implies that even by considering quite large variations in the local stress, the phenomenon can't be explained by a kink-pair mechanism. After detailed analysis of the experimental results, Dr. Caillard arrived at a number of conclusions. It was found that the motion of screw dislocations become jerkier and jerkier as the temperature decreases. An extensive amount of cross-slip was observed, but single jumps were found to pertain exactly to the (110) planes (at least the longest jumps). Hence as also observed in the first set of experiments, the elementary glide planes are of the (110) type in the entire range of temperature considered. Dr. Caillard also found that the waiting times in the locked positions are in accordance with an exponential distribution which agrees with a constant probability of unlocking per unit time. The transition between the jerky motion and the classical kink-pair mechanism was found to occur around 250 K as previously found by others and reported in Fig. 1.2. Dr. Caillard explained the screw motion as a series of locking and unlocking thermally activated events. Thus it can be inferred that there exists a metastable-glissile configuration responsible for such phenomena. The configuration that control the motion of screws above 250 K is thus a kink-pair and below 250 K it follows the bulge mechanism. Dr. Caillard reproduced correctly the peak of the activation area at 75 MPa and 250 K with only one adjustable parameter; the increase of core energy  $\Delta E$ , between sessile screws and mobile near screw dislocations. The values were found to be in the range of 26-37 meV per b above 250 K, and 11 meV per b below that. The first values are consistent with DFT calculations and the second one is considered to be the difference between the core energy of sessile screws, and the core energy of the hypothetical metastable-glissile configuration. Under such conditions, Dr. Caillard infers that the smaller than expected yield stress extrapolated to 0 K is the result of an energy barrier smaller than the depth of Peierls valleys.

This highly interesting and new phenomenon of the occurrence of jerky motion of screw dislocations at low temperatures inspired us to investigate the same at the atomistic scale. As the classical theory fails to explain or predict this phenomena, we have dedicated our energies

during the course of the thesis, in the direction of predicting a new generalized theory that can predict the behaviour of screw dislocations with acceptable accuracy over the entire range of temperatures. We have paid close attention to the finding of Dr. Caillard and tried to implement them wherever possible, in our codes during the course of all our simulations. In the following chapters we have explained in a systematic way the tools and techniques we have employed, mixed with our scientific intuition and also the results and findings of our work.

# Chapter 2

## Description of Computations

### 2.1 Description of the model for interaction between atoms

In order to analyze the mobility of dislocations, it is important to study the relative motion of atoms that constitute the dislocation core. This can be done with the help of atomistic scale simulations where the motion of atoms is integrated numerically. There are numerous models and methods that are employed to calculate the interaction between atoms.

Density Functional Theory (DFT) [102, 103] based ab-initio calculations are known to be the most accurate for calculating the time evolving atomic positions and energies because they take into account the electronic structures of the atoms in many body systems. This theory uses functionals, i.e. functions of another function to calculate the forces between atoms. For our case the function is the electron density that depends on spatial positions of atoms. DFT calculations have helped to confirm some important features of dislocation studies like the non-degenerate dislocation core structure [104] the 110 glide plane and the single-hump nature [77] of Peierls barrier for BCC crystals. But the major drawback of DFT based methods when applied to extended defects like dislocations is the extremely limited number of atoms that can be considered in the simulation cell which is of the order of a few hundreds only.

The reason being that ab-initio calculations are computationally very demanding as a large number of Schrodinger's equations need to be solved for the electrons corresponding to the atoms considered. However it proves enough to study straight dislocations which don't have any translational variance along the dislocation line thus allowing us to limit the length in this direction to that of the Burgers vector i.e.  $|b| = a_0\sqrt{3}/2$  and apply periodic boundary conditions in the direction. However at low temperatures, the motion of screw dislocations proceeds through the formation of kink pairs which breaks the translational invariance along this direction. Thus we have to consider a long 3D dislocation to simulate this process at the atomic scale which is beyond DFT capabilities for the present time [105].

Another possibility is the use of inter-atomic potentials wherein the potential energy of each atom and the forces between them are computed. For the case of metals, pair-potentials [106] were traditionally used to determine the total energy but later on they were found to give erroneous results as they ignored the coordination dependent many body interactions. This led to the development of the Embedded Atom Method (EAM) [98, 99, 107] interatomic potentials which offer a simple and dependable tool to describe bonding in metallic systems based on local density, the spatial co-ordinates of which are known. It incorporated an approximation of the many-atom interactions which is neglected by the traditional pair-potential scheme. The potential energy of individual atoms are obtained by embedding an atom into the local electron density collectively provided by the other atoms of the system. Using them, the dependence of the strength of individual bonds on the local environment can be accounted for. EAM potentials can be applied to systems involving a large number of atoms. EAM potentials are less accurate than DFT calculations but they can be applied to systems involving a large number of atoms. In order to better simulate the glide of screw dislocations, it is imperative to consider dislocations whose sizes are comparable to those observed in experiments i.e. consisting of a large number of atoms. Thus we have chosen to perform Molecular Dynamics (MD) simulations where the atomic motions are integrated classically according to Newton's laws as they are able to handle very large number of atoms, and coupled them with EAM potentials in order to calculate the atomic energies. We have chosen to work with three different EAM potentials [98, 99, 107] in order to determine the common trends observed with them and thereby reduce tentatively the

uncertainty of our analysis.

LAMMPS [108] is another very common tool employed to calculate interatomic forces. It is a classical molecular dynamics (MD) code. Molecular dynamics (MD) is a computer simulation method for studying the physical movements of atoms and molecules. LAMMPS codes can be employed to study the interactions and evolution of a variety of entities like atoms, granular materials, organic molecules, proteins, DNA, metals, point dipole particles and also a hybrid combinations of these. It can be employed to compute a wide variety of force fields like pairwise potentials, coulombic and long-range interactions between charged entities, polarization models, charge equilibration, coarse-grained potentials, electron force fields and so on. In order to calculate the forces between atoms it employs a large number of EAMs and MEAMs (Modified Embedded Atom Method) [109] interatomic potentials. MEAM is an extension to the original EAM potentials with the addition of a term to calculate the angular forces. Hence it is suitable for modeling metals and alloys with fcc, bcc, hcp and diamond cubic structures, as well as covalently bonded materials like silicon and carbon. MEAM interatomic potentials consider the scalar product of simultaneous interactions of two pairs of atoms centred on one common atom and the spatial angle between the three atoms at each step. As a result, they are much more complex and difficult to handle.

Considering all the above facts, figures and limitations in mind, we chose to work with EAM potentials to predict and model the crystal energies via atomistic scale simulations. EAM potentials allow us to work with a large number of atoms and also allow for a direct calculation of the kink pair formation enthalpy of 3D screw dislocations. As it is difficult to modify the LAMMPS code, we have chosen to work with our own code integrated with the ability to employ the EAM potentials. In the following section, we describe in details how the EAM potentials work.

### 2.1.1 EAM : Embedded Atom Method interatomic potentials

Daw and Baskes [110] were among the pioneers who proposed the embedded-atom method. They viewed the energy of the metal as the energy obtained by embedding an atom into the

local electron density collectively provided by the other atoms of the system. In addition to it, there is also an electrostatic interaction. They derived the following equation for the cohesive energy.

$$E_{coh} = G\left(\sum_{j \neq i} \rho_j(r_{ij})\right) + \frac{1}{2} \sum_{i,j(j \neq i)} \phi(r_{ij}) \quad (2.1)$$

where  $G$  is the embedding energy which is a function of the atomic electron density  $\rho$ ,  $\phi$  is the electrostatic pair potential interaction between any two atoms. The multi-body nature of the EAM potential is a result of the embedding energy term. Both summations in the formula are over all neighbors  $j$  of atoms  $i$  within the cutoff distance.

The embedding energy is basically the interaction between the atom and the background electron gas. The background density for the individual atoms in the above equation is predicted by analyzing the superposition of atomic-density tails from all the other atoms at the nucleus. EAM potentials provide a kind of physical picture of metallic bondings wherein every atom is embedded in a gas of electrons generated by the neighboring atoms. The embedding function incorporates important many-atom interactions in the equation, making it much more accurate than traditional pair potentials. The EAM is presently the most preferred method for performing semi-empirical calculations in close-packed metals as it provides the combination of the simplicity of computations required for large systems while providing a physical picture that accounts for many atom effects.

EAM potentials are constructed by fitting a lot of parameters in analytical expressions to best suit the materials for which they are meant. However, in order to obtain an accurate and realistic potential, elaborate analytic expressions involving a lot of terms like density-dependent terms, angular forces, moment expansions etc. are necessary for most materials under different conditions (geometries, structures, phases). Hence these potentials constitute complex combination of a number of functions nested into one another. This makes fitting of a potential to a certain material a daunting task. A set of experimental quantities that occur in an analytical expression can be fitted in numerous different ways and usually very arbitrary

assumptions have to be made to reduce the number of parameters to a manageable level. This is the main reason why potentials that work well at  $T = 0$  K may fail at finite temperature, or for geometries or local conditions not considered when the fit was made e.g. failing at surfaces, defects. The reason being that atoms near surfaces and other defects are embedded into an electron gas of density profile quite different from that of atoms in the bulk.

In this regard, significant progresses have been made in the accuracy of EAMs. This can be attributed to its adjustment with a data basis built from ab initio calculations, involving dislocation configurations. In order to overcome the problem of transferability, F. Ercolessi and J.B. Adams [111] devised a new method wherein they processed a large amount of output of first-principles calculations for positions and forces and combined this information with traditional fitting on experimental quantities, thereby obtaining a potential by a numerical optimization procedure. They named this technique 'the force matching method'. In this framework, the entire set of parameters used to characterize the functions are identified. After that efforts are made to match the forces supplied by first-principles calculations for a large set of different configurations with those predicted by the classical potential, by minimizing the objective function. The various configurations do not need to be related to each other and on the contrary it is desirable to include data relative to different geometries and physical situations in order to achieve a good transferability for the potential. It is useful to use samples from high temperature ab initio MD trajectories in order to obtain a good representation of the regions of configuration space that is explored at finite temperature. In order to check the utility and realism of the potential, preliminary tests using MD trajectories generated by classical potentials are made. If the potential is able to reconstruct exactly the original potentials without any further assumption beyond the analytic form, within acceptable precision and within the range of the function arguments sampled by the input data we can conclude that the EAM potential is accurate and transferable. Thus one can perform calculations of complex metallic structures within the approximate embedding-energy structure. The EAMs based on Force-Matching Method are thus a significant improvement in simplified total-energy calculations for metallic systems and can be extensively and accurately used.

We have carried out our simulations using three different EAMs. EAM1 is developed by

Chamati *et al.* [107], EAM2 by Gordon *et al.* [99] and EAM3 by Marinica *et al.* [98]. The values of the lattice parameter,  $a_0$  and the cohesive forces between the atoms,  $E_{coh}$  for all three EAMs are listed in the table below along with the experimental values.

|                     | EAM1   | EAM2   | EAM3       | Exp.   |
|---------------------|--------|--------|------------|--------|
| $a_0$ (Å)           | 2.8665 | 2.8552 | 2.814781   | 2.8665 |
| $E_{coh}$ (eV/atom) | -4.28  | -4.21  | -4.1224897 | -4.28  |

Table 2.1: Values of the lattice parameter,  $a_0$  and the cohesive forces between the atoms,  $E_{coh}$  for different EAMs and as obtained in experiments

## 2.2 Construction of Simulation Cells

The unit simulation cells used for the study of dislocations consist of atoms placed in symmetric configurations of the perfect crystal that is being modeled. Different methods have been developed over the years to model dislocations. The difference is usually in the boundary conditions that are applied to the simulation cell. Here, we describe some of the methods that have been commonly used over the years to study dislocation motion.

The first method that we are going to describe is the cluster approach where we use a cylinder that has an axis parallel to the dislocation line along which we enforce periodicity. In order to create the dislocation, we displace all the atoms according to the Volterra solution of anisotropic elasticity [112-114]. The atoms on the surface of the cylinder are kept fixed at the respective initial positions whereas the atoms inside the cylinder are relaxed. However, with this process if the cylinder radius is small, the calculation of the Peierls stress needs to be corrected because when the dislocation moves, the boundary conditions are not compatible with the dislocation position anymore. The back stress that results can be computed and corrected from the Peierls stress calculation [115, 116] but it adds to the computational cost. Also the presence of vacuum results in discontinuity in the electronic density which induces oscillations in metals effecting the core properties [117]. This problem vanishes with a large enough radius of the cylinder but then the calculations are no more feasible with ab initio method. In such case EAM potentials could be employed instead.

The second approach that we are going to describe comprises the use of flexible boundary conditions, which in some ways is an improvement of the rigid boundary conditions in the cluster approach. They can be based either on a lattice Green's function [118] or they can be coupled with an empirical potential [119, 120]. Here the atoms inside the cylinder are first relaxed keeping the atoms on the cylinder surface, as well as those in the region outside the cylinder fixed. The resulting atomic forces on the surface are then relaxed using the lattice Green's function such that atoms in all the three zones are displaced. This process is repeated until all forces inside and on the surface of the cylinder converge below a predetermined threshold. The atoms in the outer zone can be regarded as a buffer that prevents forces on the atoms on the cylindrical surface to be influenced by the external boundary. The outer zone can be cylindrical with fixed boundaries or it could be surrounded by periodic boundaries [117]. However in order to ensure the minimize perturbations in the inner regions [121] in metallic crystals, the outer zone needs to be quite large. The lattice Green's function is not that straightforward to implement but it adapts well under applied deformation which allows to determine the core configuration under finite stresses and to compute the Peierls stress [72]. The primary disadvantage of flexible boundary conditions is the difficulty in partitioning the excess energy between the dislocation and the external boundary. For example, it is possible to predict the Peierls stress, but not the Peierls energy when we employ this method to study dislocation glide.

The third approach that we have studied comprises the introduction of a single dislocation in a unit cell with periodic boundary conditions along the dislocation line and surfaces in the remaining directions. The surface atoms are displaced according to the long range elastic field i.e. the Volterra elastic field [113] of the dislocation and may be kept fixed or relaxed according to lattice Green functions [118]. The main disadvantage of this approach as in the case of the previous approach, is that it is not possible to separate the energy contribution of the dislocation from that of the surface.

The fourth approach that was considered involves the use of periodic boundaries in all three spatial directions [74, 112, 122, 123-125] to simulate the dislocation glide. However this is possible only when the total Burgers vector in the unit cell is zero. Thus a dipole of dislocations

having opposite Burgers vectors are introduced in order to produce a zero global Burgers vector. Using elasticity theory, it is possible to calculate the interaction between the two dislocations of the dipole as well as with their periodic images [125] allowing us to isolate the intrinsic properties of the dislocation. However under the action of an applied stress, the two dislocations of the dipole glide in opposite directions. The relative distance and the mutual interactions thus vary with time resulting in periodically oscillating dislocation velocities as they cross the simulation cell.

The fifth approach involves the use of a slab geometry [101] with a single dislocation in the simulation cell. To start with, a perfect crystal geometry is considered and a screw dislocation is introduced by displacing all the atoms as per the isotropic elastic solution [113]. In order to replicate an infinite glide plane, periodic boundary condition (PBC) is used along the directions constituting the glide plane. An additional shift of  $b/2$  is introduced along the direction corresponding to the line of the dislocation in order to account for the plastic strain associated with the screw dislocation and also to reconnect the left and right surfaces perpendicular to the dislocation line. This ensures the existence of the screw dislocation at all times during the computation process. The presence of the non-zero Burgers vector doesn't allow periodic boundary conditions in the remaining direction and hence two free or fixed surfaces are created instead to form a slab [101].

Thus we have described the methods that have been popularly used over the recent years. While weighting all the options, the fifth type of simulation cell proved to best suit our requirements. It provides the flexibility to account for the plastic strain introduced by the screw location as described earlier. Moreover, the problem of periodically oscillating dislocation velocities as seen with periodic boundary conditions doesn't arise in this case. The slab boundary also helps to avoid misleading interaction with periodic images by choosing dimensions that are large enough along the direction perpendicular to the dislocation line. However the most important feature of this approach is that it allows to treat a much larger number of atoms per dislocation. This corresponds to the smallest density of dislocations that can be attained with atomistic scale simulations which is usually very high compared to experimental samples. The spatial details and orientation of the simulation cell used for our computations have been described

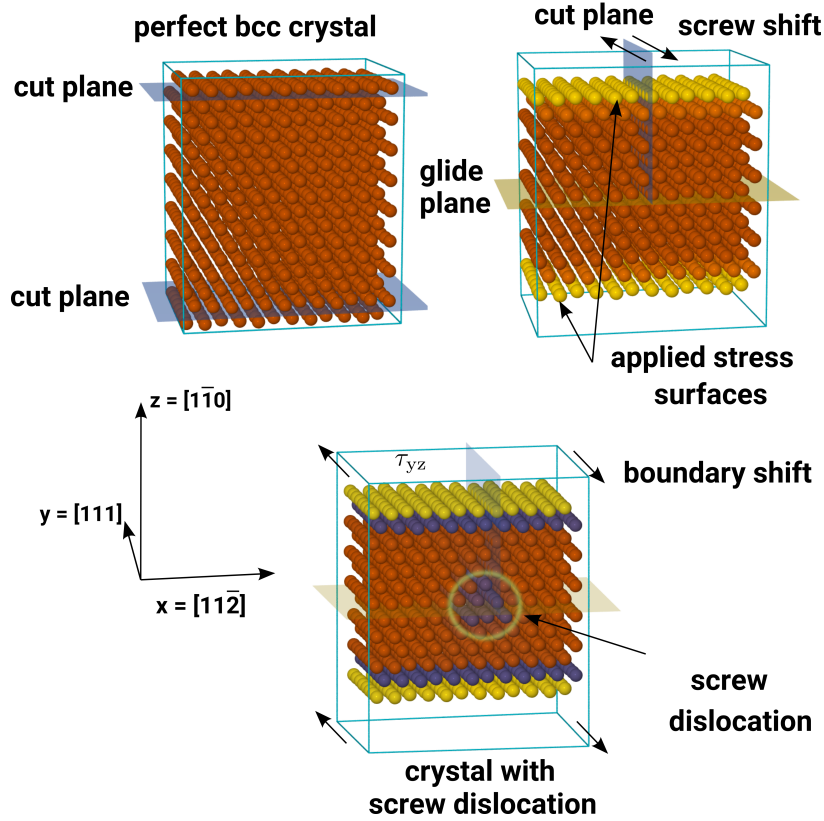


Figure 2.1: Snapshots of all the essential elements of the simulation cell we used for simulating a  $a_0/2[111](\bar{1}\bar{1}0)$  screw dislocation in BCC Fe as considered in [126]

in an easy and step wise manner using Fig. 1.1 [10]. It consists of atoms placed in symmetric Body Centred Cubic (BCC) configuration of a perfect crystal. The simulation cell is oriented in a way that the glide plane corresponds to the horizontal plane of the cell. The XY plane is chosen as the glide plane and hence there is Periodic Boundary Condition (PBC) along X and Y directions. The assigned cell directions are  $X = [\bar{1}\bar{1}\bar{2}]$ ,  $Y = [111]$  and  $Z = [\bar{1}\bar{1}0]$  respectively. The lattice parameter of perfect crystal is represented by  $a_0$  and the Burgers vector  $b = a_0/2[111]$  corresponds to the line direction (Y) of the screw dislocation. The direction Z is perpendicular to the glide plane and refers to the direction along which the simulation cell ends with free surfaces. We took proper care to choose these surface sufficiently far away to avoid interactions of the atoms in the dislocation core with the surface atoms. The simulation cell dimensions have been fixed as  $x = 14 b$ ,  $y = 160 b$  and  $z = 20 b$  respectively ( $b = 2.48 \text{ \AA}$  for  $\alpha$ -Fe). We have ensured that the dimensions along the glide directions are large enough to avoid misleading interactions with the periodic images. A screw dislocation is introduced by displacing all the

atoms as per the isotropic elastic solution [113]. Such simulation cells have been described in earlier works [127-130] too. An additional shift of  $b/2$  is introduced along the Y direction in the computation of the distance between two atoms forming a bond. The boundary conditions are thus no longer periodic, but this trick stabilizes the simulation cell with a single screw dislocation [131]. It accounts for the plastic strain associated with the screw dislocation and ensures the existence of the screw dislocation at all stages of our computations by reconnecting the left and right surfaces perpendicular to the dislocation line. A shear stress  $\tau_{yz}$  is applied to the 110[111] slip system by adding external forces to the atoms in the top and bottom z surfaces. The magnitude of the external force is  $S\tau_{yz}/N_{\text{surf}}$  where  $N_{\text{surf}}$  is the number of atoms in the surface of area S. The atomic forces on the top surface are equal in magnitude but opposite in direction to those on the bottom surface. We relax the atomic positions by a fast quench method or by adding a simple Langevin damping into the dynamical equation of motion integrated with a standard velocity Verlet algorithm [132]. Finally, when we have a maximum atomic force of  $10^{-5}$  eV/Å we consider that the simulation cell has reached an equilibrium. In Fig. 1.1, the atoms are colored as per the deviation of the perfect crystal (in the absence of dislocations) cohesive energy per atom. For the atom  $i$ , the reference energy is denoted by  $E_i^0$ , which can be computed easily before introducing the dislocation in the simulation cell. Denoting the potential energy of atom  $i$  by  $E_i$ , the potential energy deviation is given by  $\Delta_i = E_i - E_i^0$ . The atomic energies are computed by models for interaction between atoms as described in the following section.

## 2.3 Algorithms used for our computations

### Introduction

In the field of condensed matter physics, some methods have been developed over the years in order to calculate the rate of reaction or transition from one system configuration to another. The general logic involves searching for an optimum transition state [133, 134] through which the system will pass between the initial and final states. This transition state is a saddle point

at the edge of the potential energy basin corresponding to the starting state. By following the gradient of energy in both directions from a saddle point, the minimum energy path (MEP) [133, 134] can be traced. In our case, we are interested in studying the process of glide of a screw dislocation in a BCC Fe crystal. With this purpose in mind we first perform a quenching of our simulation cell loaded with an applied shear stress for an initial and final position of a straight dislocation along the glide plane. Quenching relaxes the atomic forces till the simulation cell reaches a mechanical equilibrium. Using these initial and final relaxed positions of the screw dislocation, the Nudged ELastic Band (NEB) [133, 134] computations are then performed to compute the minimum energy path (MEP) for the screw dislocation as it glides from the initial to the final position. After that we use a saddle state of the dislocation derived from the profiles of the NEB simulations to construct a long dislocation in an extended simulation cell and perform the Molecular Dynamics (MD) simulations to study the evolution of the kink pairs as they propagate along the dislocation line and the overall atomic interactions with the hope that they provide some answers towards a proper explanation for the occurrence of 'jerky motions' of dislocations as observed experimentally by D. Caillard [9]

### 2.3.1 Quenching - Relaxation of the simulation cell

Quenching is a process of relaxation of the simulation cell which provides us the most stable atomic configurations. For our case we start with a straight dislocation in our simulation cell, the initial position of which has been defined by its x,y and z co-ordinates. The simulation cell is loaded with an applied shear stress on the yz-surfaces above and below the cell. The resulting force initiates movement of the dislocation which is restricted by coupling the Newton's equation of motion for the individual atoms with a simple Langevin damping. We consider that the cell has reached equilibrium when the atomic forces have diminished to around  $10^{-5}$  eV/Å . This results in a lowest energy static equilibrium starting dislocation configuration. Similarly we can obtain the lowest energy final configuration of the dislocation under the applied shear stress by defining the final position (by changing the x co-ordinate i.e. the direction along which glide occurs) and repeating the quenching process. The distance between the initial and final

positions is equal to  $a_0\sqrt{2/3}$  i.e. the distance between two Peierls valleys which corresponds to the distance between two nearest atomic rows. Here the atomic rows are considered along the dislocation line i.e.  $Y \langle 1 1 1 \rangle$  direction and the distance between them is along the perpendicular  $Z \langle 1 1 2 \rangle$  direction.

### 2.3.2 Molecular Dynamics - Verlet and Velocity Verlet algorithm

Molecular dynamics (MD) simulations are performed to predict as accurately as possible what atoms do in real life i.e. how they interact with other atoms, how their parameters of motion change as a result of these interactions and how a system evolves with time consequently. By knowing a starting configuration of all the atoms in the system we are able to predict simultaneously the new positions and velocities at every time step by providing an algorithm for change and integrating with Newton's laws of motion. It is possible to perform MD simulations up to time scales of the order of nano seconds  $10^{-9}s$  with time steps of the order of femto-seconds  $10^{-15}s$ .

#### Verlet algorithm

For our simulations we use the EAM inter-atomic potentials that provide the force field for the inter-atomic interactions. The same relaxed starting configuration from the quenching process is used to initiate the simulations. The verlet algorithm is employed for estimating the new position and velocity of atoms at every time increment of the MD simulation. The force is the sum of the forces due to the EAM field and the applied external stress.  $F = F_{EAM} + F_{\tau}$ . Newton's equation of motion gives:  $F = ma = F_{EAM} + F_{\tau} = -\frac{\delta U}{\delta r} + F_{\tau}$  (where 'r' is the position at time 't' and 'm' is the atomic mass). The force due to the external stress  $F_{\tau}$  acts only at the surfaces of the simulation cell i.e. only on the surface atoms.

By employing the Taylor series expansion, the position at  $t+\Delta t$  is given by the equation.

$$r(t + \Delta t) = r(t) + v(t)\Delta t + \frac{1}{2!}a(t)\Delta t^2 + \frac{1}{3!}b(t)\Delta t^3 + O\Delta t^4 \quad (2.2)$$

Similarly, the position at  $t - \Delta t$  is given by the equation.

$$r(t - \Delta t) = r(t) - v(t)\Delta t + \frac{1}{2!}a(t)\Delta t^2 - \frac{1}{3!}b(t)\Delta t^3 + O\Delta t^4 \quad (2.3)$$

By adding the two equations we get :

$$r(t + \Delta t) = 2r(t) - r(t - \Delta t) + a(t)\Delta t^2 + O(\Delta t^4) \quad (2.4)$$

In this way, the position of the atom as it evolves by a time step of  $\Delta t$  can be predicted. This method is however very popular among people who perform MD simulations due to its simplicity, accuracy and stability. However it requires more computational effort as we have to save the values of positions at two previous time steps i.e. 't' and  $t - \Delta t$ . The associated truncation errors with this method are of the order of  $\Delta t^4$ . Another limitation with this method is that it cannot generate the velocities directly. The velocity can however be estimated as:  $v(t - \Delta t) = \frac{r(t) - r(t - \Delta t)}{\Delta t}$ . The verlet algorithm thus conserves the total energy of the system very well at all stages. However it comes at the cost of accuracy and stability. This problem can be overcome by employing the 'Velocity Verlet Algorithm' which can predict both the position and velocity synchronously i.e. at the same time steps and require only the initial positions and velocities to initiate. This algorithm is explained in details in the following subsection.

## Velocity Verlet Algorithm

In this method a smart ploy is employed to calculate accurately the velocities. Instead of calculating the velocities every time step, the calculation is made every half step using values of position and acceleration at the previous step.

$$v(t + \frac{\Delta t}{2}) = v(t) + \frac{1}{2}a(t)\Delta t \quad (2.5)$$

Following that we calculate the position and acceleration at the next full time step.

$$r(t + \Delta t) = r(t) + v(t)\Delta t + \frac{1}{2!}a(t)\Delta t^2 \quad (2.6)$$

$$a(t + \Delta t) = -\frac{1}{m} \frac{\delta U}{\delta r} r(t + \Delta t) \quad (2.7)$$

Then using all these values, the velocity after another half-step (which essentially is a full step) is predicted as follows :

$$v(t + \Delta t) = v(t + \frac{\Delta t}{2}) + \frac{1}{2}a(t + \Delta t)\Delta t \quad (2.8)$$

Next in order to calculate more accurately the dynamics such as to represent a real world system, it is important to introduce a Langevin damping in these equations. So the Eqn. 1.6 can be re-written as :

$$r(t + \Delta t) = r(t) + v(t)\Delta t + \frac{1}{2!}(a(t) - \lambda v(t))\Delta t^2. \quad (2.9)$$

In this way the dynamical evolution of the atoms in the dislocation along the kink propagation and thus the corresponding configurations can be estimated.

### 2.3.3 NEB method to estimate the MEP

In the Nudged Elastic Band (NEB) [133, 134] method, numerous images or replicas of the system are created and connected together by springs such as to represent a discrete path from an initial configuration I to a final configuration F. A NEB calculation can be started by

assuming a linear pathway between I and F and later an optimization algorithm can be applied to relax the images till they converge with the MEP. For our simulations, we apply the NEB to compute the MEP of the glide of the screw dislocation introduced in the simulation cell between an initial and a final state, both of which are states of local minima on the potential energy surface produced by the application of an EAM.

We can represent the string of images as  $[R_0, R_1, R_2, \dots, R_N]$  with fixed end points  $I = R_0$  and  $F = R_N$ . The N-1 intermediate replicas can be adjusted by the optimization algorithm. An object function can be used to define the whole process :

$$S(R_1, R_2, \dots, R_N) = \sum_{i=1}^{N-1} E(R_i) + \sum_{i=1}^N \frac{k}{2} (R_i - R_{i-1})^2 \quad (2.10)$$

This represents an elastic band made up of N-1 beads and N springs with the same spring constant k. The band is made to string between the two fixed endpoints. However a couple of problems are encountered. Firstly, the elastic band gets pulled away from the curved regions of the MEP due to the component of the spring force perpendicular to the path. Secondly the replicas slide down towards the endpoint resulting in lowest resolution around the saddle point where it should ideally be maximum. This down sliding happens due to the parallel component of the real force arising from the interaction between the atoms [133, 134].

### The technique of 'Nudging'

Both the problems of corner-cutting and sliding-down, mentioned in the previous sub-section can be countered by a force projection technique or 'nudging'. The force on each image is adjusted to comprise of only the parallel component of the spring force and perpendicular component of the true force.

$$F = -\nabla E(R_i)|_{\perp} + F_i^s \cdot \hat{\tau}_i \hat{\tau}_i \quad (2.11)$$

where  $\nabla E(R_i)$  is the gradient of energy corresponding to the atomic configuration of atoms in image 'i' and  $F_i^s$ , the spring force acting on image i. The perpendicular component may be separated out by subtracting the parallel component as follows:

$$\nabla E(R_i)|_{\perp} = \nabla E(R_i) - \nabla E(R_i) \cdot \hat{\tau}_{\parallel} \hat{\tau}_{\parallel} \quad (2.12)$$

It is also essential to ensure equal spacing between the replicas as the same spring constant  $k$  is used for all the springs. Even in high curvature regions where the angle between  $R_i$  and  $R_{i-1}$  deviates quite a bit from 0, this spacing can be maintained by evaluating the spring force as:

$$F_i^s|_{\parallel} = k(|R_{i+1} - R_i| - |R_i - R_{i-1}|) \hat{\tau}_i \quad (2.13)$$

## Estimation of the path tangent

The simplest way to estimate the tangent at the image i is by using the adjacent images  $R_{i+1}$  and  $R_{i-1}$  along the pathway of the NEB as follows:

$$\hat{\tau}_i = \frac{R_{i+1} - R_{i-1}}{|R_{i+1} - R_{i-1}|} \quad (2.14)$$

But a more accurate way is to bisect the two unit vectors

$$\hat{\tau}_i = \frac{R_i - R_{i-1}}{|R_i - R_{i-1}|} + \frac{R_{i+1} - R_i}{|R_{i+1} - R_i|} \quad (2.15)$$

and then normalize  $\hat{\tau}_i = \tau/|\tau|$  in order to ensure the equi-spacing of images even in large curvature regions. The computation of tangents is performed periodically every 5 to 10 steps in order to avoid some artefacts that appear when the correction is performed too frequently.

## The NEB applied to our simulation cell

The value of the spring constant is chosen as  $10 \text{ N}/\text{\AA}$  and the number of system replicas is fixed at 50. We then run the NEB code with an applied stress below the Peierls stress such that the minimum energy path (MEP) is computed when the dislocation motion is hindered by a barrier. In the case of the formation of kink pair on long dislocation below the Peierls stress we need to construct the initial dislocation path such as to break the translational symmetry of the straight dislocation which is due to thermal fluctuations. To obtain the intermediary states of the dislocation along the NEB path we combine the atom coordinates of starting and final states along the dislocation line. The coordinates are those of starting state along the dislocation line except in a central segment where the length depends of the rank in the NEB path, where the coordinates are those of final state. The successive NEB images correspond to dislocation profiles which are presented in Fig.1.2(a). The precise MEP which is plotted according to dislocation position is shown in Fig.1.2(b)

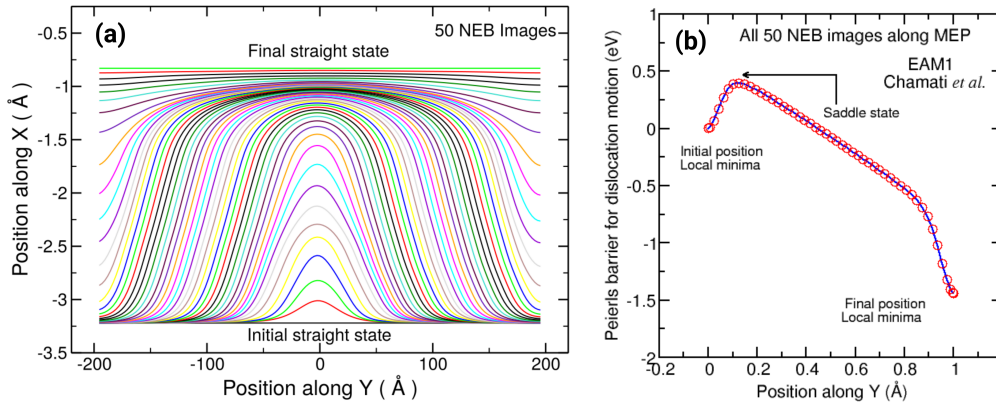


Figure 2.2: a) Profile of the dislocation in different NEB images. b) Minimum energy path (MEP) between the initial and final dislocation states with the corresponding saddle state.

The position of the dislocation is determined as the barycenter of the atomic positions weighted by  $\Delta_i$ . For the screw dislocation the position along Y axis i.e. the dislocation line is given by:

$$Y_D = \frac{1}{\sum_i \Delta_i} \sum_i y_i \Delta_i, \quad (2.16)$$

whereas its position along z axis is given by :

$$Z_D = \frac{1}{\sum_i \Delta_i} \sum_i z_i \Delta_i, \quad (2.17)$$

where  $y_i$  and  $z_i$  are the coordinates of atom  $i$  along Y and Z axis, respectively. These computations are performed in the regions excluding the surfaces or very close to the surfaces. The saddle point of the first NEB profile corresponds to the originating point of the nucleation of a kink pair on the dislocation, which propagates both ways along the dislocation line and finally leads the dislocation to cross the Peierls barrier and move into the next Peierls valley.

## 2.4 Simulation cell extension

The simulation cell used for the NEB computations is limited in length along the dislocation line; 160 b in length which is equivalent to  $400 \text{ \AA}$  or  $0.04 \mu\text{m}$ . The reason being that numerous system replicas are needed to compute accurately the MEP, thus limiting the number of atoms that can be handled computationally. This could lead to the exclusion of appearance of some phenomena that could probably occur as the kinks propagate further along the dislocation line beyond the length considered in our simulations. Also the kinks require to traverse much longer distances in order to reach steady velocity.

In order to overcome this, we first extended our simulation cell by considering periodic boundary conditions along the y direction i.e. by taking a simulation cell (same as for performing NEB computations) and extending it twice each in positive and negative y-directions. In this way we constructed a new simulation cell which is five times as long as the original cell. The length of the extended simulation cell is  $2000 \text{ \AA}$  or  $0.2 \mu\text{m}$  which is comparable to the length of dislocations observed by D. Caillard in his experiments. In order to be as close as possible to the experimental set-up, we fixed the atoms on the end surfaces of the long simulation cell along the dislocation line. As described in Fig.1.3, we then picked up the first saddle state configuration of the dislocation from the NEB computation and placed it in the central cell of

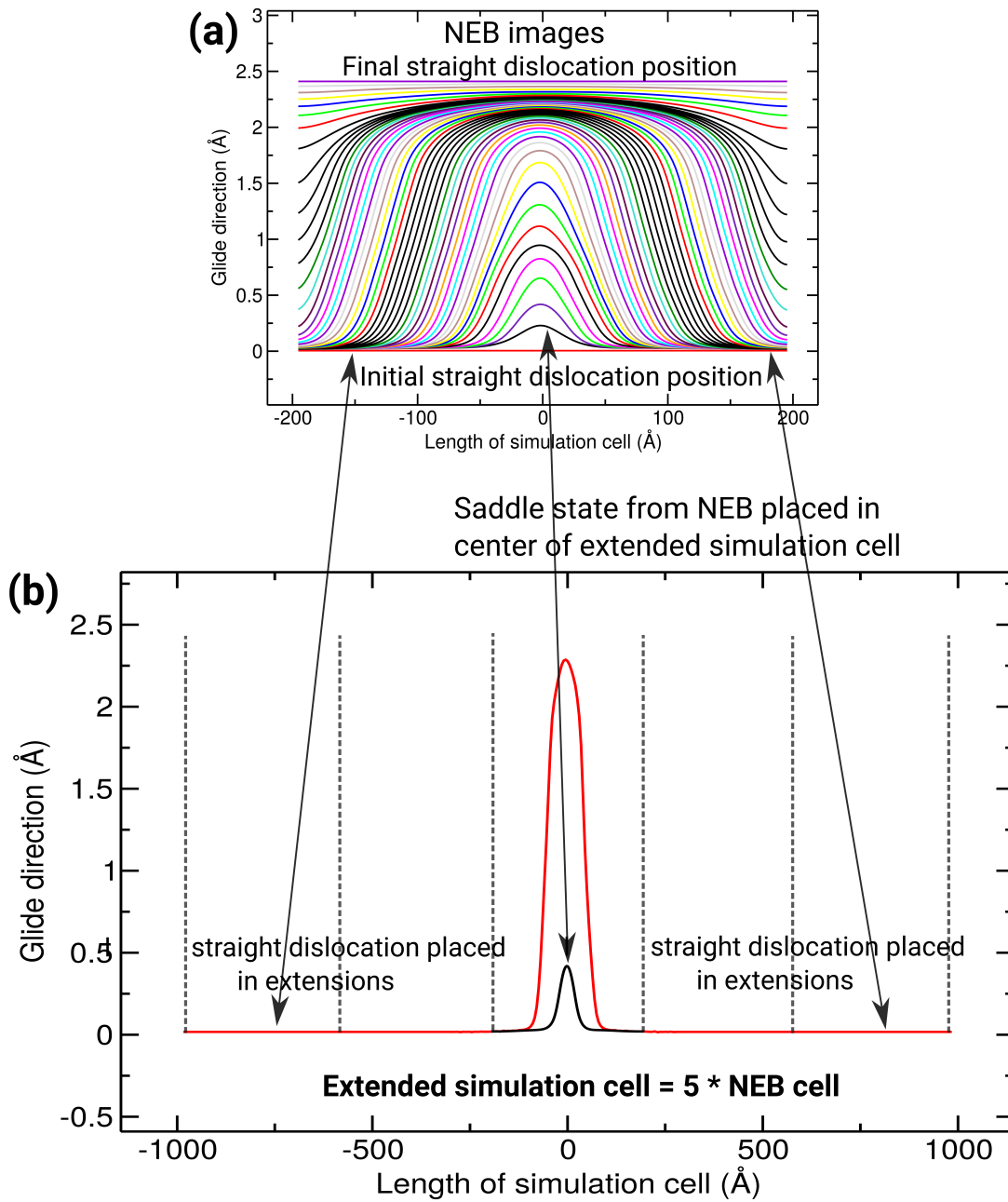


Figure 2.3: a) Typical NEB simulation cell used to compute the saddle state of the dislocation and b) Extended simulation cell with NEB saddle state placed at the center and straight dislocation segments placed on both sides several times.

the extended cell. We then placed 2 straight dislocation segments each on either side of the central cell which leads to a final extended cell, 5 times larger than the NEB one, with a kink pair right at the middle along the dislocation line.

This trick allows us to relaunch new MD simulations from a saddle state without having to wait infinitely for the occurrence of a rare event like kink pair nucleation whose time scales are of the order of milli-seconds whereas MD can be performed only upto nano-seconds. It is important also to note that we are not interested in viewing the process of how the kink pair nucleation took place in the first place. What concerns us is what happens after i.e. once the kink pair is formed, how it propagates along the dislocation line and how finally the dislocation glides to the next Peierls valley and so on.

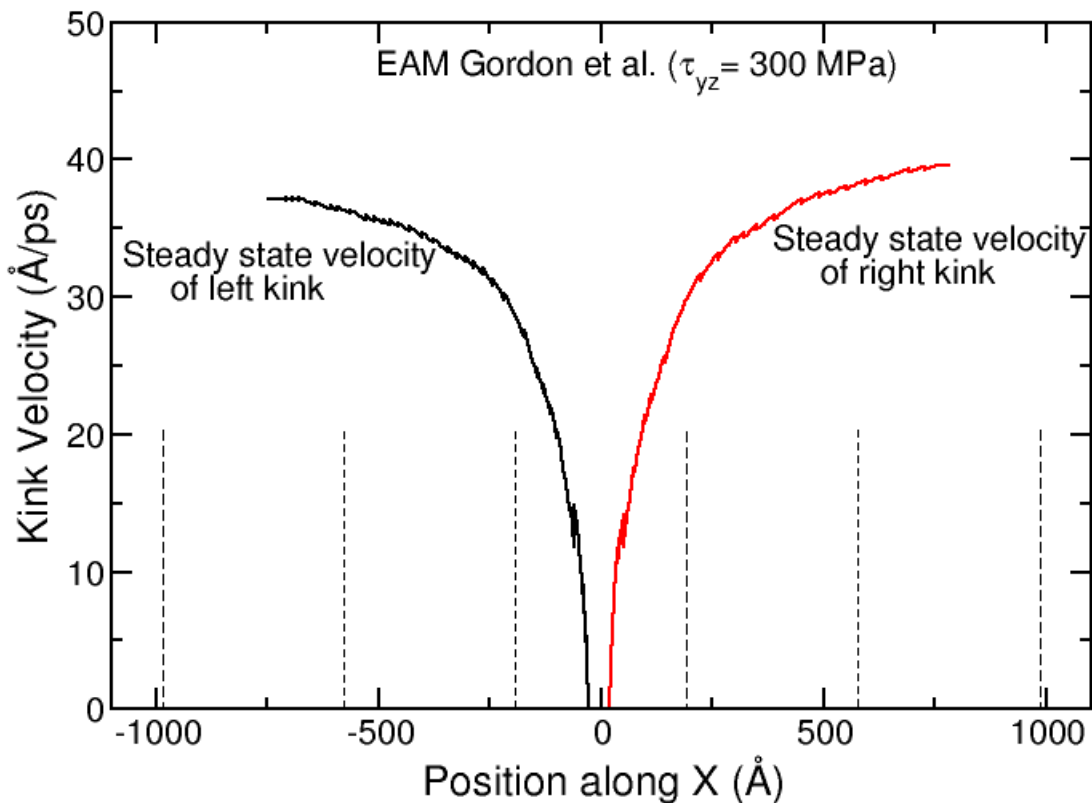


Figure 2.4: Left and right kinks attaining steady state velocity at positions that justify the simulation cell extension.

In Fig. 1.4, we have plotted the velocity of left and right kinks with respect to their positions in the extended simulation cell. The results plotted are from test simulations that were performed to investigate the required length of the extended simulation cell. It can be seen that both the left and right kinks reach steady state velocities after propagating with gradually increasing

velocity initially. This leads to the conclusion that the chosen length of the extended simulation cell is quite good to proceed with further simulations. In order to be sure, we chose to repeat our simulations with a longer extended simulation cell (7 times the NEB cell). But the analysis didn't yield any changes in the end results as obtained with the first extended simulation cell. This led to the conclusion that the dislocation length of 5 times the NEB cell is good enough to accurately simulate the phenomenon we are interested in. The kink velocities in Fig. 1.4, are calculated from the time integrated MD profiles of the screw dislocation that indicate the successive positions of both the left and right kinks along the dislocation line with respect to the time. By knowing the change in position with respect to the time, we are able to trace the velocities at all stages. Here too the velocities are computed every 5 or 10 steps to avoid artefacts resulting from a too frequent determination of velocities.

# Chapter 3

## Atomic scale study of the screw dislocation glide in bcc Iron

We performed Molecular Dynamics (MD) simulations using the extended simulation cell that we created as detailed in the previous chapter. Starting from a long straight dislocation with a kink pair at the center of the dislocation, the simulations were launched with combinations of different levels of applied shear stresses, different temperatures and using different EAM inter atomic potentials EAM1 [107], EAM2 [99] and EAM3 [98].

### 3.1 Kink propagation in standard Peierls Nabarro mechanism

In this section we examine the different cases where we observed the standard Peierls Nabarro mechanism [9] in our simulations. This mechanism refers to the standard process of dislocation glide wherein the dislocation moves in steps from one Peierls' valley [9] to the adjacent and so on, resulting in an overall glide from one part of the crystal to another. Such a step involves first the formation of a pair of kinks on the dislocation by the movement of some of the atoms to the next Peierls valley [9]. This is followed by the propagation of the kinks outwards along

the dislocation line, i.e. the atoms move along the direction of the burger's vector parallel to the dislocation line and more atoms start moving in the crystal rows contiguous to the dislocation line. Finally the entire dislocation moves to the next Peierls valley [9] when the kinks have traversed the entire length of the dislocation. For this process, the dislocations need to overcome an energetic barrier called Peierls' barrier [9]. Both the applied shear stress along the dislocation glide plane and temperature in the crystal play a part in this process by providing the necessary forces and energies to the atoms, first for the formation of kink pairs and then for the propagation of kinks along the dislocation line, which leads to the glide of the entire dislocation in a direction perpendicular to the motion of kinks.

As a result of the applied stress, a force known as the Peach-Koehler [135] force  $\tau_{yz}b$  starts acting per unit length of the dislocation. The temperature provides the necessary impetus for the formation and propagation of kink pairs. By knowing the distance traversed by the kinks i.e. the distance between the two kinks at all times, we can assert the distance by which the entire dislocation has progressed. Denoting by  $L_k$ , the instantaneous distance between the two kinks, the distance progressed by the dislocation can be expressed as  $\frac{L_k}{L}a$ ,  $a$  ( $a = \sqrt{2/3} a_0$ ) being the distance between two adjacent Peierls valleys and  $L$  the dislocation length. Thus the work done by the Peach-Koehler force to cause the dislocation motion can be expressed as :

$$W = \tau_{yz}b \frac{L_k}{L} aL = \tau_{yz}bL_k a. \quad (3.1)$$

### 3.1.1 Simulations for $\mathbf{T} = (0 + \epsilon) \mathbf{K}$

In this section we describe the simulations carried out close to 0 K. It means that initially we did not apply any kinetic energy to the atoms in the simulation cell representing the crystal. However, as we have considered our system a NVE microcanonical ensemble (fixed number of atoms, total volume and total energy of the system at all times) and started our simulations from a transition state (one of the local enthalpy maximas) corresponding to the kinked dislocation at the unstable equilibrium state, there exists an initial potential energy  $\delta E$  and hence an

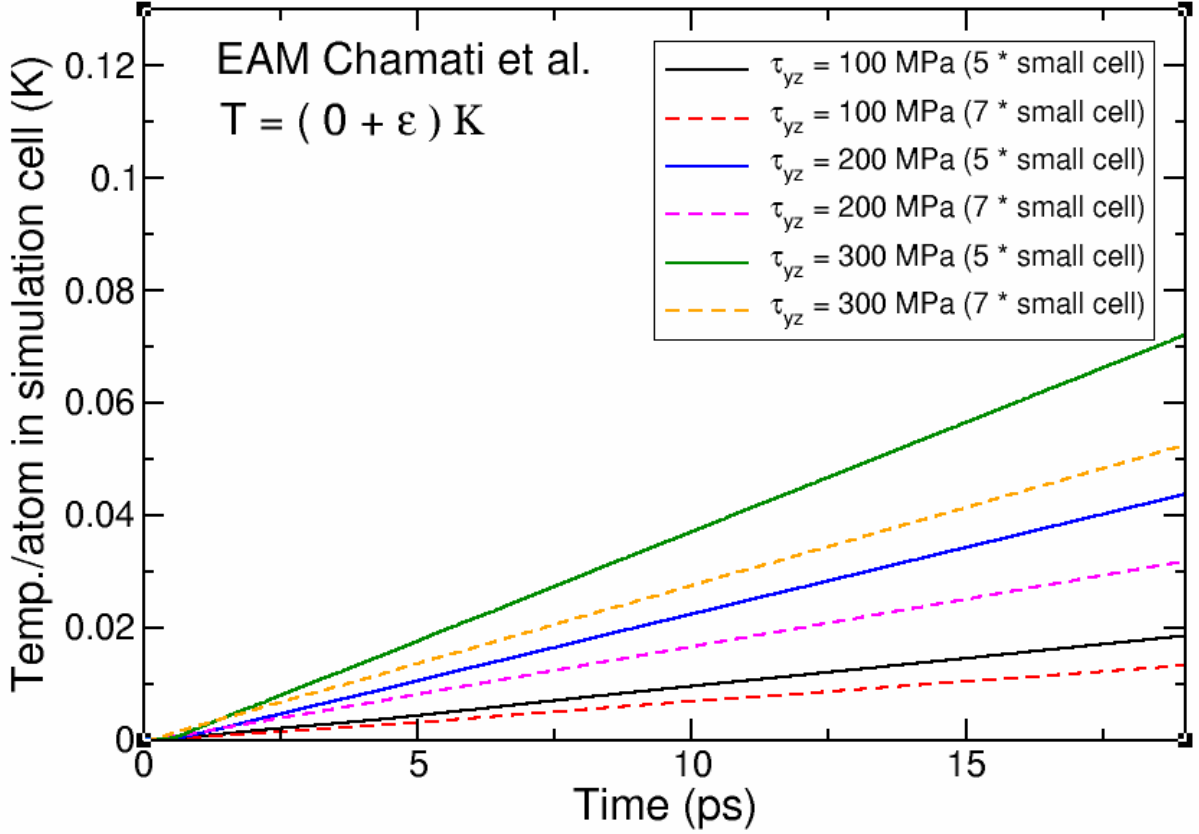


Figure 3.1: Plot of temperature per unit atom as a function of time for two different extended simulation cells i.e. 5 and 7 times the original cell, at different applied shear stresses,  $\tau_{yz} = 100$  MPa,  $\tau_{yz} = 200$  MPa and  $\tau_{yz} = 300$  MPa respectively for temperature close to 0 K i.e.  $T = (0 + \epsilon)$  K, for EAM1 [107].

additional minimal initial temperature  $\epsilon$  at all times arising from the conservation of energy.

It can be expressed as :

$$\epsilon = \frac{2\delta E}{3k_B N_{at}}. \quad (3.2)$$

As a result it can be said that the simulations were carried out at a temperature,  $T = (0 + \epsilon)$  K. The kinks gradually start to propagate along the dislocation line due to the action of the applied stress manifesting as the Peach-Koehler [135] force  $\tau_{yz}b$  described earlier. The work done by this Peach-Koehler [135] force  $\tau_{yz}b$ , is dissipated in atomic vibrations. Denoting the total number of atoms in the simulation cell by  $N_{at}$ , the total kinetic energy of the system,  $E_c$  can be expressed as :

$$E_c = N_{\text{at}} \frac{3}{2} k_B \epsilon_1, \quad (3.3)$$

where  $\epsilon_1$  is the increase in temperature of the system as a whole due to the applied stress. Equating the kinetic energy of the system with the equivalent work done by the Peach-Koehler force we have :

$$N_{\text{at}} \frac{3}{2} k_B \epsilon_1 = \tau_{yz} b L_k a. \quad (3.4)$$

By re-arranging the terms, we get an equation in terms of  $\epsilon_1$  :

$$\epsilon_1 = \frac{2\tau_{yz} b a L_k}{3k_B N_{\text{at}}}. \quad (3.5)$$

So from equation 3.2 and equation 3.5, the overall temperature  $\epsilon_{\text{total}}$  of the simulation cell at all stages can be estimated :

$$\epsilon_{\text{total}} = \epsilon + \epsilon_1 = \frac{2}{3k_B N_{\text{at}}} (\delta E + \tau_{yz} b a L_k). \quad (3.6)$$

Thus from equation 3.6, we can conclude that the effective temperature in the system increases with increase in the distance  $L_k$  between kinks i.e. with passage of time and also with the applied stress  $\tau_{yz}$ . However it decreases if we increase the total number of atoms in the simulation cell. In order to verify this, we performed simulations starting from a temperature close to 0 K (i.e.  $(0+\epsilon)$  K) for different lengths (thus varying the total number of atoms) of the extended simulation cell. Two different lengths of the extended simulation cell along  $y$ , i.e. 5 and 7 times the NEB simulation cell (described in the previous chapter) respectively were used for the same level of applied stress. The simulations were carried out for three different stress levels: 100 MPa, 200 MPa and 300 MPa respectively for both lengths of the extended simulation cell.

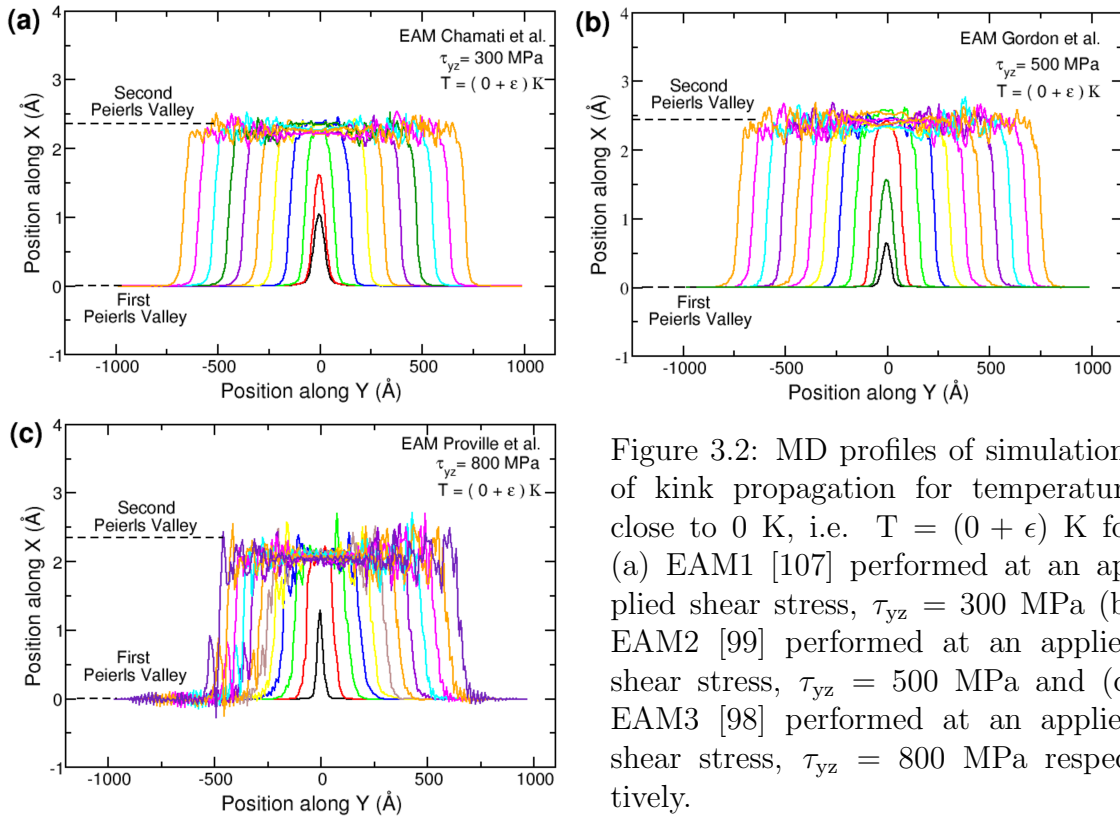


Figure 3.2: MD profiles of simulations of kink propagation for temperature close to 0 K, i.e.  $T = (0 + \epsilon)$  K for (a) EAM1 [107] performed at an applied shear stress,  $\tau_{yz} = 300$  MPa (b) EAM2 [99] performed at an applied shear stress,  $\tau_{yz} = 500$  MPa and (c) EAM3 [98] performed at an applied shear stress,  $\tau_{yz} = 800$  MPa respectively.

The effective temperature per atom in the simulation cell as a function of time has been plotted for EAM1 [107] in Fig. 3.1. Here we observe that for the case of 100 MPa, the temperature per atom increases with the passage of time for both lengths of the extended simulation cell. For the length 5 times the NEB simulation cell (black line in figure), the temperature per atom increases to 0.019 K during the length of the simulation possible and for the length 7 times the NEB simulation cell (red dashed line in figure), the temperature per atom increases to 0.013 K/atom. For the case of 200 MPa, these values are 0.042 K (Blue line) and 0.031 K (magenta dashed line) respectively and for the case of 300 MPa, these values are 0.071 K (Green line) and 0.051 K (orange dashed line) respectively. For all the three stress levels, we see that the temperature decreases when the number of atoms in the simulation cell increases, i.e. for the longer extended simulation cell. The temperature is also higher for the case of higher applied stress (for same lengths of extended simulation cell) which is in accordance with the prediction of Eqn. 3.5.

We also see that among all the different individual cases in Fig. 3.1, the highest value of

temperature increase i.e. 0.071 K is almost negligible in comparison to 1 K (0.071K). Hence we could infer that our simulations were carried out almost at 0 K, or as stated very close to 0 K. In Fig. 3.2, we have plotted the MD profiles of the dislocation at definite intervals of time evolution for simulations performed with EAM1 [107] at an applied shear stress  $\tau_{yz} = 300$  MPa, with EAM2 [99] at an applied shear stress  $\tau_{yz} = 500$  MPa and with EAM3 [98] at an applied shear stress,  $\tau_{yz} = 800$  MPa respectively. We can see for all the three cases that the kink pair initially grows in size gradually from the saddle state till it is in the adjacent Peierls valley [9] and then it propagates along the dislocation line as expected in standard theory. Here we note that for all the three EAMs, the simulations were carried out at stress levels lower than the Peierls stresses [9], i.e. the stress needed to overcome the crystal resistance in the absence of thermal fluctuations. The Peierls stress [9] values predicted by atomistic simulations for EAMs: EAM1 [107], EAM2 [99] and EAM3 [98] are 600 MPa, 900 MPa and 1000 MPa respectively.

Following these simple set of simulations to verify our calculations with standard theory, we proceeded to test our simulations again, this time with the application of temperature to the crystal lattice. The results have been described and discussed in the following section.

### 3.1.2 Simulations at $T = 5$ K and $T = 10$ K

In order to introduce temperature in our simulations, we designed our code to attain the desired temperature by designating the initial velocities of the atoms according to a Maxwell-Boltzmann random distribution. This process has a stronger statistical basis than using a thermostat because it relies on the real atomistic heat bath of a larger system rather than any particular thermostat algorithm.

Referring once more to Fig. 3.1, we observe that the increase of effective temperature per atom  $\epsilon_0$  along MD time steps is much smaller compared to the applied temperatures 5 K and 10 K ( $\epsilon_0 = 0.071\text{K} \llll 5\text{K}, 10\text{K}$ ). Hence the effect of the initial temperature in the system can be neglected. We have considered the same three cases as in the previous section (simulations close to 0 K), with the only difference being that small temperatures,  $T = 5$  K and  $T = 10$  K have been applied to the simulation cell in two different sets of simulations. The profiles of

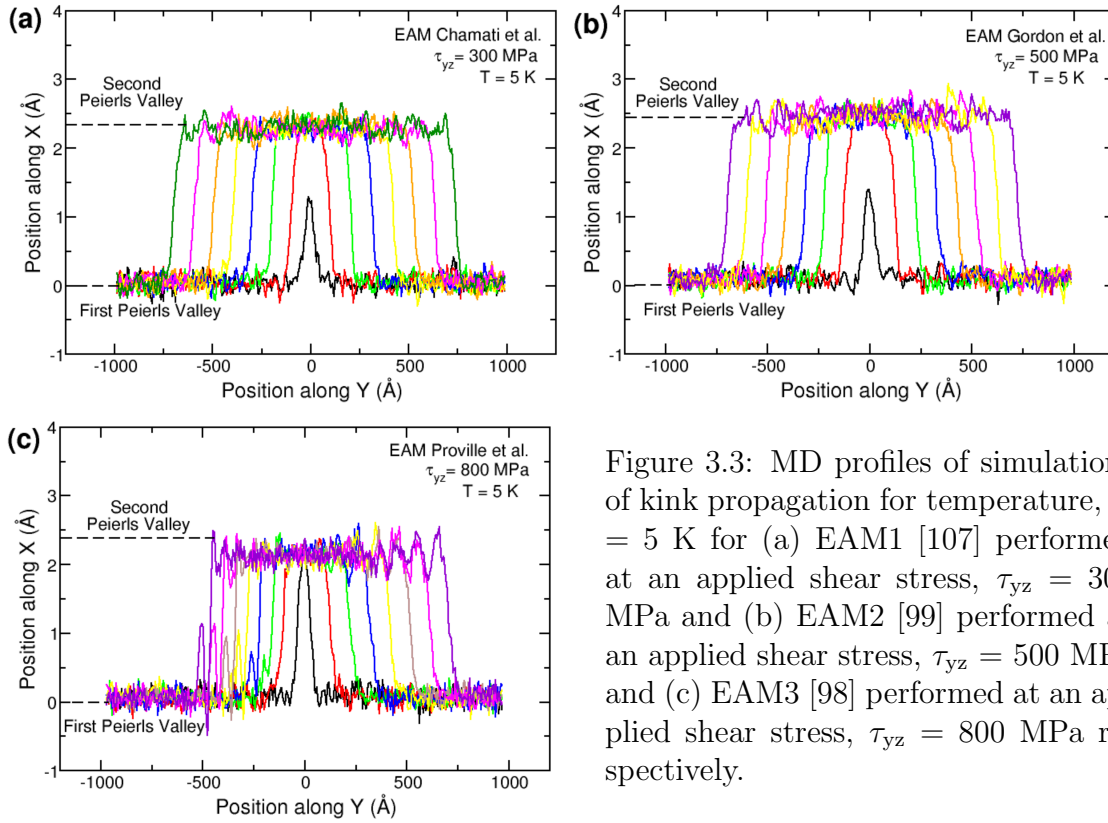


Figure 3.3: MD profiles of simulations of kink propagation for temperature,  $T = 5$  K for (a) EAM1 [107] performed at an applied shear stress,  $\tau_{yz} = 300$  MPa and (b) EAM2 [99] performed at an applied shear stress,  $\tau_{yz} = 500$  MPa and (c) EAM3 [98] performed at an applied shear stress,  $\tau_{yz} = 800$  MPa respectively.

dislocation along with the kink propagation are very crude and unclear to the naked eye when plotted at the same time interval as in the previous case of zero applied temperature. This can be attributed to the fact that the application of temperature significantly increases the initial velocities and gradually the kinetic energies of the atoms causing larger local vibrations of all the atoms along the dislocation. Therefore we averaged the dislocation profile over 1000 time steps in order to have a more clear view. These results have been plotted in Fig. 3.3 (for  $T = 5$  K) and Fig. 3.4 (for  $T = 10$  K) respectively.

For both sets of simulations, again the standard Peierls Nabarro mechanism was observed every time. The profiles also appeared quite similar to the respective profiles in the case without any applied temperature. However, it is not visually possible to know if the application of temperature has any effect on the velocities of the propagating kinks, which in turn could effect the glide velocity of the entire dislocation. Hence we proceeded to analyse the kink velocities with and without the application of temperature for all the three EAMs : EAM1 [107], EAM2 [99] and EAM3 [98].

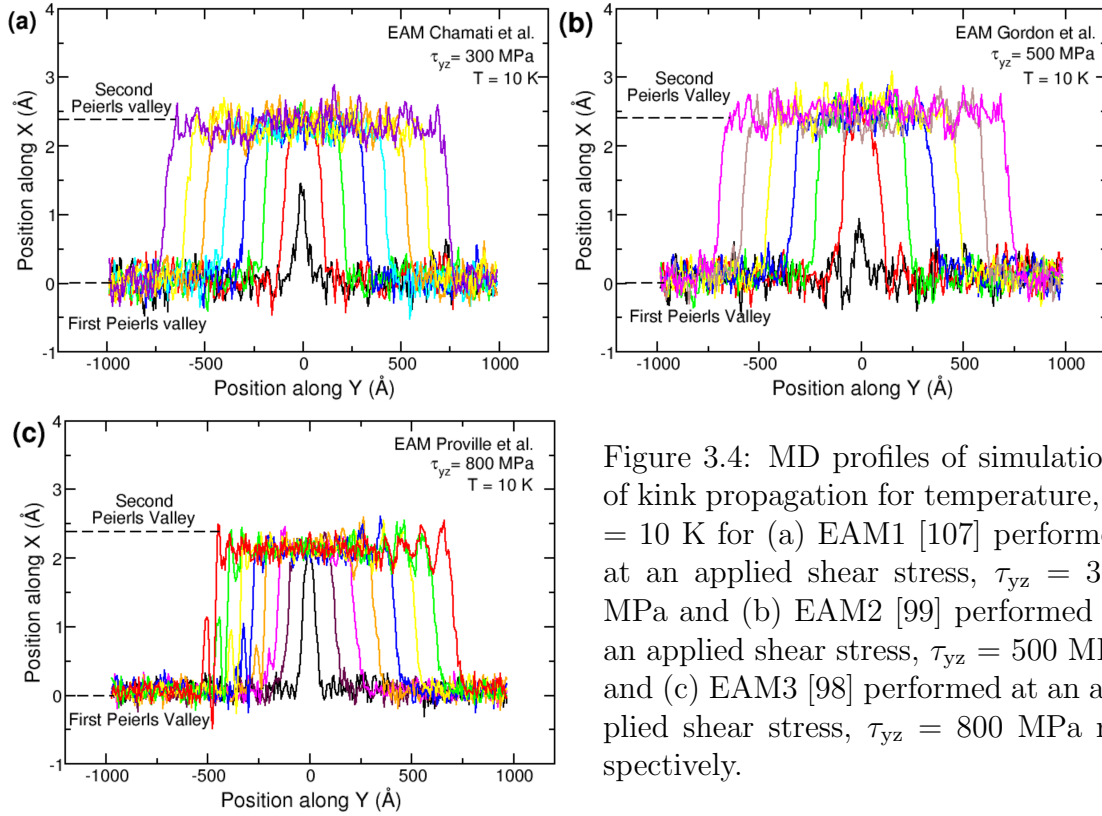


Figure 3.4: MD profiles of simulations of kink propagation for temperature,  $T = 10$  K for (a) EAM1 [107] performed at an applied shear stress,  $\tau_{yz} = 300$  MPa and (b) EAM2 [99] performed at an applied shear stress,  $\tau_{yz} = 500$  MPa and (c) EAM3 [98] performed at an applied shear stress,  $\tau_{yz} = 800$  MPa respectively.

### 3.1.3 Plot of kink velocity as a function of time

Although there wasn't any significant visible difference in the profiles of kink propagation by the introduction of small temperatures in our simulations, we proceeded to investigate closely the effect of temperature on the velocities of the propagating kink pairs. Previous studies have established some effects of temperature on the velocities of propagating kinks. For decades, after Leibfried [136] predicted that temperature decreases the velocity of kinks, it began to be widely accepted. However recently in 2013, Swinburne contradicted this and predicted that the friction parameter, hence the velocity of kinks is temperature independent. The main findings and predictions of these two theories are described in a detailed manner before comparing our simulation results with such predictions.

G. Leibfried, in one of the earliest atomistic scale works [136] on dislocation velocities had predicted that the kink velocities in screw dislocations are temperature dependent and they decrease with increasing temperature. At temperatures above one fifth of the Debye temperature, the drag due to the interaction of dislocations with phonons starts to be significant and is quite

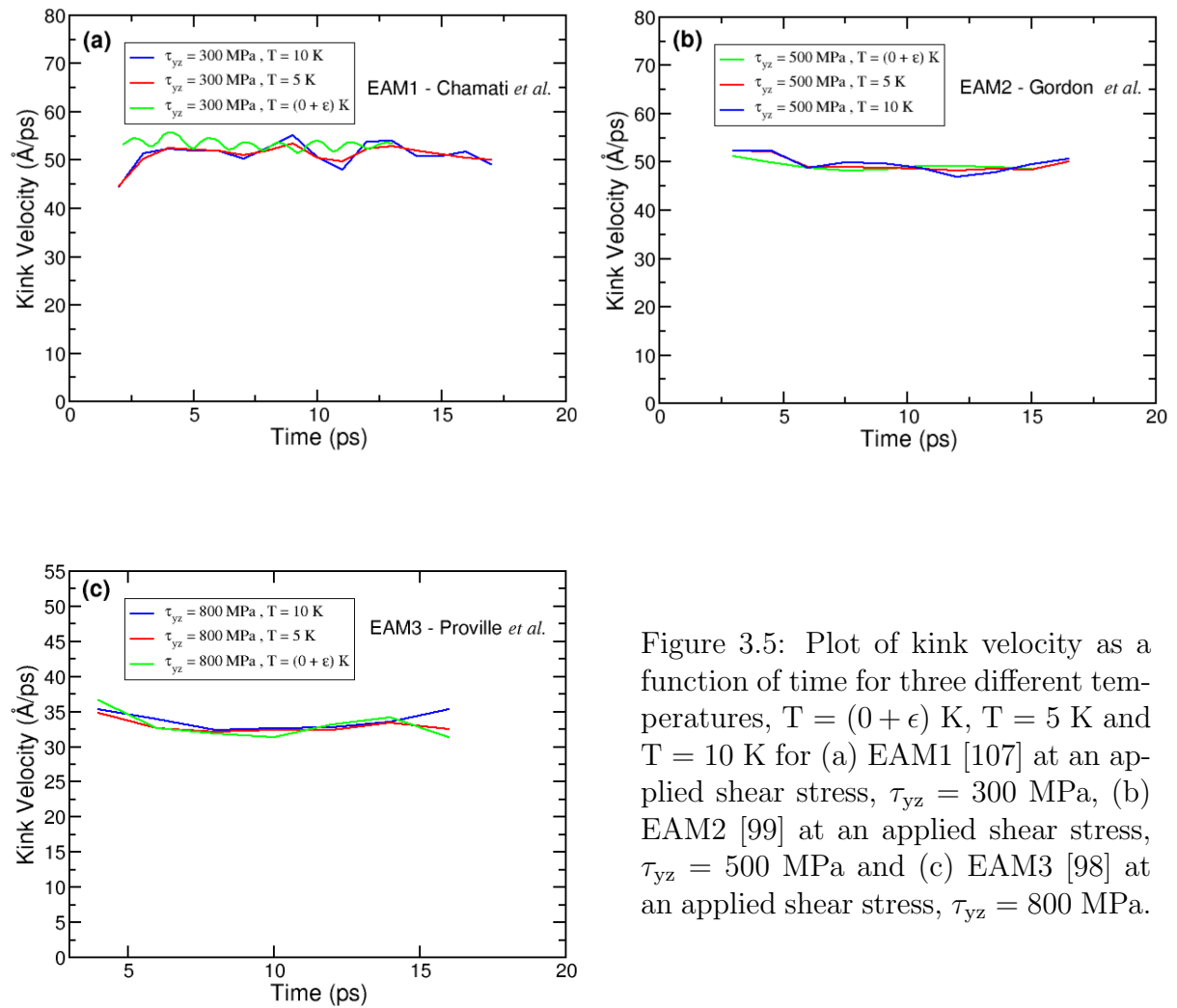


Figure 3.5: Plot of kink velocity as a function of time for three different temperatures,  $T = (0 + \epsilon)$  K,  $T = 5$  K and  $T = 10$  K for (a) EAM1 [107] at an applied shear stress,  $\tau_{yz} = 300$  MPa, (b) EAM2 [99] at an applied shear stress,  $\tau_{yz} = 500$  MPa and (c) EAM3 [98] at an applied shear stress,  $\tau_{yz} = 800$  MPa.

prominent in the regime of practical temperatures. The findings of Leibfried was employed and confirmed by E. Bitzek and P. Gumbsch [137] while studying the dynamics of dislocations in a face centred cubic (FCC) metal. They employed two different embedded atom method (EAM) potentials by Angelo et al. [138] and Mishin's potential [139] to study FCC Nickel and used a simple slab geometry to carry out atomistic scale simulations in order to estimate the Peierls stress, the effective mass, the line tension (described in the previous chapter) and the phonon drag coefficient  $B_{ph}$  for both edge and screw dislocations. They studied the dislocation-obstacle interactions for a dislocation intersecting an array of voids and found a noticeable effect caused due to inertial overshooting. To study this effect, they developed a dynamic line tension model (described in the previous chapter) which could be used to estimate the magnitude of inertial effects when dislocations interact with localized obstacles depending on obstacle strength, spacing and temperature. Leibfried [136] had proposed the damping coefficient or the phonon drag coefficient  $B_{ph}$  to quantify the deceleration by viscous drag. According to Leibfried [136], the phonon drag coefficient  $B_{ph}$  at temperature T, is expressed as :

$$B_{ph} = \frac{3kTz}{20c_t b^2}. \quad (3.7)$$

,

where k is the Boltzmann's constant and z is the number of atoms per unit cell,  $c_t$  is the speed of transverse waves and b is the Burger's vector. In the regime where inertia can be neglected, the work of the Peach-Koehler force is dissipated through dislocation damping by phonons, which leads to the equation:  $B_{ph}v = \tau_{yz}b$ . Thus it can be inferred from equation 3.7, that according to Leibfried, the phonon drag coefficient increases with increasing temperature. It is also evident that as v is inversely proportional to  $B_{ph}$ , the corresponding velocity decreases with temperature. Bitzek and Gumbsch [137] utilized the steady state velocity  $v_{ss}$  reached after an acceleration period to determine the drag coefficient  $B = \tau_{yz}b/v_{ss}$  for different temperatures T for non relativistic motion of dislocations i.e. for  $v_{ss} \leq c_t/3$ . The temperature dependence of B for edge dislocations was found to be in good agreement with Leibfried's estimate. Whereas for the case of non-linear photon scattering in screw dislocations, the drag coefficients were found

to be higher as expected.

Leibfried's model was also used and illustrated by D.L. Olmsted *et al.* [140] in their studies on dislocation mobility. Molecular Dynamics simulations were employed to study the velocities of edge and screw dislocations in pure Al and Ni, both of which have face centred cubic (FCC) crystal structures unlike Fe. The velocities of the dislocations were plotted as a function of  $\frac{\sigma}{T}$  keeping  $\sigma$  constant and varying the temperature. In most cases a regime was observed where the velocity is linear in  $\frac{\sigma}{T}$ . Thus for a given material, the behaviour in this linear regime could be captured by a single parameter  $\frac{B}{T}$ , the values of which were obtained and tabulated. For both the cases of screw dislocation in pure Al and pure Ni, the  $\frac{B}{T}$  value decreased with the decrease in  $\frac{\sigma}{T}$  values. Now as  $\sigma$  is constant a decrease in  $\frac{\sigma}{T}$  value implies an increase in temperature and the corresponding decrease in  $\frac{B}{T}$  value implies an increase in the value of B. This is in accordance with the theoretical prediction of Leibfried's model.

A contrasting behaviour has however been predicted by T.D. Swinburne *et al* [10]. with regards to the velocity of kinks. They concluded that the kink velocity is independent of temperature which has been explained in the following part of this paragraph. For the case of Body Centred Cubic (BCC) Iron (Fe), the formation energy of kink pairs is much larger compared to the thermal energy. The time scales attainable in MD depends on the stress level close to  $\tau_P$  (Peierls stress) for which the barrier for kink pair propagation is smaller than kT. Hence it is impossible to get statistically significant data on the simulated kink nucleation. This is why researches resort to the use of very high deformation rates (6 orders of magnitude [136]) in simulations as compared to experiments in order to induce the formation of a kink pair. But on the other hand it has also been established that the dislocation core structure [129] and Peierls barrier change with applied stress. The possibility of a degenerate dislocation core structure had however been ruled out by DFT based calculations [74]. In order to avoid a degenerate core structure, Swinburne applied the well known discrete Frenkel-Kontorova-Langevin (FKL) [141-144] model with a coarse graining approach that treats the dislocation line as an elastic string sitting in a periodic substrate potential [145]. He fixed the nodes as per the spacing of the atomic planes normal to the dislocation line, essentially assigning a core position in each such plane essential to reproduce the structure and dynamics of the dislocations that were

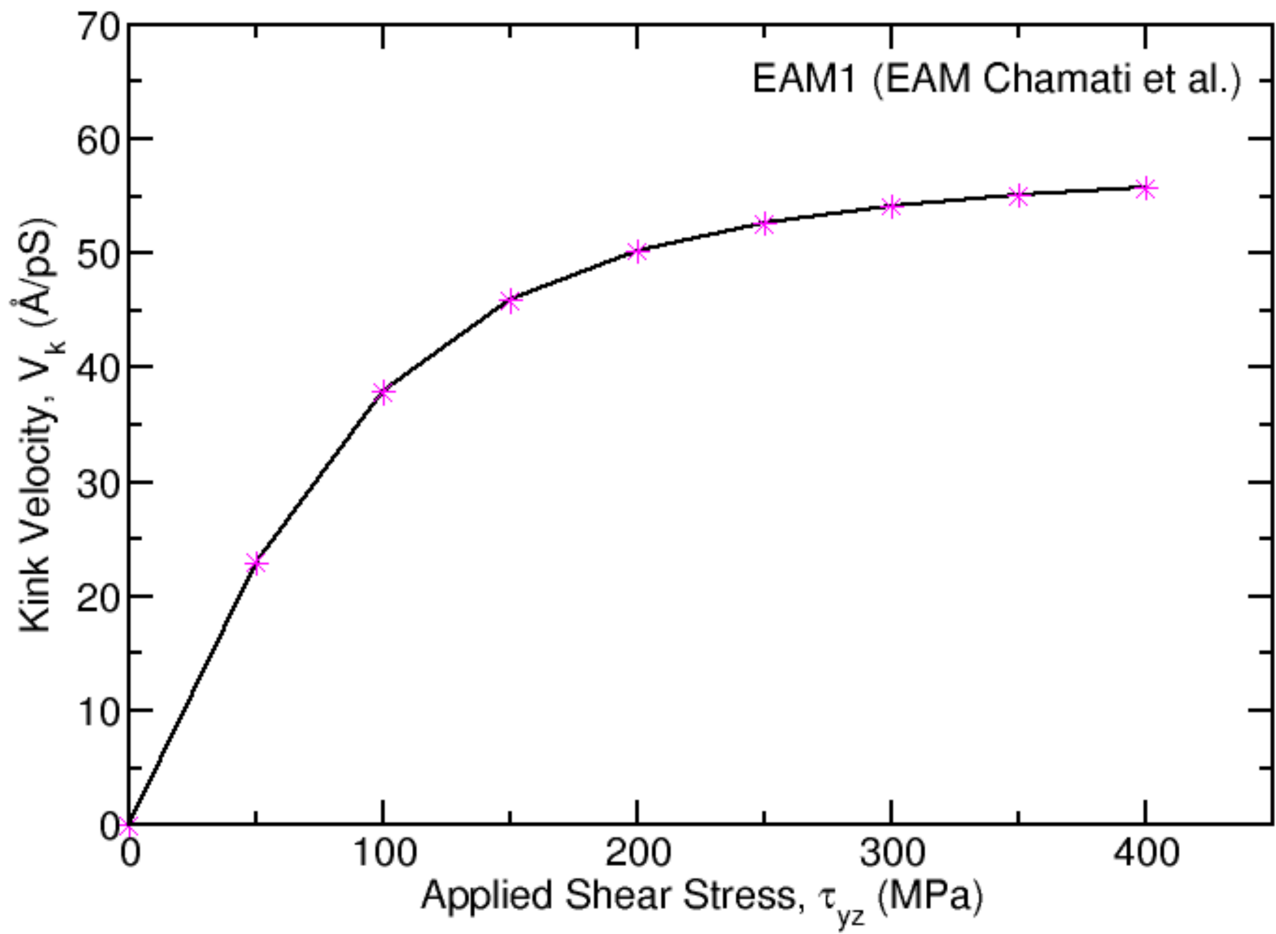


Figure 3.6: Asymptotic Kink velocity plotted as a function of increasing applied shear stress for EAM1 [107]. (EAM Chamati et al.)

being simulated. Discreteness effects had previously been theoretically examined in covalent materials by Boós and Duesbery [143], but this was the first attempt ever to investigate the dynamic behaviour they predict. In the simulation results, kinks were identifiable quite clearly and a kink diffusion constant could be derived from statistical analysis. It was observed that for screw dislocations, the kink diffusivity varied linearly with temperature meaning that the migration barrier is extremely small. This wide range of diffusive behavior was rationalized by analytical study which led to the conclusion that frictional forces on a kink, hence the kink velocity is independent of temperature. Many substrate potentials were tested but only a sinusoidal substrate potential function was consistent with the approximation of taking a dislocation line to be a string of constant internal structure restricted to the slip plane. The model was able to reproduce the thermally activated dynamics of dislocations seen in atomistic scale MD simulations (coupled to a thermostat) at around  $10^{-7}$  of the computational cost by simulating a line of only 500 nodes on a coarse time step of 10 ps instead of the entire atomistic system of 700,000 atoms on a very fine time step of 1 fs. This efficiency was employed to investigate dislocation motion under experimental stress levels inaccessible to MD. A clear length dependence was observed for screw dislocations that could be attributed to the negligible kink migration barrier seen earlier.

In Fig. 3.5, we have plotted the velocities of kinks as a function of evolving time for three different temperature regimes  $T = (0+\epsilon)$  K,  $T = 5$  K and  $T = 10$  K for the three EAM potentials EAM1, EAM2 and EAM3 respectively. The velocities are derived from our simulation results, from the change in position of the kinks as they propagate along the dislocation line with evolving time. It is seen that for all the cases, the kink velocities finally attain an asymptotic value. The asymptotic velocities of kinks obtained in our simulations are fitted to the asymptotic velocities predicted by the widely accepted Soliton's law [146]. These adjustments allow us to compute kink velocities and temperatures without repeating our simulations every time, for each case.

The Soliton's law has been described in details in the following text. The expression for kink velocity in Solitons law [146] is derived from the Frenkel-Kontorova model as the one used by Swinburne *et al* [145]. It has been dubbed as 'line tension model' in ref. [84] in reference to

the seminal work from Dorn, Rajnak and Guyot [147, 148] done way back in the 1960s. The line tension [84] refers to the restoring force associated with the increase in dislocation length when the dislocation bows out to form a kink pair. In the model used in [84], the dislocation line tension is first calculated by performing atomic scale simulations in a cell that is small enough to be accessible to DFT calculations. The calculated line tension value is then used as a parameter in a line tension model to predict the kink-pair formation enthalpy on screw dislocations as a function of applied stress.

The expression for the velocity is derived by starting from the Lagrangian for the line tension model for dislocations :

$$L_{LT}(x, \tau_{yz}) = \int dy \left[ \frac{\rho}{2} \left( \frac{\partial x}{\partial t} \right)^2 - (V_P(x(y, t)) - \tau_{yz} b x(y, t) + \frac{T}{2} \left( \frac{\partial x}{\partial y} \right)^2 \right], \quad (3.8)$$

where  $y$  is the position of the segment along the dislocation line and  $x$  is the displacement along the glide direction for the line segment situated at  $y$  position along glide direction at time  $t$ .  $V_P$  and  $T$  are the substrate potential and line tension coefficient respectively, both having dimensions of energy per unit length.  $\tau_{yz} b$  is the Peach-Koehler force and  $\rho$  is the dislocation mass per unit length. Extremalizing the action for the Lagrangian in Eq. 1.9 leads to the dynamical equation :

$$\rho x_{tt} = -V'_P(x(y)) + \tau_{yz} b + T x_{yy}. \quad (3.9)$$

In order to account for the energy dissipation through crystal vibrations we add a term proportional to  $x_t$  the velocity :

$$\rho x_{tt} = -V'_P(x) + \tau_{yz} b + T x_{yy} - \rho \lambda x_t. \quad (3.10)$$

A simple form for  $V_P$ ,  $V_P = \frac{\alpha x^2 (a-x)^2}{a^4}$  is considered in order to derive an analytic expression for kink velocity. For this form of the potential and in the absence of external applied stress, ( $\tau_{yz}$

= 0) , the static solution of Eq. 3.10, has the simple form:  $y = \frac{a}{2} (1 + \tanh(k_0 y))$ , where  $k_0 = \sqrt{\frac{\alpha}{2T a^2}}$

The dynamical solution in the absence of damping is given as a soliton solution [9] :

$$x = \frac{a}{4} \left( 1 + \tanh\left(\frac{k_0}{\sqrt{1 - \frac{v^2}{c^2}}}(y - vt)\right) \right), \quad (3.11)$$

where  $v$  is the velocity of the kink solution and  $c = \sqrt{\frac{T}{\rho}}$  is the velocity of small amplitude waves along the line.

It has been numerically verified that the applied stress and damping have no effect on the main form of the dynamical solution and hence we use the same equation to treat our case.

We then estimate the work done per unit time from the applied stress along the trajectory of one kink :  $W = \tau_{yz} b \int_{-\infty}^{\infty} x_t dy$ , which gives  $W = \tau_{yz} b a v$

Next we determine the expression for the heat per unit time dissipated through the damping term :  $Q = \rho \lambda \int_{-\infty}^{\infty} x_t^2 dy$  which is simplified as :  $Q = \rho \lambda a^2 v^2 \frac{k_0}{3} \sqrt{1 - \frac{v^2}{c^2}}$

In the stationary regime of the kink propagation,  $W$  and  $Q$  are equal which leads to the following deduction of the expression for kink velocity :

$$v_k = \frac{\frac{3\tau_{yz} b}{\lambda \rho} \sqrt{\frac{2T}{\alpha}}}{\sqrt{1 + \left(\frac{3\tau_{yz} b}{\lambda \rho c} \sqrt{\frac{2T}{\alpha}}\right)^2}} \quad (3.12)$$

The value of  $T$  is taken from the calculated values in [84]. Then we substitute the constant part of the equation derivable by using proper values and units as,  $\zeta = \frac{3b}{\lambda \rho} \sqrt{\frac{2T}{\alpha}}$ , and re-write the final equation as :

$$v_k = \frac{\zeta \tau_{yz}}{\sqrt{1 + \left(\frac{\zeta \tau_{yz}}{c}\right)^2}} \quad (3.13)$$

The parameters  $c$  and  $\zeta$  were adjusted for the cases of each of the two EAM potentials [107, 98] in order to reproduce the MD data ( at  $T = (0+\epsilon)$  K ) plotted in Fig. 3.5. The values obtained for EAM1 [107] are  $\zeta = 0.5 \text{ \AA ps}^{-1} \text{ MPa}^{-1}$  and  $c = 5800 \text{ ms}^{-1}$ .

In Fig. 3.5 (a), we have plotted the kink velocity profiles for EAM1 [107] at an applied shear stress,  $\tau_{yz} = 300 \text{ MPa}$ . It is seen that the velocity profiles are similar for all three temperature regimes. The asymptotic velocity is fairly constant, around 50-52  $\text{\AA}/\text{ps}$  for the different temperatures in the simulations. This figure leads us to conclude that for EAM1 [107], temperature does not have any effect on the velocity of kink propagation. This is in accordance with the prediction by Swinburne [145] which had also been seen in a few other investigations of dislocations [149-151]. In Fig. 3.5 (b), we have plotted the kink velocity profiles for EAM2 [99] at an applied shear stress,  $\tau_{yz} = 500 \text{ MPa}$ . Even here, it can be seen that the velocity profiles for all the cases of temperature are almost exactly similar. The asymptotic velocity in this case is also around 50-52  $\text{\AA}/\text{ps}$ , as in the case with EAM1. Here too, we can conclude that there is no effect of temperature on the velocity of kink propagation. Finally in Fig. 3.5 (C), we have plotted the kink velocity profiles for EAM3 [98] at an applied shear stress,  $\tau_{yz} = 800 \text{ MPa}$ . Here too the velocity profiles for all the cases of temperature are more or less same indicating yet again that the application of temperature has no effect on the velocity of kink propagation. However, unlike for the case of EAM1 and EAM2, the asymptotic velocity in this case is around 35  $\text{\AA}/\text{ps}$ , which is much lower than the previously observed value of 50-52  $\text{\AA}/\text{ps}$  observed for EAM1 and EAM2. Such differences can be attributed to the fact that each EAM inter-atomic potential is constructed based on a number of assumptions and fitting of parameters with previous experimental or DFT data for a specific species or compound and for a specific range of properties, usually at 0 K. The various effects like that of temperature range, composition and structure and also the applied fitting model are the major factors that could have led to the discrepancies observed with the different EAM potentials.

Thus, from our simulations we can conclude that the prediction of the Swinburne theory about kink velocities is correct and hence we can state that temperature has no effect on the velocity of kinks. In the next section we have reported the results obtained at higher stress levels using the same three EAM potentials, not far off from the Peierls stresses predicted for each.

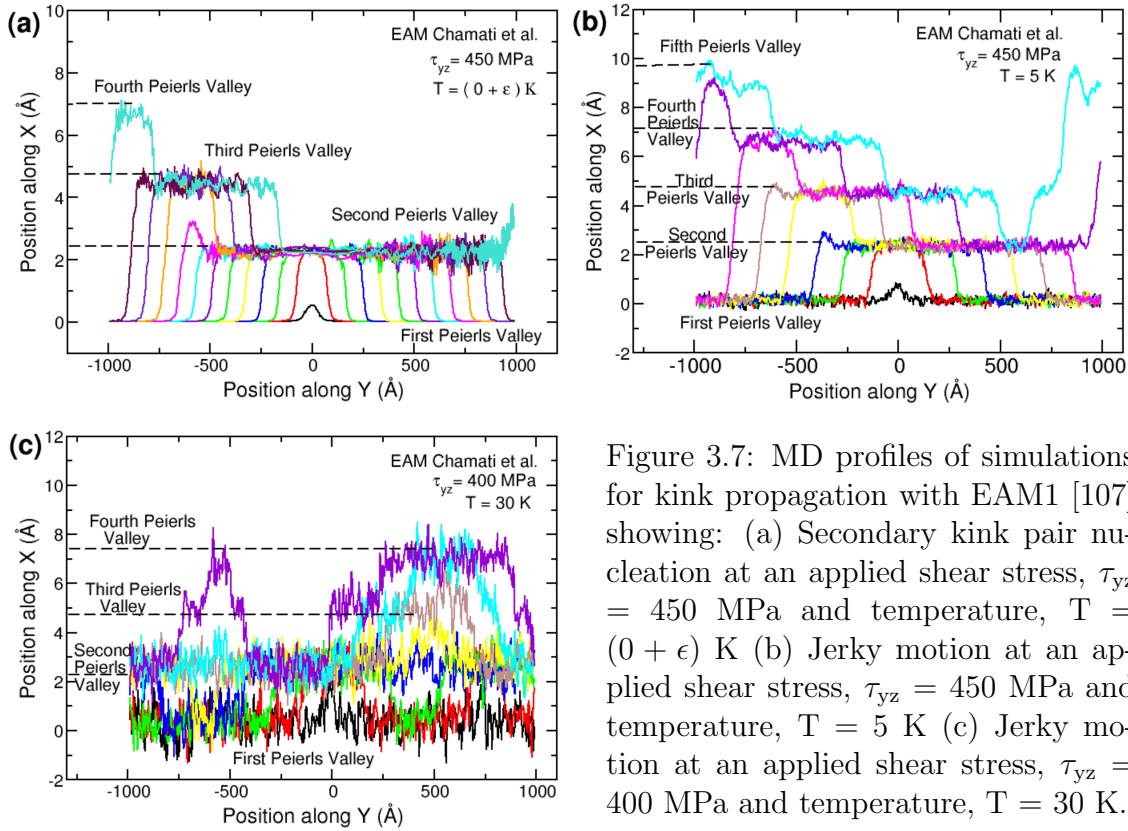


Figure 3.7: MD profiles of simulations for kink propagation with EAM1 [107] showing: (a) Secondary kink pair nucleation at an applied shear stress,  $\tau_{yz} = 450$  MPa and temperature,  $T = (0 + \epsilon)$  K (b) Jerky motion at an applied shear stress,  $\tau_{yz} = 450$  MPa and temperature,  $T = 5$  K (c) Jerky motion at an applied shear stress,  $\tau_{yz} = 400$  MPa and temperature,  $T = 30$  K.

### 3.2 Kink propagation at high stress level

We proceeded with performing simulations at higher stress levels and also tested the effects of temperature in this regime. At stresses high enough, above a certain threshold we saw that along the propagation of primary kinks, nucleation of additional kink pairs takes place. The accumulation of these additional kinks leads to the formation a macro-kink which extends from the first Peierls valley to another one, far beyond the closest Peierls valley. This phenomenon was observed with all three EAM potentials EAM1 [107], EAM2 [99] and EAM3 [98] and at different combinations of applied shear stress and temperature. It is an interesting observation which seems like the 'jerky motion' observed in Caillard's experiments.

In Fig. 3.7, we have shown the different cases of appearance of jerky motion with EAM1 [107] (Chamati et al.) As mentioned earlier, the Peierls stress of EAM1 as attained with atomistic simulations is 600 MPa. The jerky motion appeared every time at stress levels much below the Peierls stress level. Fig. 3.7 (a) shows the MD profiles of the dislocation at an applied shear

stress,  $\tau_{yz} = 450$  MPa and temperature  $T = (0 + \epsilon)$  K. It is seen that after the initial kink pair nucleates in the first Peierls valley and propagates along the simulation cell, at some point the atoms in the left kink jump to the next Peierls valley with respect to the initial and a secondary kink pair is now nucleated here. Further kink nucleation takes place along the dislocation line. In order to see the effect of temperature on such phenomena we repeated our simulations at the same stress level but with an applied temperature of 5 K. It was observed that for the same number of MD time steps, the secondary kinks reach the fifth Peierls valley as compared to the fourth Peierls valley in the previous case. This has been plotted in Fig. 3.7 (b). This would suggest that temperature aids this secondary nucleation process. In order to further verify this, we performed the simulations again at a lower stress level of 400 MPa while gradually increasing the applied temperature in different simulations. We were able to see the similar nucleation of multiple kink pairs at an applied temperature of 30 K (Fig. 3.7 (c)), which leads us to conclude that temperature aids the process of secondary kink pair nucleation. It can also be observed that the MD profiles of the dislocation are not very smooth for this particularly case. It may be attributed to the fact that temperature increases the atomic vibrations of the individual atoms constituting the dislocation.

Next In Fig. 3.8, we have shown the different cases of appearance of jerky motion with EAM2 [99]. Fig. 3.8 (a) shows the MD profiles of the dislocation at an applied shear stress,  $\tau_{yz} = 600$  MPa and temperature  $T = (0 + \epsilon)$  K. It is seen that the initial kink pair (starting configuration taken from NEB computations) instantly grows in size reaching the second Peierls valley. After that the kink pair just keeps growing further in size and jumping to other Peierls valleys centred around the same position i.e. the center of the simulation cell. Finally the kink pair grows into a very large macro-kink extending several Peierls valleys with the rest of the dislocation still in the initial Peierls valley. The same exact trend is seen in Fig. 3.8 (b). Here the instantaneous formation of the macro-kink is observed at a lower applied shear stress level,  $\tau_{yz} = 550$  MPa but with applied temperature  $T = 5$  K. Similar instantaneous nucleation is seen again for even lower applied shear stress,  $\tau_{yz} = 500$  MPa but with higher applied temperature  $T = 20$  K, as evident from Fig. 3.8 (c). However it seems that the source of energy that causes such instantaneous nucleations is the inertial energy in the initial kinked dislocation profile taken

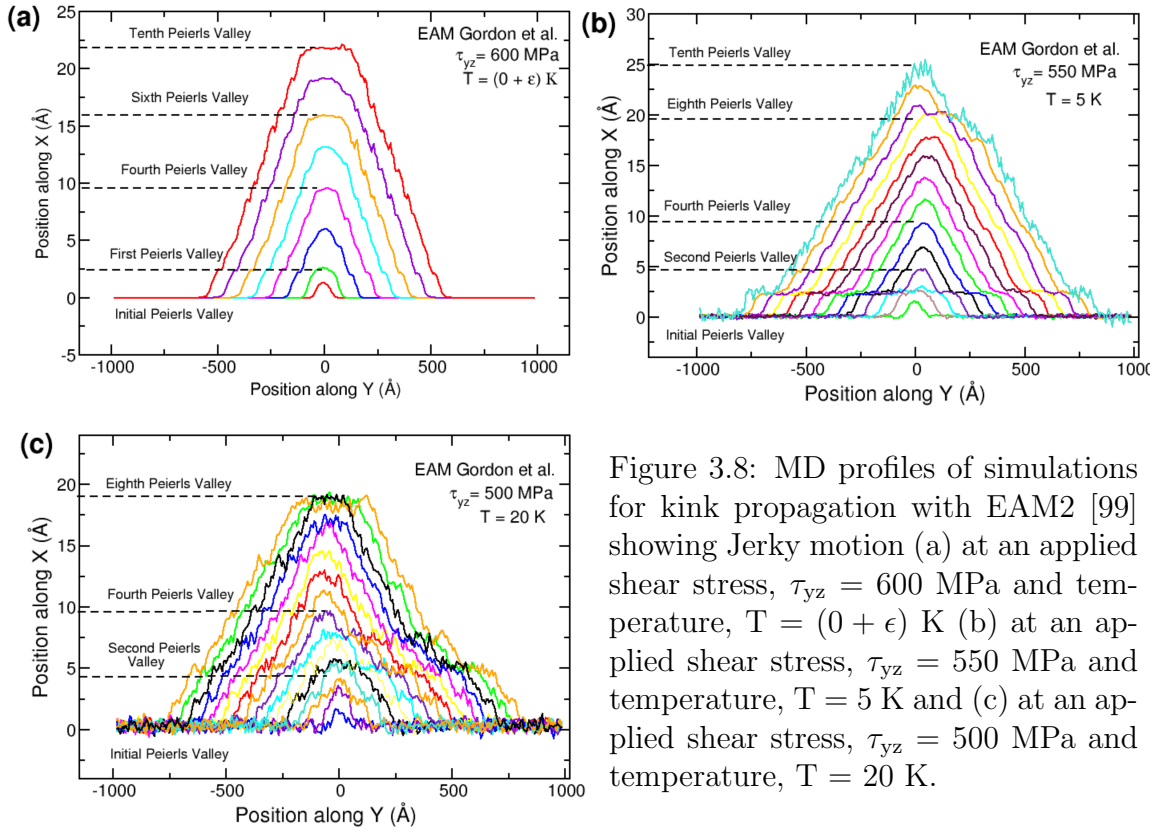


Figure 3.8: MD profiles of simulations for kink propagation with EAM2 [99] showing Jerky motion (a) at an applied shear stress,  $\tau_{yz} = 600$  MPa and temperature,  $T = (0 + \epsilon)$  K (b) at an applied shear stress,  $\tau_{yz} = 550$  MPa and temperature,  $T = 5$  K and (c) at an applied shear stress,  $\tau_{yz} = 500$  MPa and temperature,  $T = 20$  K.

from the NEB computations.

In order to mitigate this inertial effect, we proceeded to perform relaxation of the isolated kinked profile from NEB in a simulation cell. This ensures the gradual size growth of the kink pair after successive MD steps and after a while it reaches the next Peierls valley and the kinks then begin to propagate along the dislocation line as per standard theory. We utilize the first kinked profile that is seen to be fully formed in the adjacent Peierls valley and then repeat our computations using EAM2 [99]. The results have been reported in Fig. 3.9.

In Fig. 3.9 (a), we can see that the starting profile is that of a kink pair fully nucleated in the next Peierls valley. Here we see that with the same parameters ( $\tau_{yz} = 600$  MPa and  $T = (0 + \epsilon)$  K) as used in Fig. 3.8 (a), the results are not the same. Instead of an instantaneous macro-kink, we observe the occurrence of the standard Peierls process. This is due to the initial relaxation of the starting dislocation profile. So we proceeded to perform more simulations at a higher applied stress level. In Fig. 3.9 (b), there is reappearance of the Jerky motion of kinks. The parameters used for this set of simulations are  $\tau_{yz} = 650$  MPa and  $T = (0 + \epsilon)$  K and the jerky

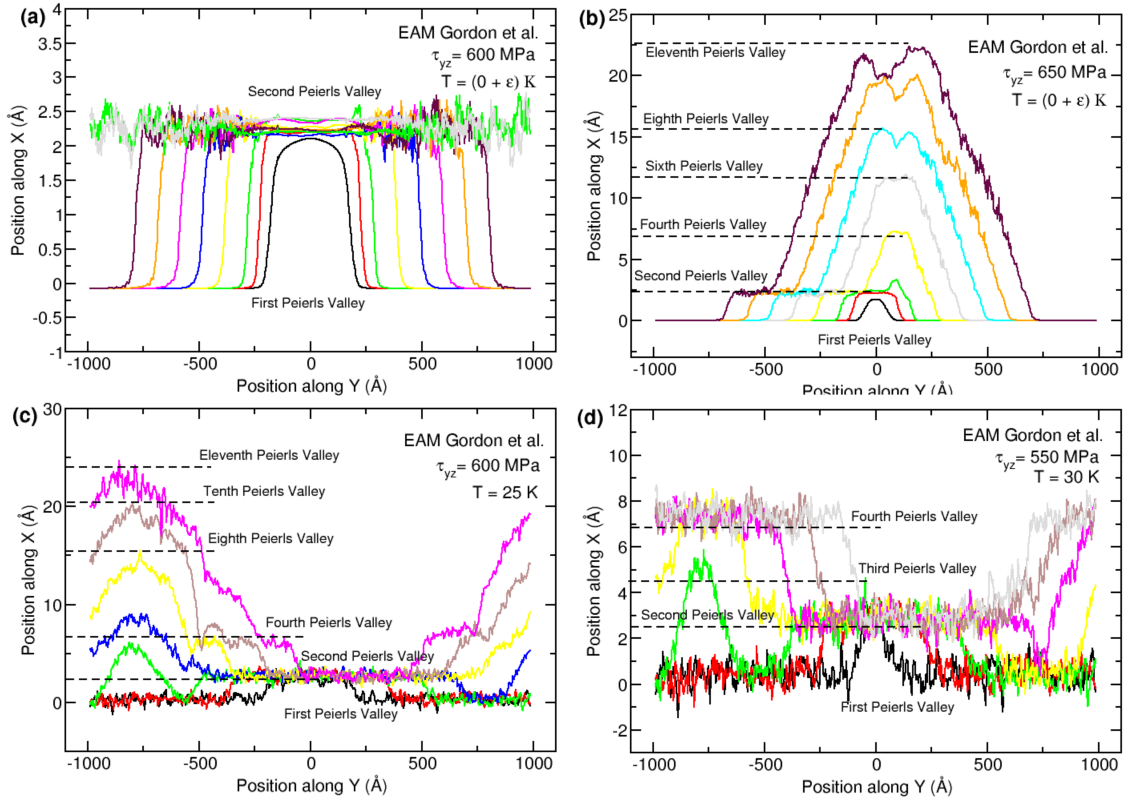


Figure 3.9: MD profiles of simulations for kink propagation with EAM2 [99] after proper relaxation of the starting unstable profile taken from NEB computations showing: (a) Standard Peierls [9] process at an applied shear stress,  $\tau_{yz} = 600$  MPa and  $T = (0 + \epsilon)$  K (previously Jerky motion was observed instead with these same parameters) (b) Jerky motion at an applied shear stress,  $\tau_{yz} = 650$  MPa (instead of 600 MPa as previously seen) and temperature,  $T = (0 + \epsilon)$  K (c) Jerky motion at an applied shear stress,  $\tau_{yz} = 600$  MPa and temperature,  $T = 30$  K and (d) Jerky motion at an applied shear stress,  $\tau_{yz} = 550$  MPa and temperature,  $T = 30$  K.

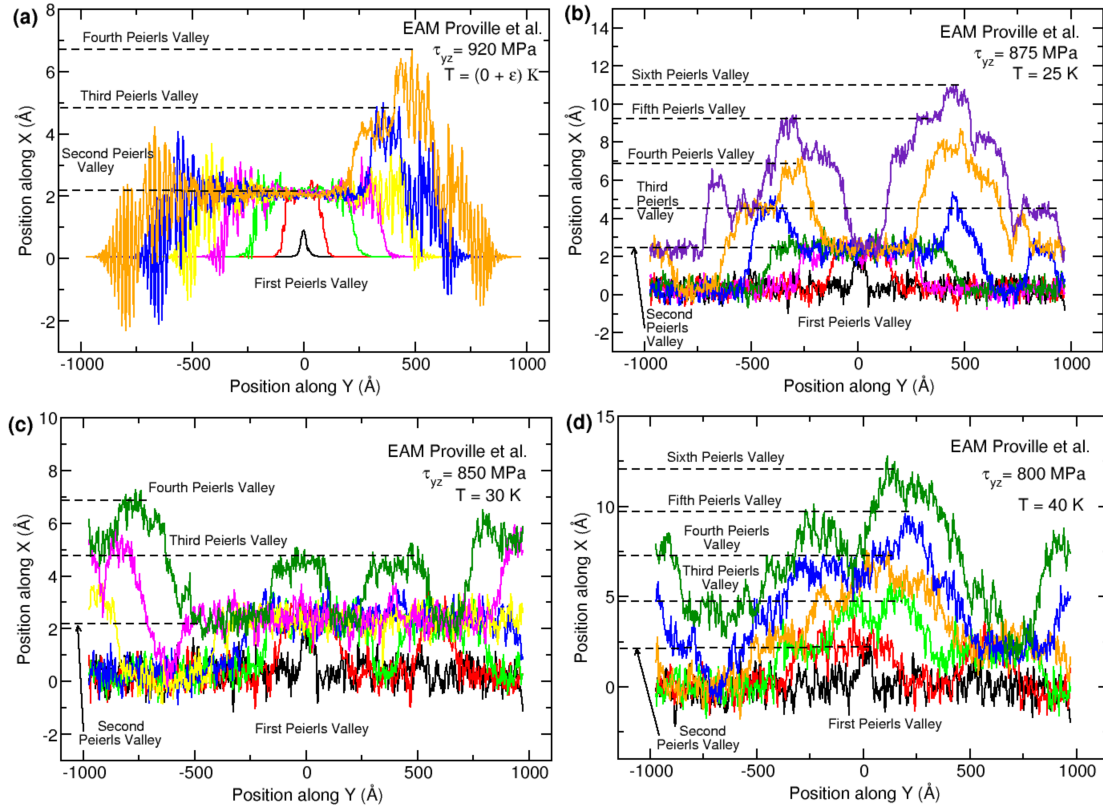


Figure 3.10: MD profiles of simulations for kink propagation with EAM3 [98] showing Jerky motion (a) at an applied shear stress  $\tau_{yz} = 920$  MPa and temperature  $T = (0 + \epsilon)$  K; b) at an applied shear stress  $\tau_{yz} = 875$  MPa and temperature  $T = 25$  K; c) at an applied shear stress  $\tau_{yz} = 850$  MPa and temperature  $T = 30$  K and (d) at an applied shear stress  $\tau_{yz} = 800$  MPa and temperature  $T = 40$  K

motion no longer constitutes an instantaneous macro kink formation. Proceeding further, we introduced temperature in our simulations and in accordance with previous trends, the Jerky motion was observed at lower stress levels as the temperature was gradually increased. In Fig. 3.9 (c), the Jerky motion was observed at an applied shear stress,  $\tau_{yz} = 600$  MPa and temperature,  $T = 25$  K whereas in Fig. 3.9 (d), the same was observed at further lower applied shear stress level,  $\tau_{yz} = 550$  MPa but slightly higher temperature,  $T = 30$  K.

However we must emphasize that EAM2 has negative coefficient of thermal expansion, which may result in the unphysical behaviour during kink propagation. We may argue that the thermal energy dissipation around the propagating kink could yield spurious contractions of the crystal region situated around the kinks.

The results of the simulations performed with the last EAM that we have studied i.e. EAM3

[98] have been plotted in Fig. 3.10. In Fig. 3.10 (a), we see the appearance of the Jerky motion with parameters applied shear stress  $\tau_{yz} = 920$  MPa and temperature  $T = (0 + \epsilon)$  K. Continuing with the trend of introducing temperature and trying at lower stress levels, we were able to see the Jerky motion again with the parameters  $\tau_{yz} = 875$  MPa and temperature,  $T = 25$  K, plotted in Fig. 3.10 (b). The Jerky motion occurred again at further lower stress level  $\tau_{yz} = 850$  MPa and slightly higher temperature,  $T = 30$  K. This is shown in Fig. 3.10 (c). We were able to observe the Jerky motion again with much lower applied shear stress level  $\tau_{yz} = 800$  MPa and a slightly higher temperature,  $T = 40$  K. This has been plotted in Fig. 3.10 (d).

There are a few common trends observed with all the three EAMs. We have seen that the jerky motion has occurred at stress values well below the Peierls stress levels attributed to each EAM. With the application of temperature, the jerky motion has been observed at further lower applied shear stress levels. The associated energetics causing the occurrence of such phenomenon have been analyzed and described in details in the following section.

### 3.3 Investigation of the energetics responsible for jerky motion

For our simulations with EAM1 [107] at  $T = (0 + \epsilon)$  K, although we observed a jerky motion of the screw dislocation at  $\tau_{yz} = 450$  MPa, we wanted to investigate what happens if the applied shear stress is increased further. We performed another set of simulations at  $\tau_{yz} = 550$  MPa and as expected there was the appearance of a macro-kink once again. On closer observation of the time integrated MD profiles, we found some differences which we have reported in Fig. 3.11. Comparing the profiles in Fig. 3.11 (a) and Fig. 3.11 (b), we observe that in the first figure, for  $\tau_{yz} = 450$  MPa, the nucleation of the secondary kink-pair occurs after the primary kink has travelled a distance of  $600 \text{ \AA}$  from the starting position whereas for the second case at  $\tau_{yz} = 550$  MPa, the secondary kink-pair occurs after the primary kink has travelled a much smaller distance of  $250 \text{ \AA}$ . This leads to the inference that the time period for occurrence of jerky motion decreases with increasing applied shear stress levels. This also means that some

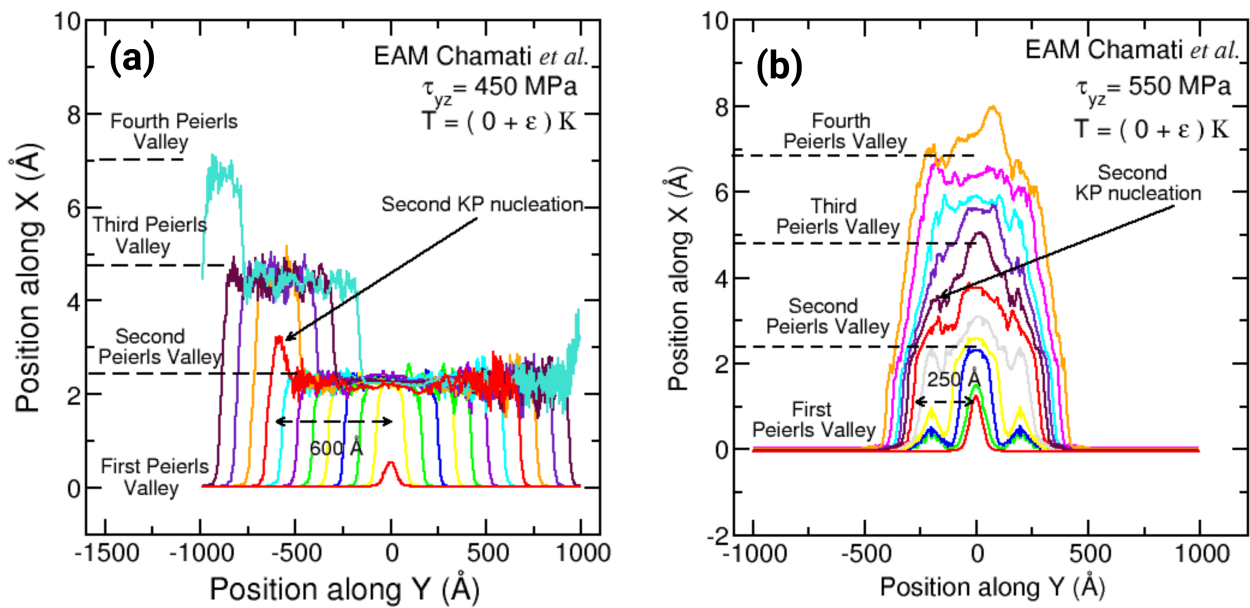


Figure 3.11: MD profiles of simulations for kink propagation with EAM1 [107] showing Jerky motion at temperature  $T = (0 + \epsilon)$  K ;(a) at an applied shear stress  $\tau_{yz} = 450$  MPa and (b) at an applied shear stress  $\tau_{yz} = 550$  MPa. The initial state of MD is represented by the kinked profile in red, computed by the NEB method. Dashed arrows indicate the distance between the primary kink pair and the second kink pair nucleation. The black arrows are used to point out the instant of occurrence of secondary kink pairs.

type of energy gets accumulated in the screw dislocation because of which nucleation of more kink pairs occurs.

From the previously performed NEB computations, we got an idea of the variation of the kink pair formation enthalpy with varying applied shear stress. In Fig. 3.12 we have plotted some results from NEB computations carried out with EAM1 [107]. In Fig. 3.12 (a), we have plotted a view of all 50 NEB images as they travel along a MEP from the initial state of the screw dislocation to the final state. The top of the hill refers to the saddle state where the kink pair nucleates. The corresponding energy along the Y axis is the measure of the kink pair formation enthalpy at a particular stress level for the screw dislocation. In Fig. 3.12 (b), we have shown the profiles of the MEP at some regular intervals of applied shear stress. A zoomed in version of the same has been plotted in Fig. 3.12 (c) and the kink-pair formation enthalpies along with the corresponding applied shear stress levels have been pointed out. In the last figure, Fig. 3.12 (d), these kink-pair formation enthalpies have been plotted as a function of the applied shear stress over its entire working range in our simulations. It can be observed that the kink pair formation enthalpy gradually decreases as the applied shear stress value increases.

Next in order to compute the energy built up in the screw dislocation responsible for formation of secondary kinks, we divided the entire length of the screw dislocation into segments, each of length  $b$ . Following this we computed the combined kinetic energies of all the atoms associated with a kink located at  $b$  along the dislocation line for different values of the applied shear stress. We then plotted the same as a function of the increasing applied shear stress for EAM1 [107]. This has been plotted in Fig. 3.13. We can see that the kinetic energy increases gradually with the applied shear stress. On the same figure, we plot again the enthalpy of kink pair formation for EAM1 [107] at different levels of applied shear stress. By linearly expanding the curve for kinetic energy, we observed that this curve intersects the plot of kink pair formation enthalpy at a point and the corresponding shear stress level is very close to the shear stress at which the jerky motion was observed. So we can conclude that at this applied shear stress level, the kinetic energy accumulated because of the travelling kinks becomes sufficient for the nucleation of new kink pairs, which ultimately leads to the formation of a macro-kink comprising of multiple kink pairs and extending over several Peierls valleys [9].

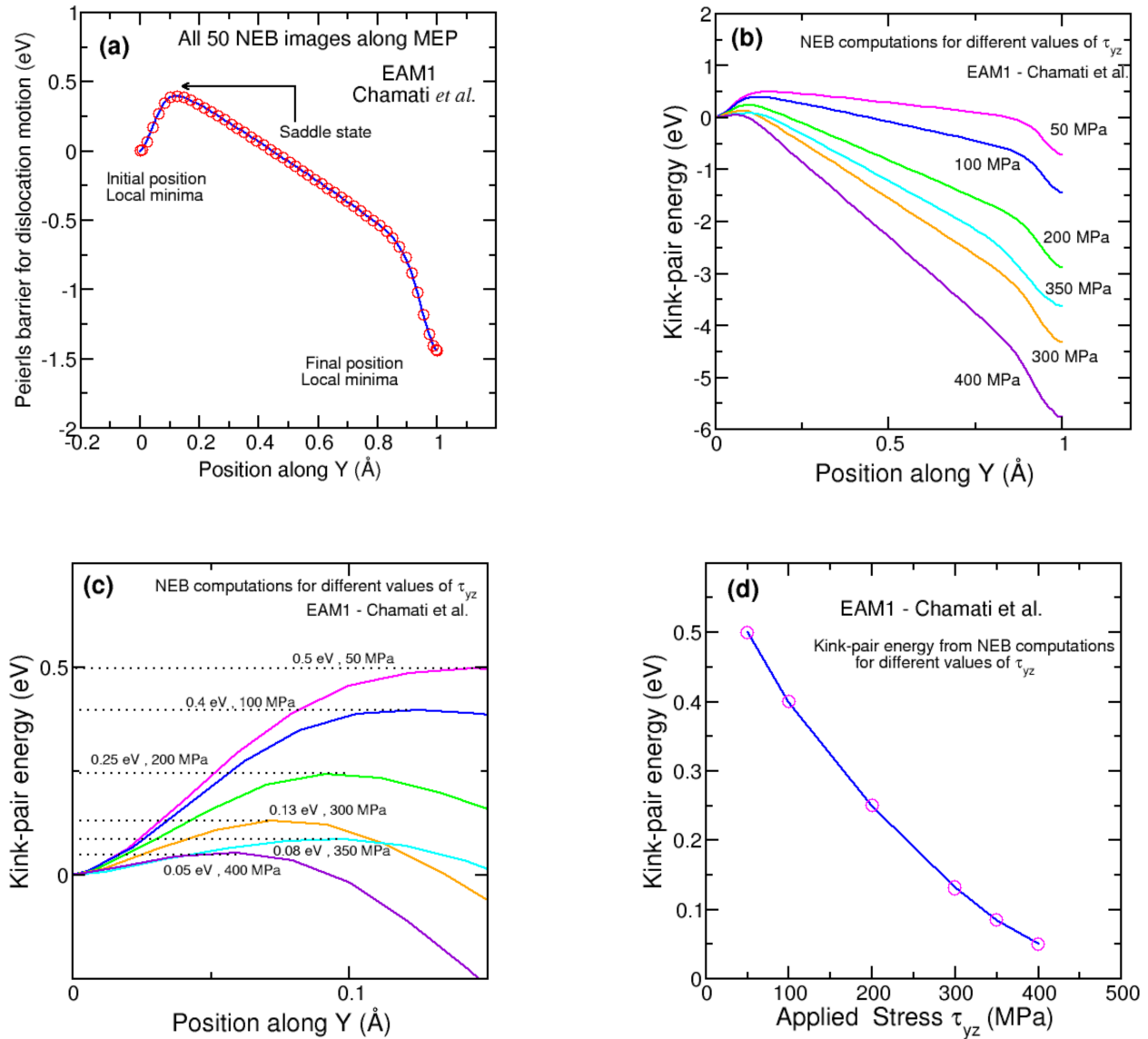


Figure 3.12: Results from NEB computations at different levels of applied shear stresses using EAM1 [107] showing: (a) The MEP undertaken by the 50 NEB images between the initial and the final straight screw dislocation states (b) Different MEPs of the NEB images at different levels of applied shear stress,  $\tau_{yz}$  (c) zoomed in view of (b) showing also the corresponding values of kink-pair formation energies for different values of the applied shear stress,  $\tau_{yz}$  (d) Variation of the kink pair formation energy over the entire range of the applied shear stress for our simulations

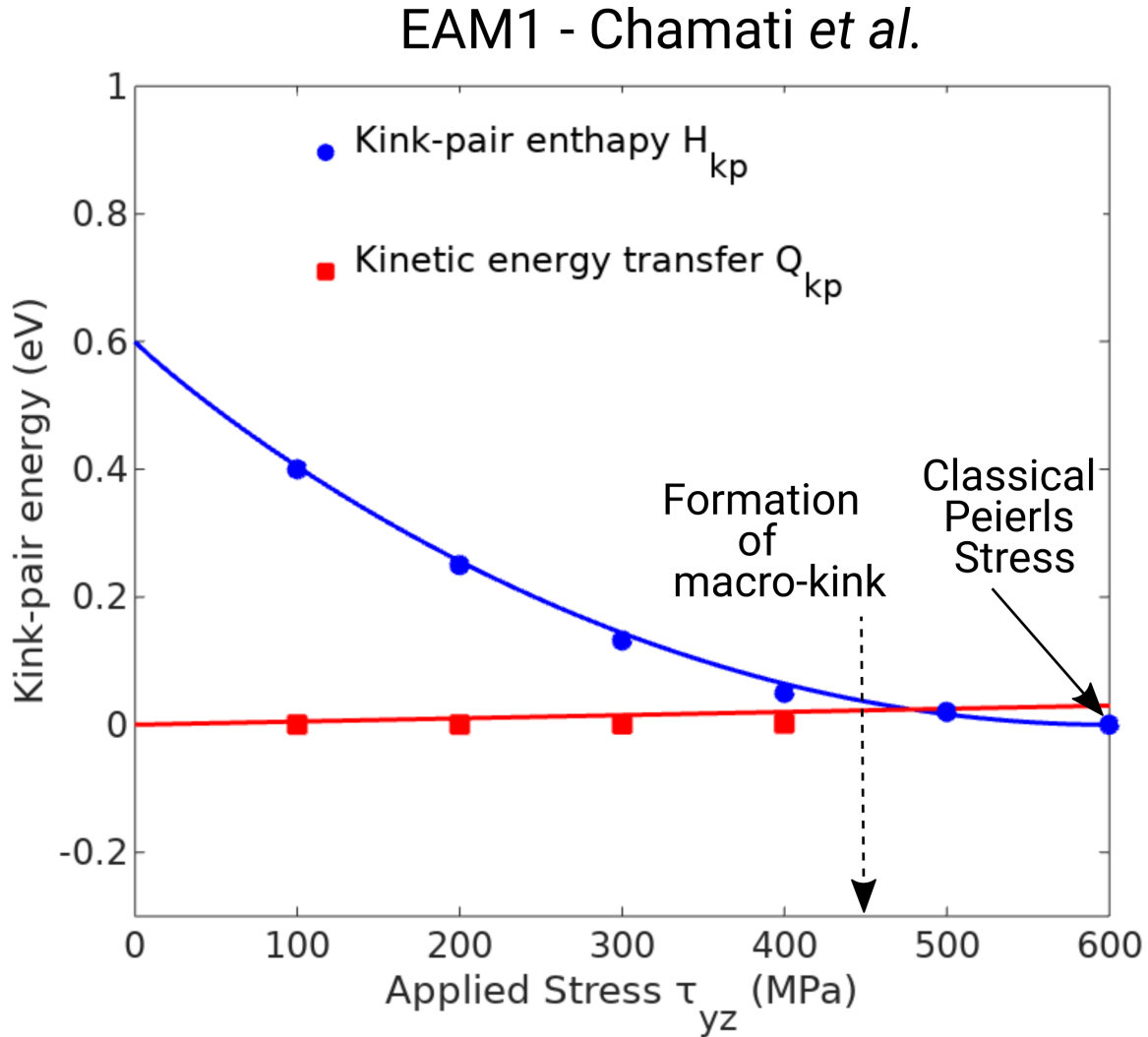


Figure 3.13: Kinetic energy transfer from kink motion and kink pair activation enthalpy against the applied shear stress  $\tau_{yz}$ . The symbols represent values from atomistic simulations and the curves are according to analytical fits. Blue line : activation enthalpy for the nucleation of a kink pair  $H_{kp}$  ; Red line : steady value of the kinetic energy transfer  $Q_{kp}$ . The analytical fit for the kink pair formation enthalpy is :  $H_{kp} = H_0[1 - (\frac{\tau_{yz}}{\tau_P})^{0.95}]^{1.96}$  and that for the kinetic energy along the dislocation segments is :  $Q_{kp} = 0.03 \frac{\tau_{yz}}{\tau_P}$ .

# Chapter 4

## Atomistic scale study of the screw dislocation glide in bcc Tungsten

### 4.1 Introduction

Tungsten has a bcc crystal structure and is one of the most important metals of the present day, owing to excellent properties that make it useful for a wide variety of applications. It has the highest melting point amongst all the metals, around 3100 °K and the lowest coefficient of thermal expansion. The melting point of tungsten is 5400 °C and it is also one of the heaviest metals having a density of around 19.2 g/cm<sup>3</sup>. Tungsten in its pure form appears as a shiny white metal and can be yielded and processed easily. The presence of little amounts of carbon and oxygen gives it significant hardness and brittleness. The most common use of tungsten is in the form of cemented carbides (WC) or hardmetals. Tungsten monocarbide (WC) has hardness comparable to that of diamond and by combining it with the toughness and plasticity of metallic alloy binders like Co, Ni or Fe, a variety of product tools are manufactured like cutting and mining tools, tools for shaping, moulding and surface finish of metals and their alloys like drill bits, high speed cutting tools, lathe tools and milling cutters. It is also extensively used in the shipping, mining and construction industries. Other significant properties that make tungsten popular are high modulus elasticity and compression, high resistance to thermal creep,

high conductivity of electricity and heat. The first industrial use of tungsten was in the of steels towards the end of the 19th century finally leading to the development of high speed steels. Later on the development of tungsten powder metallurgy led to the development of the lamp industry. Products like magnetrons for microwave ovens, filaments of lights, contacts, wires and rods are all milled from tungsten and used extensively throughout the world. Another aspect of the use of tungsten is in the field of nuclear power. It is a good candidate for the claddings of nuclear fuel rods in advanced fission reactors and as a plasma facing component in fusion reactors. Hence it is of utmost importance to study the evolution of the microstructure of tungsten and tungsten based alloys under irradiation which depends to a large extent on the properties of point defects like vacancies and interstitials and also other defects like dislocations. The structural properties of tungsten are quite similar to body centered cubic iron, e.g. a prominent decrease of the yield stress with the increase in temperature in the range of low temperatures and they too don't follow the Schmid law. Like iron, their plastic deformation depends on the low mobility of screw dislocations arising from a frictional force, in the planes associated with the  $\langle 111 \rangle$  direction. They too exhibit a large difference between the deformation stress extrapolated to zero K in tests and the theoretical Peierls stress obtained from DFT calculations [153]. With the experimental results of D. Caillard and our own simulation results for bcc Fe, where we saw the occurrence of jerky motion instead of the standard Peierls mechanism at low temperatures, we proceeded to investigate if such phenomenon pertains only to Fe or other bcc metals also. We performed atomistic scale MD simulations for tungsten using the interatomic potential, EAM4 [154] developed by Marinica *et al.* specifically for modelling the defects and dislocations in bcc tungsten.

## 4.2 Details of the simulation cell, algorithms, and the different steps of simulations

### 4.2.1 Simulation cell

The simulation cell used is similar to the one used for Fe with just changes in the dimensions in order to facilitate the computations for tungsten. Like in the case of iron, here too the simulation cell comprises of atoms placed in symmetric Body Centred Cubic (bcc) configuration of a perfect crystal. The XY plane is again chosen as the glide plane corresponding to the horizontal plane of the cell and with Periodic Boundary Condition (PBC) along X and Y directions. Again, like in the case of iron the assigned cell directions are  $X = [112]$ ,  $Y = [111]$  and  $Z = [110]$  and the Burgers vector  $b = \frac{a_0}{2}[111]$  corresponds to the line direction (Y) of the screw dislocation. For the case of iron, the simulation cell dimensions were  $x = 14 b$ ,  $y = 160 b$  and  $z = 20 b$  respectively ( $b = 2.48 \text{ \AA}$  for  $\alpha$ -Fe). However this dimensions did not suit the simulations for tungsten owing to the fact that the lattice parameter and hence the distance between successive Pierls valleys is larger in W compared to Fe. This meant that we needed to increase the dimension along  $X = [112]$  and adjust the other dimensions so that the total number of atoms is not compromised. The dimensions compatible with our simulations were finally chosen were  $x = 22 b$ ,  $y = 104 b$  and  $z = 20 b$  respectively ( $b = 3.14 \text{ \AA}$  for W). A screw dislocation is introduced in the saw manner as for iron and an additional shift of  $b/2$  is introduced along the Y direction to stabilize the simulation cell with a single screw dislocation.

### 4.2.2 Quenching and NEB calculations

Like for the case of iron, we perform a quenching of our simulation cell loaded with an applied shear stress on two different occasions, first for the initial position and then for the final position of a straight dislocation along the glide plane. These two positions can be defined by providing the co-ordinates in the code. Quenching relaxes the simulation cell till the atomic forces gradually decrease to  $10^{-5} \text{ eV/\AA}$  and a mechanical equilibrium is reached. Then we use

these initial and final relaxed positions to compute the minimum energy path (MEP) for the screw dislocation using the Nudged ELastic Band (NEB) method at the same value of applied shear stress. The quenching process is performed for all the values of applied shear at which we want to perform the NEB computations. As in the case of iron, the value of the spring constant is chosen as  $10 \frac{N}{A}$  and the number of system replicas is fixed at 50. The NEB codes are run for applied stress values below the Peierls stress in order to ensure that the minimum energy path (MEP) is computed when the dislocation motion is hindered by a barrier.

In Fig. 4.1 (a), we have plotted the enthalpy along the minimum energy path of screw dislocations obtained from NEB calculations at regular intervals of applied shear stresses,  $\tau_{yz}$  i.e. at 100 MPa, 500 MPa, 900 MPa, 1.2 GPa and 1.5 GPa respectively. The local maximas corresponding to the kink nucleation can be seen for different stress levels. In Fig. 4.2 (b), we show a zoomed in view of Fig. 4.1 (a) wherein the kink nucleation enthalpies have been specified for each value of the applied shear stress  $\tau_{yz}$ . Lastly in Fig. 4.1 (c), the kink pair nucleation enthalpies have been plotted against the different values of the applied shear stress  $\tau_{yz}$ . It can be observed that the enthalpy of kink pair formation decreases gradually as the applied shear stress increases, indicating that the dislocation glide becomes easier at higher applied stress levels.

### 4.2.3 The extended simulation cell

The length of the simulation cell used to perform the NEB computations is much shorter for the case of tungsten as compared to that for iron. For iron we used a simulation cell with dimension  $y = 160$  b along the dislocation line whereas for tungsten, we had to contain with a much shorter length of  $y = 104$  b. However in chapter 3, we had seen that for the case of extended simulation cells there is a negligible difference between the temperature per atom when we considered extended simulation cells which are 5 and 7 times the NEB cell respectively. It is important to recall that this temperature arises from the kinked dislocation profile placed in the central cell derived from NEB computations which corresponds to a transition state i.e. one of the local enthalpy maximas. For the case of iron, it was sufficient to proceed with just 5

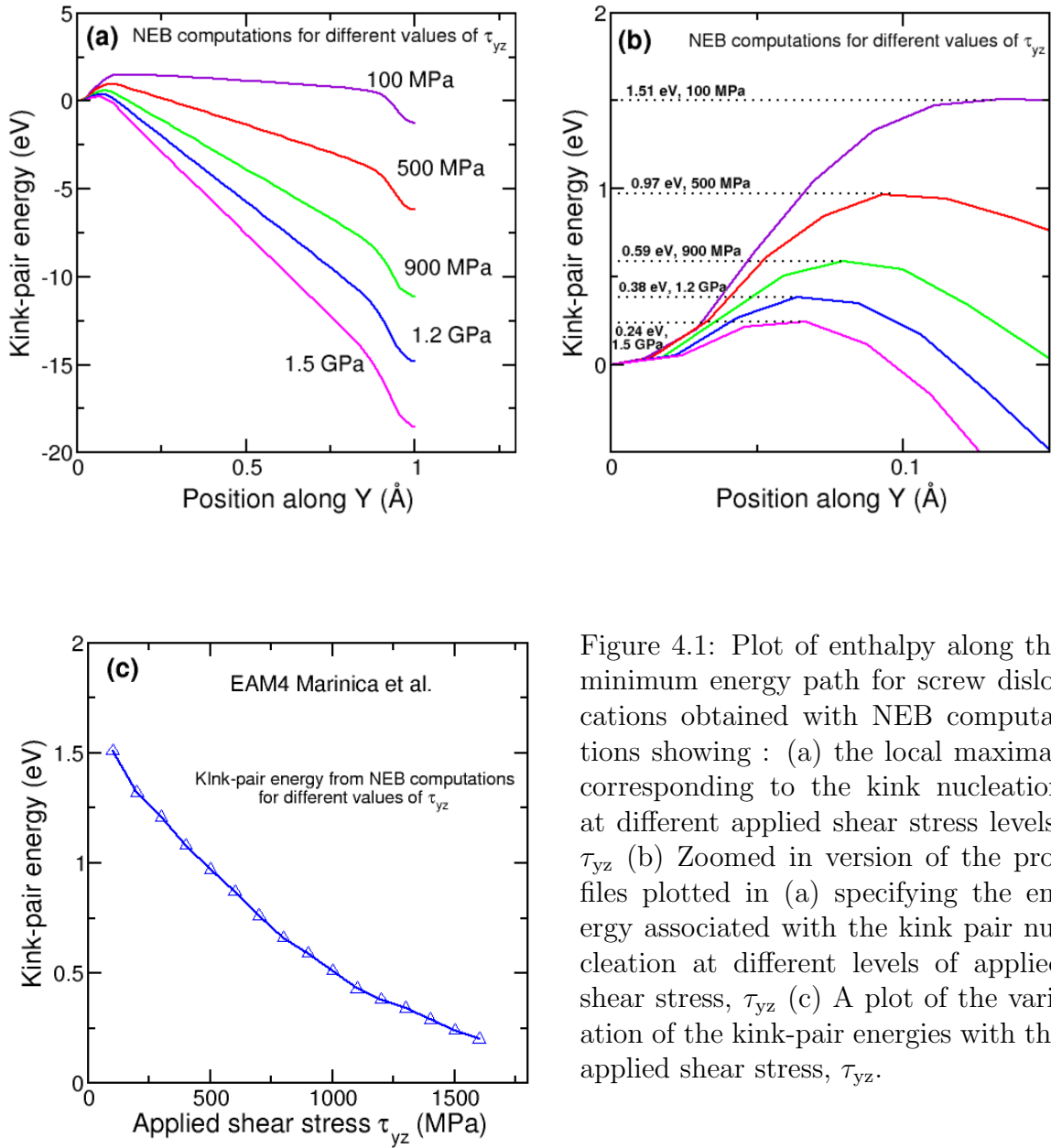


Figure 4.1: Plot of enthalpy along the minimum energy path for screw dislocations obtained with NEB computations showing : (a) the local maximas corresponding to the kink nucleation at different applied shear stress levels,  $\tau_{yz}$  (b) Zoomed in version of the profiles plotted in (a) specifying the energy associated with the kink pair nucleation at different levels of applied shear stress,  $\tau_{yz}$  (c) A plot of the variation of the kink-pair energies with the applied shear stress,  $\tau_{yz}$ .

times the extension. However, for tungsten, as the NEB cell is quite shorter, we have chosen to use an extended simulation cell which is 7 times the NEB cell in length. Thus we end up with a simulation cell having a length of 728 b ( $7 \times 104$  b) which is equivalent to 2300 Å or 0.23 μm.

After the NEB computations are done and the extended simulation cell has been created we perform molecular dynamics simulations wherein the atomic motions are integrated classically according to Newton's laws and coupled them with an EAM potentials in order to calculate the atomic energies. The EAM potential (EAM4) [154] that we have utilised has been developed by Marinica *et al.* and we have described it in details in the following subsection.

#### 4.2.4 The EAM potential used for our simulations

Unlike for BCC iron, very few EAM potentials are available in the literature compatible for modeling tungsten. The first many-body potential for tungsten was developed by Finnis and Sinclair [155]. Ackland and Thetford [156] improved upon this potential by creating a larger fitting database and including the electron gas calculations. It was used to predict bulk properties, radiation damage and energy landscapes of defects. Subsequently some other EAM potentials have been developed over the years by Juslin and Wirth [157], Wang *et al* [158], Derlet *et al* [159] etc. However these potentials had some shortcomings when it comes to serving our purpose of studying the screw dislocation glide in BCC tungsten. For example the EAM in [157] was specifically designed to study helium-vacancy clustering in tungsten, the EAM in [158] described very inaccurately the energy landscape of defects in simulations carried out at finite temperature whereas the EAM in [159] did not correctly predict the degenerate core for screw dislocations.

The potentials (we call them EAM4a-EAM4d instead of EAM1-EAM4 in the original work) developed by Marinica *et al* [154] use the embedded atom method algorithm fitted to a diverse database comprising of experimentally determined parameters for tungsten, formation energies and atomic forces based on DFT calculations. A lot configurations for point and extended defects were tested for the transferability of the potentials. All important properties related to the  $\langle 111 \rangle$  screw dislocations were computed such as the Peierls barrier, the Peierls

stress, the glide plane, the enthalpy of formation of kink pairs, the dislocation core structure and polarisation of the core. A quadrupolar periodic array of dislocation dipoles [77, 160] was considered and a study was carried out to find out the stability of the degenerate and non-degenerate core configurations. by computing the dependence of the dislocation core energy on its polarization. They concluded that a stable dislocation core is completely unpolarized. They also estimated the Peierls barrier for the  $\langle 111 \rangle$  screw dislocation by simultaneous displacement of the two dislocations along the (110) plane such that a constant separation is maintained between them at all stages. A NEB calculation was then performed and the elastic contributions of the associated strain rates of the initial and final states were subtracted. A single-humped Peierls barrier was obtained complying with DFT results with a barrier height agreeing very well with DFT calculations enabling quantitative comparison of the predicted kink-pair formation energies with experimental data.

Next, in order to determine the Peierls stress, the simulation cell was subjected to shear stress till the point when the dislocation began to glide. Two different types of simulation cells were employed : with free surfaces parallel to the (110) plane as employed by Rodney *et al* [129] and using a quadrupolar arrangement of dislocation dipoles having periodic boundary conditions in all three directions. It was seen that only EAM4c predicted a (110) glide plane as observed in experimental tests [161, 162] and DFT computations [163]. The Peierls stress predicted by this potential is around 1.1 GPa. EAM4b and EAM4d are able to predict much more precisely the Peierls barrier but the glide plane predicted by them is (211) . The EAM4c potential seems like the lone potential for tungsten that reproduces the single-humped Peierls barrier and also predicts a (110) glide plane. Overall, we can conclude that EAM4(a-d) are the first EAM potentials for tungsten that agree qualitatively with DFT computations regarding screw dislocations. These potentials are able to proffer agreeable EAM parametrizations that are adept to motion of screw dislocations in tungsten, a problem that was previously not addressed to such an acceptable extent in the methods available in the literature. For our simulations, we have chosen to work with EAM4d because the magnitude of the Peierls potential and the kink-pair energy are the closest to the experimental and DFT values. The Peierls stress associated with this EAM potential is 2.03 GPa and hence our simulations were carried out at stress levels

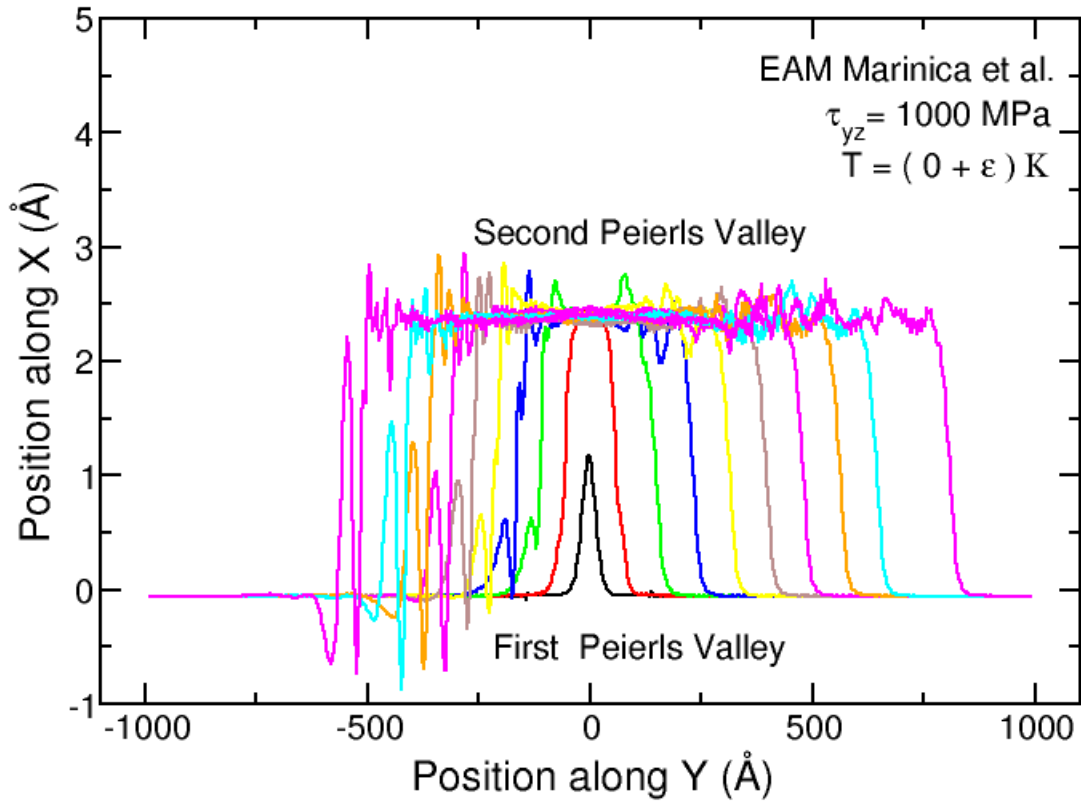


Figure 4.2: MD profiles of simulations of kink propagation for temperature close to 0 K, i.e.  $T = (0 + \epsilon)$  K for EAM4 [1] performed at an applied shear stress,  $\tau_{yz} = 1$  GPa.

lower than this value.

### 4.3 MD simulation results

Starting from a long straight dislocation with a kink pair at the center of the dislocation, the simulations were launched with combinations of different levels of applied shear stresses, different temperatures using the EAM inter atomic potential EAM4. The results have been reported and discussed in the following sub sections.

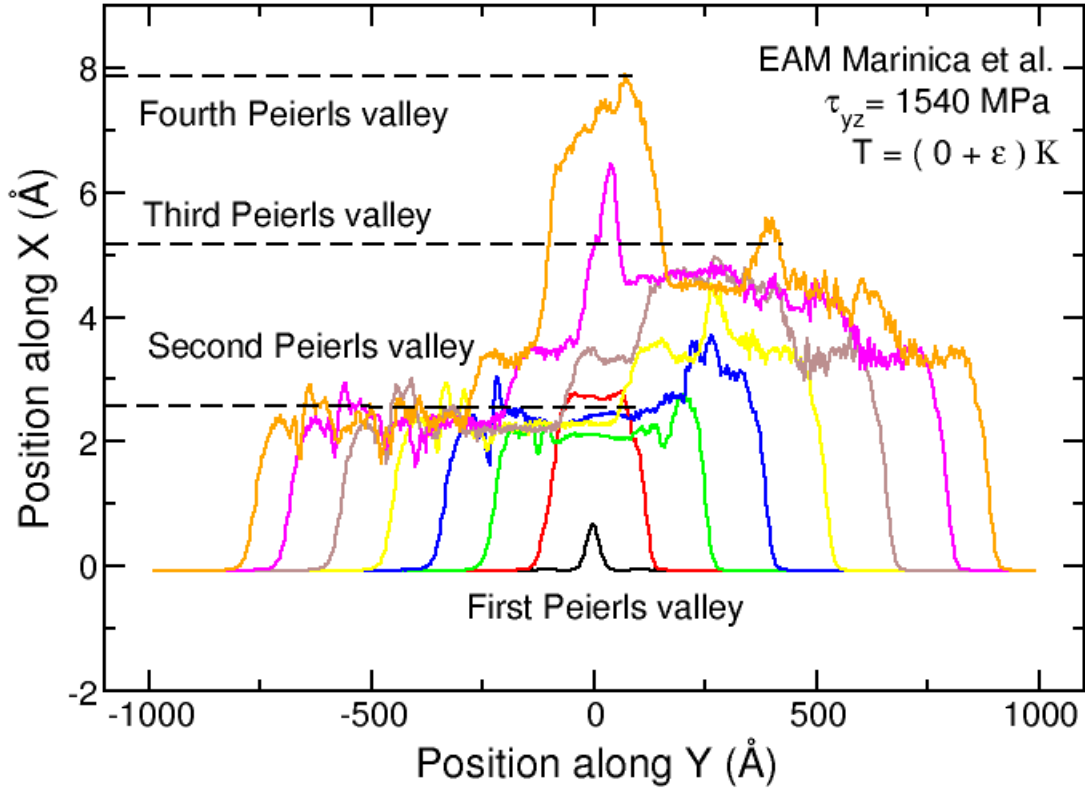


Figure 4.3: MD profiles of simulations of kink propagation for temperature close to 0 K, i.e.  $T = (0 + \epsilon)$  K for EAM4 [1] performed at an applied shear stress,  $\tau_{yz} = 1.54$  GPa.

#### 4.3.1 Simulations at $T = (0 + \epsilon)$ K

In Fig. 4.2, we have reported the time integrated MD profiles of the screw dislocation in bcc tungsten as it starts to glide from its initial position. These simulations were carried out at an applied shear stress,  $\tau_{yz} = 1$  GPa and at a temperature close to 0 K i.e.  $T = (0 + \epsilon)$  K. This stress level is lower than all the Peierls stress values predicted by the four EAM potentials developed by Marinica *et al* i.e. EAM4a-EAM4d. In this case, we see that the standard Peierls mechanism is observed as the initial central kink develops into a full grown kink in the next Peierls valley and continues to propagate outwards along this Peierls valley on both the sides.

After that we performed more simulations by gradually increasing the value of the applied shear stress. At an applied shear stress of  $\tau_{yz} = 1.54$  GPa, we saw the appearance of a macro-kink as

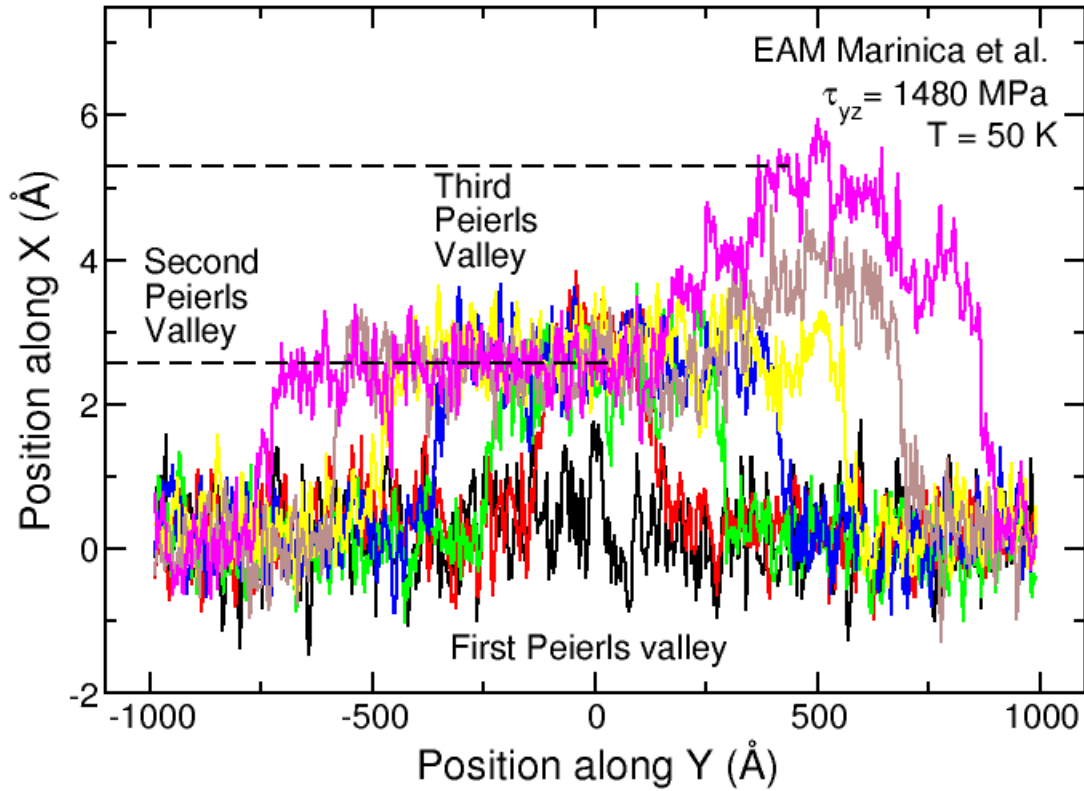


Figure 4.4: MD profiles of simulations of kink propagation for temperature close to 0 K, i.e.  $T = 50$  K for EAM4 [1] performed at an applied shear stress,  $\tau_{yz} = 1.48$  GPa.

in the case of iron. This has been shown in Fig. 4.3. We observe that there were two additional kink pair nucleations constituting the macro kink, thus leading to a long jump extending over 3 Peierls valleys. So as per our observations in the case of bcc iron, we proceeded to examine the effect of temperature on the jerky motion of the screw dislocation. Previously for iron, we would like to recall that it was found that temperature aids the phenomenon of jerky motion and the application of temperature resulted in the occurrence of jerky motion at lower stress levels compared to the case where no external temperature was provided.

### 4.3.2 Simulations with the application of temperature

We performed a number of simulations at stress levels lower than the stress level of occurrence of jerky motion without the application of temperature. Simulations were carried out at intervals of applied stress levels 20 MPa lower each time. For each stress level, different simulations were performed increasing the applied temperature on each occasion. Finally, at an applied shear stress,  $\tau_{yz} = 1480$  MPa and at a temperature of  $T = 50$  K, we were able to observe the appearance of a macro-kink yet again, confirming our earlier observation for bcc iron that temperature aids the process of jerky motion. The same has been plotted in Fig. 4.4. This is an important observation in our simulation as we can conclude that temperature aids the process of jerky motion for bcc metals in general.

## 4.4 Plot of kink pair formation enthalpy and kinetic energy of traveling kinks against applied stress

In Fig. 4.5, the enthalpy of formation of kink pairs for each level of  $\tau_{yz}$  computed with NEB and the variation of the sum of kinetic energies of all atoms associated with each dislocation line segment of length  $b$  have been plotted. They are represented by the blue line and the red line respectively. We see that the enthalpy of kink pair formation keeps decreasing with the applied shear stress and the kinetic energy of kinks keeps increasing during the same time. By extending the red curve linearly, we observe that the two lines intersect at a point, implying that the kinetic energy of the kinks is sufficient enough for the nucleation of a secondary kink pair. This explains the energetics of the occurrence of additional kink pairs in our simulations. In the following section we draw a comparison between the jerky motion observed in iron with the jerky motion observed in the case of tungsten.

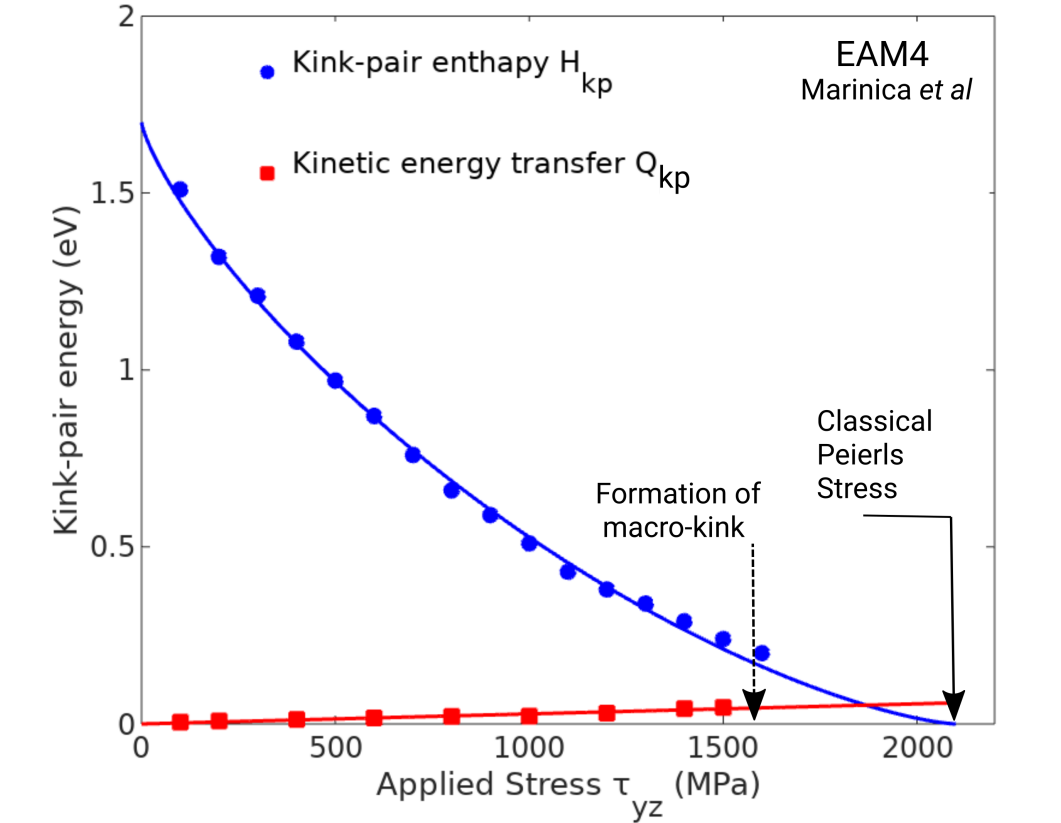


Figure 4.5: Kinetic energy transfer from kink motion against  $\tau_{yz}$ . Black line : activation enthalpy for the nucleation of a kink pair  $H_{kp}$  ; Red line : steady value of the kinetic energy transfer  $Q_{kp}$ . The symbols represent values from atomistic simulations and the curves are according to analytical fits. Blue line : activation enthalpy for the nucleation of a kink pair  $H_{kp}$  ; Red line : steady value of the kinetic energy transfer  $Q_{kp}$ . The analytical fit for the kink pair formation enthalpy is :  $H_{kp} = H_0[1 - (\frac{\tau_{yz}}{\tau_P})^{0.78}]^{1.42}$  and that for the kinetic energy along the dislocation segments is :  $Q_{kp} = 0.06 \frac{\tau_{yz}}{\tau_P}$ .

## 4.5 Comparison of the jerky motions observed in bcc iron and tungsten

Here we recall from chapter 3 that for bcc iron, the jerky motion was observed at applied shear stress levels of  $\tau_{yz} = 450$  MPa,  $\tau_{yz} = 650$  MPa and  $\tau_{yz} = 920$  MPa for EAM1, EAM2 and EAM3, respectively for the simulations carried out at  $T = (0 + \epsilon)$  K. Following this, for all the three EAMs the jerky motion was observed again at applied shear stresses 50 MPa lower than these values when the temperature was applied to our simulations. The temperatures required were  $T = 30$  K for EAM1,  $T = 25$  K for EAM2 and  $T = 25$  K for EAM3. For the case of tungsten too, the jerky motion was observed at around 50 MPa lower with the application of temperature, but the temperature required was much higher i.e.  $T = 50$  K. Even with a higher temperature being applied, we observed that the macro-kink extends over 2 Peierls valleys only i.e. it extends from the first (initial) Peierls valley up to the third Peierls valley (Fig. 5.3). For the case of bcc iron we had observed that the macro-kink extended over a distance of 4, 10 and 5 Peierls valleys respectively for the EAMs, EAM1, EAM2 and EAM3, although the applied temperatures were around half of what was applied for the case of tungsten. Thus we can conclude that the effect of temperature is much more pronounced in the case of iron when compared to tungsten. We can also state that the phenomenon of jerky motion is easier to occur in iron when compared to tungsten.

## 4.6 Experimental observations of Dr. Caillard for Tungsten

Recently Dr. Caillard has published his experimental results for in-situ straining experiments carried out for pure tungsten to study the geometry and kinetics of glide of dislocations with respect to applied stress and temperature [153]. Experiments were carried out on a single crystal of pure tungsten procured from P. Gumbsch and D. Weygand. This material had previously been analysed by Brunner and his colleagues [164] and contained less than 1 ppm

of O, C, N, and Si, and less than 0.1 ppm at of other elements. Like in the case of iron 3 mm by 1 mm rectangular specimens were cut along different orientations by spark cutting and mechanically polished to a thickness of 10 mm. A thin edged hole was created at the center of each specimen by the process of electropolishing. After that the specimens were glued on a copper grid fixed on a Gatan low-temperature straining holder for experiments carried out between 95 K and 300 K. For the experiments in the excess of 300 K, the samples were glued on a home-made high-temperature straining device utilising a high-temperature cement. The entire experimental procedures were recorded using a Megawiew III camera and subsequently all the frames were analyzed.

Dr. Caillard arrived at a number of conclusions from the observations during his experiments. With regards to the glide of the screw dislocations which concerns our study, he found that the plasticity of tungsten depends on the motion of straight screw dislocations in the temperature range between 95 K and 573 K. Breaking down this temperature regime Dr. Caillard observed jerky type of motion at 300 K and 473 K. However interestingly it was found that the dislocations are not entirely mobile in the intermediate time between two consecutive jumps where they move quite slowly and steadily as per the classical theory. The movement is highly jerky at around 473 K and the jerky motion is visible at temperatures lower than it. On the other hand, the steady classical motion becomes extremely slow at 300 K and around 200 K the motion becomes too slow and limited in number for a proper analysis. Further experiments show that at 573 K, there is a recurrence of purely steady motion of the screw dislocations (as per the standard Peierls mechanism) but this motion is quite fast compared to the observations at lower temperatures. With regards to the tensile axes, Dr. Caillard concluded that for tensile axes other than the  $\langle 110 \rangle$  screw dislocations move by a combination of steady and jerky motion in planes which cannot be identified unambiguously. For a tensile axis close to  $\langle 110 \rangle$ , however, screw dislocations have a much jerkier motion with jumps over large distances, exactly in the (112) planes (only in the twinning direction) and in addition, in the (123) planes also. All these observations were found to be in excellent agreement with previous results of Argon and Maloof [165]. The conclusions of the research work was that the jerky motion and the steady motion are quite different in nature. The stress and temperature dependences of the steady

motion follow the classical laws of thermodynamics but the same can not be said for the jerky motion. The stress discrepancy is evidently due to a change of dislocation mechanism, from the standard Peierls mechanism at high temperature to the jerky motion at low temperature.

## 4.7 Comparison of our simulations with Dr. Caillard's experimental observations

From our computational observations, there is agreement with the experimental observations that for the case of tungsten, the motion of screw dislocations is more difficult in comparison with the screw dislocation mobility in bcc Fe with regards to sensitivities to applied shear stress and temperature. In the experiments, the jerky motion was observed at higher temperatures (compared to bcc Fe) i.e.  $> 300$  K whereas in our simulations we observed jerky motion at 50 K which is still twice the temperature which we employed for the case of Fe. Moreover the macro-kink was seen to extend over 2 Peierls valleys only indicating that much more temperature has to be applied in order to observe a large macro-kink extending over several Peierls valleys. In our simulations, it becomes difficult to observe clearly the dislocation profiles if we apply larger temperatures. This is due to the fact that the energies and vibrations of individual atoms that comprise the screw dislocation increases drastically with the application of larger temperatures which result in the profiles being too haphazard to be identified clearly when plotted. Thus it is difficult to verify exactly what happens at very large temperatures employed in the experiments, but the general observation in the simulations are in agreement with the experimental trends.

# Chapter 5

## Conclusion

In the concluding section, we would like to summarize the goals of the thesis, the motivation behind them and the extent to which they have been realized. The methods that have been employed to reach our goals and their effectiveness are highlighted here and the applications of our work are discussed. We also discuss the perspectives of our work, how it may be improved upon and how it can benefit the scientific research community in the future.

### 5.1 Summary of results

We started off our work motivated by some very interesting and new experimental observations that could not be explained by existing classical theory of dislocation mechanism. These observations were the jerky motion or long jumps (extending several Peierls valleys) undergone by the screw dislocations at low temperatures, instead of the conventional Peierls mechanism in the experiments performed by Dr. D. Caillard for pure iron. The aim was to find out the facts that provide an explanation for such occurrence at the atomistic scale. We chose to work with MD simulations to study the motion of the entire screw dislocation by tracking the motion of the individual atoms that constitute the dislocation.

We identified two limitations with the traditional MD simulation process that needed to be addressed in order to simulate the motion of a screw dislocation. The first was the limited

length of the simulation cell and hence the screw dislocation that MD could handle. These sizes were not at all comparable to the dislocation sizes that were observed in the experiments. The next limitation was that MD simulations can be carried out only upto the time scale of pico seconds. This time scale is much smaller compared to the time required for the nucleation of a pair of kinks on a straight screw dislocation which is of the order of seconds. Hence we performed NEB calculations with 50 images to find out the MEP between an initial and final straight states of a screw dislocation. Since the NEB uses 50 system replicas, the simulation cell size was limited in size. We picked up the saddle state kinked profile of the screw dislocation and placed it in a central simulation cell of the same size. Then on both sides of this central cell we employed PBC conditions to place extensions of the same central cell. In these extensions we placed straight screw dislocation segments. Thus at the end, we had a very long extended simulation cell with a long screw dislocation (comparable to the sizes observed in experiments) having a kink pair right at the centre of the dislocation. We had thus solved both the problems that we had identified at the beginning and we then proceeded to perform MD simulations using different EAM potentials.

The results with all the three EAM potentials showed that as we kept on gradually increasing the applied shear stress in successive simulations, the recorded dislocation profiles showed a change of mechanism at sufficiently high shear stresses but below the corresponding Peierls stresses. It was seen that the dislocations moved as per the standard Peierls process at lower stresses i.e. from one Peierls valley to the adjacent as the kink grew in size initially reaching the adjacent valley and continued to propagate outward along the dislocation while being in this new valley. At stress levels high enough, the recorded profiles that we plotted show that a new kink pair nucleates from the primary ones at a certain point along their outward propagation and these secondary kinks grow in size and reach the next valley and start to propagate outward giving rise to more kink pairs till the original kink pair extends over several Peierls valleys.

This was a very interesting observation comparable to the sudden long jumps of screw dislocations observed by Dr. Caillard. Such mechanism occur very fast i.e. at the time scale of pico-seconds whereas in the experiments the observations were made for 25 frames per second. So this huge difference of time scale appears to be the reason why the gradual extension of the

kinks over multiple Peierls valleys appeared to be just a simple jump extending several valleys in the experiments.

Next in order to find out the reason behind such phenomena, we identified that there has to be a source of some energy responsible for such jumps. As the kinks are in motion along the dislocation line, we proceeded to measure the associated kinetic energies of the travelling kinks. For this purpose, we divided the entire dislocation line into segments each of length  $b$ , and measured the total kinetic energies of all the atoms in each kink located at  $b$ . These kinetic energies were found to increase gradually with increasing levels of applied shear stress. On the other hand, from our NEB computations we had the information about the enthalpy of kink pair nucleation for different values of applied shear stresses. When plotted, these enthalpies were found to decrease significantly with increasing levels of applied shear stress. By plotting both the kinetic energies and kink nucleation enthalpies against the applied shear stress, it was observed that the two curves intersect at some point below the Peierls stress level, implying that the kinks have sufficient energies at this point for the nucleation of new kink pairs which can explain the nucleation of secondary kinks previously observed in our simulations. The point of intersection of the two curves is very close to the stress levels at which we observed the macro-kinks in our simulations leading us to believe more that the kinetic energies of the travelling kinks are the reason for jerky motion because at higher stress levels the energy required for nucleation of new kink pairs are significantly low.

We also observed that for stress levels sufficient for the formation of macro kinks in our simulations, the nucleation of the secondary kinks takes place quicker for higher stress levels i.e. the primary kinks travel much lesser distance along the dislocation line till the point of nucleation of secondary kinks, for higher values of applied shear stresses. We also studied the effect of temperature on these phenomena and were able to conclude that temperature aids the process of jerky motion i.e. the first seen macro kink nucleation can occur at a lower stress level with the application of temperature. Similar trends were also observed in the case of bcc tungsten, although we found that the jerky motion takes place much easier for bcc iron i.e. the jumps are longer and the effect of temperature is more prominent in the case of iron.

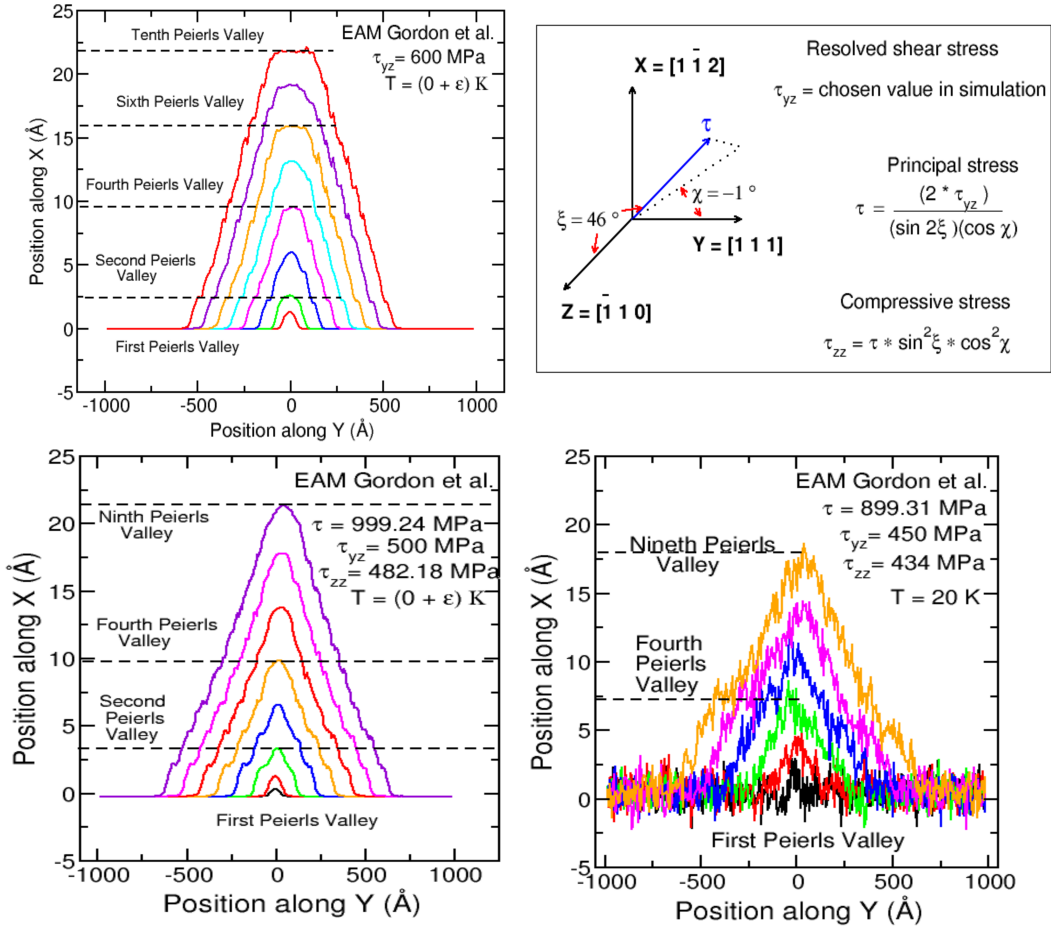


Figure 5.1: MD profiles of simulations for kink propagation with EAM2 [99] showing: (a) Jerky motion at an applied shear stress,  $\tau_{yz} = 600$  MPa and  $T = (0 + \epsilon)$  K (b) Orientation A [87, 101] of the crystal. (c) Jerky motion at an applied principal stress  $\tau = 999.24$  MPa, resolved shear stress component,  $\tau_{yz} = 500$  MPa, and resolved compressive stress component,  $\tau_{zz} = 482.18$  MPa at temperature,  $T = (0 + \epsilon)$  K and (d) Jerky motion at an applied principal stress  $\tau = 899.31$  MPa, resolved shear stress component,  $\tau_{yz} = 450$  MPa, and resolved compressive stress component,  $\tau_{zz} = 434$  MPa at temperature,  $T = (0 + \epsilon)$  K.

## 5.2 Future perspective

We recently made some studies on the effects of non-glide/compressive stresses on the motion of screw dislocations. The reason being that in the experiments and also in our simulations reported in the previous chapters, we had considered only pure shear stresses acting along the glide plane of the screw dislocation. In practical applications, there are different components of stresses acting on these materials depending on their orientation and hence the effects of such stresses should also be studied and deciphered.

In Fig. 5, using EAM2, we have plotted the effects of compressive stresses, using a crystallo-

graphic orientation A [87, 101] wherein the principal stress acts at an angle to the simulation cell. The angle made with the Z-direction and the angle between the projection of the principal stress on the XY glide plane and the line direction Y are fixed according to the Orientation A. It was found that compressive stresses aid the process of jerky motion just like the addition of temperature, which too was found to aid the process of jerky motion. The shear component of the stress was first chosen in order to be able to compare with previous simulations. From the shear stress value, the values of the principal stress and the compressive component were derived. The combined effect of compressive stress and temperature led to further decrease of the applied shear stress level at which the jerky motion was observed. For the case of pure shear stress, as previously reported, the jerky motion was observed at 600 MPa, whereas after considering the compressive stress effect, the jerky motion was observed at 500 MPa. Then repeating the simulations at an applied temperature of 20 K in the presence of compressive component of the stress, the jerky motion was observed at an even lower shear stress level of 450 MPa. Thus the jerky motion is observed at stress values, much below the Peierls stress value of 800 MPa for EAM2.

By continuing further into this work we could quantify different aspects associated with the jerky motion. Knowing the applied shear and compressive stresses and temperature levels, one could predict the extent of the jerky motion i.e. parameters like the number of Peierls valleys over which the jump extends, the time required for such a long jump to occur, the waiting time between jumps and so on. This will enable a much deeper understanding of bcc metals at very low temperature ranges which can help in the safe design of devices and equipments operating at such low temperatures and built using these bcc metals.

This knowledge could also be gradually extended for the case of all bcc metals and even some binary alloys, thus allowing for the research and development of a wide range of materials that can be potentially used for different low temperature applications in the field of science and technology.

# Chapter 6

## Resumé

Le glissement activé thermiquement de dislocations de vis dans des cristaux de symétrie cubiques centrés (bcc) se poursuit par la formation et la propagation de paires de décrochement au moyen du mécanisme de Peierls [9], nommé d'après Peierls pour ses premiers travaux sur la théorie de la dislocation. Le mouvement des dislocations des vis est contrôlé par un potentiel périodique provenant de leur structure centrale non planaire, connu sous le nom de potentiel de Peierls [9]. Le mécanisme [9], accepté comme processus standard de glissement de dislocation, explique que les dislocations se déplacent par étapes d'une vallée de Peierls [9] à une vallée adjacente, etc., entraînant un glissement général d'une partie du cristal à une autre. Cependant, une série d'expériences *in situ* sur du Fe ultra-pur de symétrie cubiques centrés (bcc), réalisées par le Dr D. Caillard à diverses températures, et en fonction de la contrainte, ont permis de faire des observations intéressantes. On a constaté que dans le régime à basse température de 100 à 300 K, les segments de vis droits ont un mouvement saccadé dans les plans (110), ce qui est très différent du mécanisme classique de Peierls observé à température ambiante. Le mouvement saccadé fait référence à un phénomène observé lors d'expériences dans lequel la dislocation, au lieu de glisser progressivement d'une vallée de Peierls à celle adjacente, fait un saut en longueur de plusieurs vallées de Peierls. Comme la théorie classique n'arrivait ni à expliquer ni à prévoir ce phénomène, nous avons consacré notre énergie à prévoir une nouvelle théorie généralisée à l'échelle atomique capable de prédire le comportement des dislocations de vis avec une précision

acceptable sur toute la plage de températures.

Nous avons choisi de réaliser des simulations de dynamique moléculaire (MD) permettant de prédire comment les atomes interagissent avec d'autres atomes, c'est-à-dire comment leurs paramètres de mouvement changent et comment un système évolue avec le temps. En connaissant une configuration de départ de tous les atomes du système, nous sommes capables de prédire simultanément les nouvelles positions et vitesses à chaque étape de temps en fournissant un algorithme (algorithme de vitesse standard par Verlet [132]), qui permet le changement et en intégrant les lois du mouvement de Newton. Nous avons choisi de travailler avec les potentiels EAM pour prédire et modéliser les énergies des cristaux, car ils nous permettent de travailler avec un grand nombre d'atomes et de permettre également un calcul direct de l'enthalpie de formation de paires de décrochements de dislocations de vis en 3D.

La cellule de simulation, était considérée comme une géométrie cristalline parfaite et une dislocation de vis est introduite en déplaçant tous les atomes selon la solution élastique isotrope [113]. Afin de reproduire un plan de glissement infini, la condition de limite périodique (PBC) est utilisée dans les directions  $X = [\bar{1} \bar{1} 2]$  et  $Y = [1 1 1]$ , constituant le plan de glissement XY. Un décalage supplémentaire de  $b/2$  est introduit le long de la ligne de dislocation (Y), afin de prendre en compte la déformation plastique associée à la dislocation de la vis et de reconnecter les surfaces gauche et droite perpendiculairement à la ligne de dislocation. Cela garantit l'existence de la dislocation de la vis pendant le processus de calcul à tout moment. La présence de ce vecteur de Burgers différent de zéro n'autorise pas les conditions aux limites périodiques dans la direction restante  $Z = [\bar{1} 1 0]$  ; deux surfaces libres sont donc créées pour former une dalle [101]. Le paramètre réseau du cristal parfait est représenté par  $a_0$  et le vecteur de Burgers  $b = (a_0/2) [111]$  correspond au sens de la ligne (Y) de la dislocation de la vis. Nous nous sommes assurés que les dimensions le long des directions de glissement ( $x = 14b$ ,  $y = 160b$ ,  $z = 20b$  où  $b = 2,48 \text{ \AA}$  pour  $\alpha\text{-Fe}$ ) sont suffisamment grandes pour éviter des interactions trompeuses avec les images périodiques.

Nous effectuons d'abord une trempe de notre cellule de simulation chargée d'une contrainte de cisaillement appliquée sur les surfaces yz situées au-dessus et au-dessous de la cellule pour une

position initiale et finale d'une dislocation rectiligne le long du plan de glissement. Les forces résultant de telles contraintes initient le mouvement de la dislocation qui est limité en couplant l'équation du mouvement de Newton des atomes individuels à un simple amortissement de Langevin. Nous considérons que la cellule a atteint l'équilibre lorsque les forces atomiques ont diminué pour se situer autour de  $10^{-5}$  eV/Å. En utilisant ces positions initiale et finale relâchées de la dislocation de la vis, les calculs de la bande élastique Nudged (NEB) [133, 134] sont ensuite effectués pour calculer le chemin d'énergie minimal (MEP) de la dislocation de la vis lorsqu'elle glisse de la position initiale à la position finale. Cependant, dans la méthode NEB, de nombreuses images ou répliques du système (50 dans notre cas) sont créées et reliées entre elles par des ressorts de manière à représenter un chemin discret d'une configuration initiale I à une configuration finale F. Par conséquent, la cellule de simulation a une longueur limitée et les dislocations sont très courtes comparées aux longueurs observées par le Dr Caillard dans les expériences. Cela pourrait entraîner l'exclusion de certains phénomènes susceptibles de se produire lorsque les décrochements se propagent le long de la ligne de dislocation au-delà de la longueur considérée dans nos simulations. De plus, les décrochements nécessitent de parcourir des distances beaucoup plus longues pour atteindre une vitesse constante. Afin de remédier à cela, nous avons d'abord étendu notre cellule de simulation en prenant en compte les conditions aux limites périodiques le long de la direction Y, c'est-à-dire en prenant une cellule de simulation (identique à celle utilisée pour les calculs NEB) et en l'étendant deux fois dans les directions Y positive et négative. De cette façon, nous avons construit une nouvelle cellule de simulation cinq fois plus longue que la cellule d'origine. La longueur de la cellule de simulation étendue est de 2000 Å ou 0.2  $\mu\text{m}$ , ce qui est comparable à la longueur des dislocations observées par D. Caillard dans ses expériences. Afin de nous rapprocher du montage expérimental, nous avons gelé les surfaces d'extrémité Y de la cellule de simulation étendue le long de la ligne de dislocation, c'est-à-dire que nous avons fixé les atomes sur les surfaces d'extrémité. Nous avons ensuite relevé la première configuration de la dislocation à l'état de selle dans le calcul de NEB et nous l'avons placée dans la cellule centrale de la cellule étendue. Nous avons ensuite placé 2 segments droite de dislocation dans chaque côté de la cellule centrale, ce qui aboutit à une dernière cellule étendue, 5 fois plus longue que celle de NEB. La dislocation comporte une petite

paire de décrochement au milieu de la ligne de dislocation. Cette astuce nous permet de relancer de nouvelles simulations MD à partir d'un état de selle sans attendre infiniment la survenue d'un événement rare tel que la nucléation de paires de décrochements (dont les échelles de temps sont de l'ordre du milli-seconde alors que MD ne peut être exécuté que jusqu'à nano-secondes).

Les simulations ont été lancées avec des combinaisons de différents niveaux de contraintes de cisaillement appliquées, de températures différentes et en utilisant différents potentiels inter-atomiques: EAM1 [107], EAM2 [99] et EAM3 [98] afin de déterminer les tendances communes observées avec les trois EAMs. Les premières simulations ont été réalisées sans application de température et à des niveaux de contrainte inférieurs aux contraintes de Peierls [9] (contrainte nécessaire pour vaincre la résistance des cristaux en absence de fluctuations thermiques). Les valeurs de contrainte de Peierls prédites par les simulations atomistiques pour EAM1 [107], EAM2 [99] et EAM3 [98] sont respectivement de 600 MPa, 900 MPa et 1000 MPa. Nous avons tracé les profils MD de la dislocation à des intervalles définis dans le temps pour les simulations effectuées avec EAM1 [107] à une contrainte de cisaillement appliquée  $\tau_{yz} = 300$  MPa, avec EAM2 [99] à une contrainte de cisaillement appliquée  $\tau_{yz} = 500$  MPa et avec EAM3 [98] à une contrainte de cisaillement appliquée  $\tau_{yz} = 800$  MPa. Nous avons constaté que, dans les trois cas, la paire de décrochement initialement grossissait progressivement de l'état selle jusqu'à ce qu'elle se trouve dans la vallée adjacente de Peierls [9], puis se propagent le long de la ligne de dislocation comme prévu dans la théorie standard. Ensuite, afin d'étudier l'effet de la température, nous avons considéré les trois mêmes cas que dans le premier ensemble de simulations, la seule différence était que de petites températures ( $T = 5$  K et  $T = 10$  K) ont été appliquées à la cellule de simulation pour deux séries différentes de simulations. Afin d'introduire la température dans nos simulations, nous avons conçu notre code pour atteindre la température souhaitée en désignant les vitesses initiales des atomes selon une distribution aléatoire de Maxwell-Boltzmann. Ce processus repose sur une base statistique plus solide que l'utilisation d'un thermostat, car il repose sur le bain de chaleur atomistique réel d'un système plus grand plutôt que sur un algorithme de thermostat particulier.

Pour les deux séries de simulations, le mécanisme de Peierls Nabarro standard a de nouveau été observé à chaque fois. Les profils sont également apparus assez similaires aux profils respectifs

dans le cas sans aucune température appliquée. Cependant, il n'est visuellement pas possible de savoir si l'application de la température a un effet sur les vitesses des décrochements qui se propagent, ce qui pourrait à son tour affecter la vitesse de glissement de toute la dislocation. Nous avons donc commencé à tracer les vitesses de décrochement en fonction de l'évolution du temps pour trois régimes de température différents  $T = 0$  K,  $T = 5$  K et  $T = 10$  K pour les trois potentiels EAM1, EAM2 et EAM3 respectivement. Les vitesses proviennent des résultats de notre simulation, c'est-à-dire du changement de position des décrochements qui se propagent le long de la ligne de dislocation avec l'évolution du temps. On voit que dans tous les cas, les vitesses de décrochement atteignent finalement une valeur asymptotique. Nous avons observé que la température n'a pas d'effet sur la vitesse des décrochements, en accord avec les prédictions précédentes de T.D. Swinburne et al. [10].

Nous avons ensuite procédé à des simulations à des niveaux de contrainte plus élevés et avons également testé les effets de la température dans ce régime. À des contraintes suffisamment élevées, au-dessus d'un certain seuil, nous avons constaté que, tout au long de la propagation des décrochements primaires, se produisaient la nucléation de paires de décrochements supplémentaires. L'accumulation de ces décrochements supplémentaires conduit à la formation d'un macro-décrochement qui s'étend de la première vallée de Peierls à une autre, bien au-delà de la vallée de Peierls la plus proche. Ce phénomène a été observé avec les trois potentiels EAM1, EAM1 [107], EAM2 [99] et EAM3 [98], et différentes combinaisons de contrainte de cisaillement et de température. C'est une observation intéressante qui ressemble au mouvement saccadé observé dans les expériences du Dr Caillard. Il était également intéressant d'observer que, pour les trois EAM, le niveau de contrainte de cisaillement appliqué auquel le mouvement saccadé était observé continuait à diminuer à mesure que la température appliquée augmentait. On peut donc en conclure que la température facilite le processus de mouvement saccadé. L'autre tendance commune observée avec les trois EAM est que le mouvement saccadé s'est produit à des valeurs de contrainte bien inférieures aux niveaux de contrainte de Peierls attribués à chaque EAM. En outre, avec l'application de la température, le mouvement saccadé a été observé à des niveaux de contrainte de cisaillement appliqués plus bas pour les trois potentiels d'EAM.

Ensuite, nous voulions examiner ce qui se produirait si la contrainte de cisaillement appliquée était encore augmentée, au-delà du point d'apparition primaire du mouvement saccadé. En prenant comme exemple le cas de EAM1, un autre ensemble de simulations a été réalisé à  $\tau_{yz} = 550$  MPa, à un niveau de contrainte supérieur de 100 MPa au niveau principal d'occurrence du mouvement saccadé, à savoir 450 MPa. Comme prévu, un macro-décrochement a été observé à nouveau. En observant de plus près les profils MD intégrés dans le temps, nous avons constaté que, dans le premier cas, la nucléation de la paire de décrochement secondaires se produit après la primaire décrochement a parcouru une distance de 600 Å de la position de départ alors que dans le deuxième cas, ce phénomène s'est produit après une distance beaucoup plus petite de 250 Å. Cela conduit à déduire que la période de temps pour la survenue d'un mouvement saccadé diminue avec l'augmentation des niveaux de contrainte de cisaillement appliqués. Cela signifie également qu'un certain type d'énergie est accumulé dans la dislocation de la vis en raison de la nucléation de plusieurs paires de décrochements.

À partir des calculs NEB précédemment effectués, nous avons eu une idée de la variation de l'enthalpie de formation de paires de décrochements avec différentes contraintes de cisaillement appliquées en la traçant en fonction de la contrainte de cisaillement appliquée sur toute la plage de travail de nos simulations. Il a été observé que l'enthalpie de la formation de paires de décrochement diminue progressivement à mesure que la valeur de contrainte de cisaillement appliquée augmente. Ensuite, afin de calculer l'énergie accumulée dans la dislocation de la vis responsable de la formation de décrochements secondaires, nous avons divisé toute la longueur de la dislocation de la vis en segments de longueur  $b$  chacun. Ensuite, nous avons calculé les énergies cinétiques combinées de tous les atomes associés à un décrochement situé en  $b$  le long de la ligne de dislocation pour différentes valeurs de la contrainte de cisaillement appliquée. Sur le même graphique pour l'enthalpie de formation de paires de décrochements, nous avons ensuite tracé ces énergies cinétiques en fonction de l'augmentation de la contrainte de cisaillement appliquée. En prenant comme exemple le cas avec EAM1 [107], il a été observé que l'énergie cinétique augmente progressivement avec la contrainte de cisaillement appliquée et en prolongeant la courbe pour l'énergie cinétique, nous avons observé que cette courbe intersecte le tracé de l'enthalpie de formation de paires de décrochements en un point. Et le niveau

de contrainte de cisaillement correspondant est très proche de la contrainte de cisaillement à laquelle le mouvement saccadé a été observé dans nos simulations. Nous pouvons donc en conclure qu'à ce niveau de contrainte de cisaillement appliqué, l'énergie cinétique accumulée à cause des décrochements en déplacement, devient suffisante pour la nucléation de nouvelles paires de décrochements, ce qui conduit finalement à la formation d'un macro-décrochement, comprenant plusieurs paires de décrochements et s'étendant sur plusieurs vallées du Peierls. Des tendances similaires ont également été observées avec EAM2 et EAM3.

Ensuite, afin d'étudier si le mouvement saccadé se produit dans d'autres cristaux de BCC, nous avons effectué des simulations pour le tungstène (W) en utilisant le seul potentiel EAM approprié que nous avons trouvé dans la littérature, à savoir EAM4 ([154]). Des tendances similaires, telles que la diminution de la période d'apparition du mouvement saccadé avec l'augmentation des niveaux de contrainte de cisaillement appliquée, et la température aidant le processus du mouvement saccadé ont été observées, conformément à nos observations pour bcc Fe. Cependant, l'effet de la température est beaucoup plus marqué dans le cas du fer que dans celui du tungstène. Dans le cas du tungstène, le mouvement des dislocations de vis est plus difficile comparé à la mobilité des dislocations de vis dans bcc Fe en ce qui concerne les sensibilités à la contrainte de cisaillement appliquée et à la température.

Pour les perspectives futures, en continuant plus loin dans ce travail, nous pourrions quantifier différents aspects associés au mouvement saccadé. Connaissant les contraintes de cisaillement appliquées et les niveaux de température, il est possible de prédire l'ampleur du mouvement saccadé, c'est-à-dire des paramètres tels que le nombre de vallées de Peierls sur lesquelles le saut s'étend, le temps requis pour qu'un saut aussi long se produise, le temps d'attente entre les sauts, etc. Cela permettra une compréhension beaucoup plus approfondie des métaux bcc à très basses températures, ce qui peut aider à la conception en toute sécurité d'appareils et d'équipements fonctionnant à des températures basses et construits à l'aide de ces métaux bcc.

# Bibliography

- [1] Taylor, G. I., *The mechanism of plastic deformation of crystals. Part I. Theoretical.* Proc. Roy. Soc. A, 1934. 145: p. 362.
- [2] Mott, N. F. and Nabarro, F. R. N., *Report on Strength of Solids.* Physical Society London, 1948. p. 2.
- [3] Nabarro, F. R. N., *Report on Strength of Solids.* Physical Society London, 1948. p. 38.
- [4] Schmid, E., *Zn - normal stress law.* 1st International Congress for Applied Mechanics., 1924. Delft: Technische Boekhandel en Drukkerij J.Waltman Jr.
- [5] Schmid, E. and Boas, W., *Kristallplastizitt.* Berlin, Springer., 1935.
- [6] Seeger, A. Flgge, S.(Ed.), *Encyclopaedia of Physics.* Springer, Berlin., 1958. VII: p. 1.2.
- [7] Taylor, G. I. and Elam, C. F., *The distortion of iron crystals.* Proc. Roy. Soc. Lond. A, 1926. 112: p. 337.
- [8] Taylor, G. I., *The deformation of crystals of beta-brass.* Proc. Roy. Soc. Lond. A, 1928. 118: p. 1.
- [9] Peierls, R., *The size of a dislocation.* Proc. Phys. Soc., 1940. 52: p. 34.
- [10] Duesbery, M. S., *The dislocation core and plasticity.* Dislocations in Solids, 1989. 8: p. 67.
- [11] Christian, J., *Some surprising features of the plastic deformation of body-centered cubic metals and alloys.* Metall. Mater. Trans. A, 1983. 14: p. 1237.

- [12] Mitchell, T. E., Foxall, R. A. and Hirsch, P. B., *Work-hardening in niobium single crystals*. Philos. Mag., 1963. 8: p. 1895.
- [13] Mitchell, T. E. and Spitzig, W. A., *Three-stage hardening in tantalum single crystals*. Acta Metall., 1965. 13: p. 1169.
- [14] Bowen, D. K., Christian, J. W. and Taylor, G., *Deformation properties of niobium single crystals*. Can. J. Phys., 1967. 45: p.903.
- [15] Foxall, R. A., Duesbery, M. S. and Hirsch, P. B., *The deformation of niobium single crystals*. Can. J. Phys., 1967. 45: p. 607.
- [16] Duesbery, M. S. and Foxall, R. A., *A detailed study of the deformation of high purity niobium single crystals*. Phil. Mag. A, 1969. 20: p. 719.
- [17] Statham, C. D., Vesely, D. and Christian, J. W., *Slip in single crystals of niobium-molybdenum alloys deformed in compression*. Acta Metall., 1970. 18: p. 1243.
- [18] Irwin, G. J., Guiu, F. and Pratt, P. L., *Influence of orientation on slip and strain hardening of molybdenum single crystals*. Phys. Status Solidi A, 1974. 22: p. 685
- [19] Nagakawa, J. and Meshii, M., *Deformation of niobium single crystals at temperatures between 77 and 4. 2 K*. Philos. Mag. A, 1981. 44: p. 1165.
- [20] Hollang, L. and Seeger, A., *The flow-stress asymmetry of ultra-pure molybdenum single crystals*. Mater. Trans. JIM, 2000. 41: p. 141.
- [21] Kirchner, H. O. K., *Plastic deformation of the alkali metals sodium and potassium*. Acta Phys. Austriaca, 1978. 48: p. 111.
- [22] Basinski, Z. S., Duesbery, M. S. and Murty, G. S., *The orientation and temperature dependence of plastic flow in potassium*. Acta Metall., 1981. 29: p. 801.
- [23] Siedersleben, M. E. and Taylor, G., *Slip systems in bcc Li-Mg alloys*. Philos. Mag. A, 1989. 60: p. 631.

- [24] Pichl, W. and Krystian, M., *The flow stress of high purity alkali metals*. Phys. Status Solidi A, 1997. 160: p. 373.
- [25] Dipersio, J. and Escaig, B., Phys. Stat. Sol.(a), 1977. 40: p. 393.
- [26] Basinski, Z. S. and Christian, J., *The influence of temperature and strain rate on the flow stress of annealed and decarburized iron at subatmospheric temperatures*. Austr. J. Phys, 1960. 13: p. 299.
- [27] Blewitt, T. H., Coltman, R. R. and Redmann, J. K., *Proceedings of the Conference on Defects in Crystalline Solids*. London: Physical Society, 1955. p. 369.
- [28] Niewczas, M., Basinski, Z. S., Basinski, S. J. and Embury, J. D., *Deformation of copper single crystals to large strains at 4.2 K*. Phil. Mag. A, 2001. 81: p. 1121.
- [29] Bailey, J. E. and Hirsch, P. B., *The dislocation distribution, flow stress, and stored energy in cold-worked polycrystalline silver*. Phil. Mag., 1960. 5: 486.
- [30] Duesbery, M. S. and Vitek, V., *Plastic anisotropy in b.c.c. transition metals*. Acta mater., 1998. 46: p. 1481.
- [31] Takeuchi, S., *Dislocation core effects on plasticity*. Radiation Effects and Defects in Solids, 1999. 148: p. 333.
- [32] Duesbery, M. S., Vitek, V. Cserti, J. and C. J. Humphreys (ed.), *Understanding Materials: A Festschrift for Sir Peter Hirsch*. London: Institute of Materials, 2002. p. 165.
- [33] Allen, N. P., Hopkings, B. E. and McLennan, L. E., *The tensile properties of single crystals of high-purity iron at temperatures from 100 to -253 C*. Proc. R. Soc. Lond. A., 1956. 234: p. 221.
- [34] Conrad, H. and Schoeck, G., *Cottrell locking and the flow stress in iron*. Acta Mater., 1960. 8: p. 791.
- [35] Conte, R., Groh, P. and Escaig, B., *Etude de l'écoulement plastique de monocristaux filamenteux de fer entre 300 et 4k par*. Status Solidi B., 1968. 28: p. 475.

- [36] Conrad, H. and Frederik, S., *The effect of temperature and strain rate on the flow stress of iron*. Acta Metal., 1962. 10: p. 1013.
- [37] Stein, D. T., Low Jr., J. R. and Seybolt, A. U., *The mechanical properties of iron single crystals containing less than 510–3 ppm carbon*. Acta Metall., 1963. 11: p. 1253.
- [38] Stein, D. T. and Low Jr., J. R., *Effects of orientation and carbon on the mechanical properties of iron single crystals*. Acta Metall., 1966. 14: p. 1183.
- [39] Arsenault, R. J., *Low-temperature creep of alpha iron*. Acta. Metall. Acta. Metall., 1964. 12: p. 547.
- [40] Keh, A. S. and Nakada, Y., *Plasticity of iron single crystals*. Canad. J. Phys., 1967. 45: p. 1101.
- [41] Spitzig, W. A. and Keh, A. S., *Orientation dependence of the strain-rate sensitivity and thermally activated flow in iron single crystals*. Acta Metall., 1970. 18: p. 1021.
- [42] Spitzig, W. A., *Analysis of thermally-activated flow in iron single crystals*. Acta Metall., 1970. 18: p. 1275.
- [43] Altshuler, T. L. and Christian, J. W., *The mechanical properties of pure iron tested in compression over the temperature range 2 to 293 degrees K*. Phil. Trans. R. Soc. Lond. A., 1967. 261: p. 253.
- [44] Aono, Y., Kuramoto, E. and Kitajima, K., *Reports of research institute for applied mechanics*. Kyushu University. 1981. p. 127.
- [45] Brunner, D. and Diehl, J., *The use of stress-relaxation measurements for investigations on the flow-stress of alpha-iron*. J. Phys. Status Solidi A, 1987. 104: p. 145.
- [46] Brunner, D. and Diehl, J., *Extension of measurements of the tensile flow-stress of high-purity alpha-iron single-crystals to very low temperatures*. Zeitschrift Fur Metallkunde, 1992. 83: p. 828.

- [47] Seeger, A., *The temperature and strain-rate dependence of the flow stress of body-centred cubic metals: A theory based on kink-kink interactions*. Z. Metallkde., 1981. 72: p. 369.
- [48] Seeger, A., Veyssiere, P. (ed.), Kubin, L. (ed.) and Castaing, J. (ed.), *Dislocations 1984* C.N.R.S., Paris, 1984. p. 141.
- [49] Brunner, D. and Diehl, J., *Temperature and strain-rate dependence of the tensile flow-stress of high-purity  $\alpha$ -iron below 250 K.I. Stress/Temperature regime-III*. Phys. Stat. Sol. A, 1991. 125: p. 203
- [50] Havner, K. S., *Finite plastic deformation of crystalline solids. Cambridge monographs on mechanics and applied mathematics*. Cambridge University Press: Cambridge, 1992.
- [51] Gough, H. J., *The behaviour of a single crystal of alpha-iron subjected to alternating torsional stresses*. Proc. R. Soc. Lond. A, 1928. 118: p. 498.
- [52] Barrett, C. S., Ansel, G. and Mehl, R. F., *Slip, twinning and cleavage in iron and silicon ferrite*. Trans. Am. Soc. Met., 1937. 25: p. 702.
- [53] Chen, N. K. and Maddin, R., *Slip planes and the energy of dislocations in a body centered cubic structure*. Acta Metall., 1954. 2: p. 49.
- [54] Seeger, A., *Why anomalous slip in body-centred cubic metals?* Mat. Sci. Eng. A, 2001. A319-321: p. 254.
- [55] Seeger, A. and Wasserbaech, W., *Anomalous slip - a feature of high-purity body-centred cubic metals*. Phys. Stat. Sol. A, 2002. 189: p. 27.
- [56] Sigle, W., *High-resolution electron microscopy and molecular dynamics study of the  $(\frac{a}{2})[111]$  screw dislocation in molybdenum*. Philos. Mag. A, 1999. 79: p.1009.
- [57] Mendis, B. G., Mishin, Y., Hartley, C. S. and Hemker, K. J., *Use of the Nye tensor in analyzing HREM images of bcc screw dislocations*. Philos. Mag., 2006. 86: p. 4607.
- [58] Basinski, Z. S., Duesbery, M. S. and Taylor, R., *Influence of Shear Stress on Screw Dislocations in a Model Sodium Lattice*. Can. J. Phys., 1971. 49: p. 2160.

- [59] Vitek, V., Perrin, R. C. and Bowen, D. K., *The core structure of  $\frac{1}{2}(111)$  screw dislocations in b.c.c. crystals*. Phil. Mag. A, 1970. 21: p. 1049.
- [60] Duesbery, M. S., Vitek, V. and Bowen, D. K., *The effect of shear stress on the screw dislocation core structure in body-centred cubic lattices*. Proc. R. Soc. A, 1973. 332: p. 85.
- [61] Vitek, V., *Theory of the core structures of dislocations in BCC metals*. Cryst. Lattice Defects, 1974. 5.1: p. 1.
- [62] Seeger, A. and Wüthrich, C., *Dislocation relaxation processes in body-centred cubic metals*. Nuovo Cim. B, 1976. 33: p. 38.
- [63] Duesbery, M. S. and Basinski, Z. S., *The flow stress of potassium*. Acta metall. mater., 1993. 41: p. 643.
- [64] Ito, K. and Vitek, V., *Atomistic study of non-Schmid effects in the plastic yielding of bcc metals*. Phil. Mag. A, 2001. 81: p. 1387.
- [65] Masuda, K. and Sato, A., *Electronic theory for screw dislocation in b.c.c. transition metals*. Phil. Mag. B, 1978. 37: p. 531.
- [66] Xu, W. and Moriarty, J. A., *Atomistic simulation of ideal shear strength, point defects, and screw dislocations in bcc transition metals: Mo as a prototype*. Phys. Rev. B, 1996. 54: p. 6941.
- [67] Rao, S. I. and Woodward, C., *Atomistic simulations of  $\frac{a}{2} \langle 111 \rangle$  screw dislocations in bcc Mo using a modified generalized pseudopotential theory potential*. Phil. Mag. A, 2001. 81: p. 1317.
- [68] Yang, L. H., Soderlind, P. and Moriarty, J. A., *Accurate atomistic simulation of  $\frac{a}{2} \langle 111 \rangle$  screw dislocations and other defects in bcc tantalum*. Phil. Mag. A, 2001. 81: p. 1355.
- [69] Yang, L. H., Soderlind, P. and Moriarty, J. A., *Atomistic simulation of pressure-dependent screw dislocation properties in bcc tantalum*. Mater. Sci. Engng A, 2001. 309: p. 102.
- [70] Mrovec, M., PhD Thesis, University of Pennsylvania. 2002.

- [71] Ismail-Beigi, S., and Arias, T. A., *Ab Initio Study of Screw Dislocations in Mo and Ta: A New Picture of Plasticity in bcc Transition Metals*. Phys. Rev. Lett., 2000. 84: p. 1499.
- [72] Woodward, C., and Rao, S. I., *Ab-initio simulation of isolated screw dislocations in bcc Mo and Ta*. Phil. Mag. A, 2001. 81: p. 1305.
- [73] Woodward, C., and Rao, S. I., *Flexible Ab Initio Boundary Conditions: Simulating Isolated Dislocations in bcc Mo and Ta*. Phys. Rev. Lett., 2002. 88: p. 216402.
- [74] Frederiksen, S. L., and Jacobsen, K. W., *Density functional theory studies of screw dislocation core structures in bcc metals*. Phil. Mag., 2003. 83: p. 365.
- [75] Domain, C. and Monnet G., *Simulation of Screw Dislocation Motion in Iron by Molecular Dynamics Simulations*. Phys. Rev. Lett., 2005. 95: p. 215506.
- [76] Chaussidon, J., Fivel, M. and Rodney, D., *The glide of screw dislocations in bcc Fe: Atomistic static and dynamic simulations*. Acta Mater, 2006. 54: p. 3407.
- [77] Ventelon, L. and Willaime, F., *Core structure and Peierls potential of screw dislocations in  $\alpha - Fe$  from first principles: cluster versus dipole approaches*. J. Comput-aided Mater. Des. 2007. 14: p. 85.
- [78] Groger, R., Bailey, A. G. and Vitek, V., *Multiscale modeling of plastic deformation of molybdenum and tungsten: I. Atomistic studies of the core structure and glide of  $\frac{1}{2} < 111 >$  screw dislocations at 0 K*. Acta Mater, 2008. 56: p. 5401.
- [79] Groger, R., Racherla, V., Bassani, J. L. and Vitek, V., *Multiscale modeling of plastic deformation of molybdenum and tungsten: II. Yield criterion for single crystals based on atomistic studies of glide of  $\frac{1}{2} < 111 >$  screw dislocations*. Acta Mater, 2008. 56: p. 5412.
- [80] Groger, R. and Vitek, V., *Multiscale modeling of plastic deformation of molybdenum and tungsten. III. Effects of temperature and plastic strain rate*. Acta Mater, 2008. 56: p. 5426.
- [81] Clouet, E., Ventelon, L. and Willaime, F., *Dislocation Core Energies and Core Fields from First Principles*. Phys. Rev. Lett. 2009. 102: p. 055502.

- [82] Ventelon L., Ph.D. Universit Claude Bernard, Lyon, November 2008.
- [83] Frederiksen, S. L. and Jacobsen K. W., *Density functional theory studies of screw dislocation core structures in bcc metals*. Philos. Mag., 2003. 83: p. 365.
- [84] Proville, L., Ventelon, L. and Rodney, D., *Prediction of the kink-pair formation enthalpy on screw dislocations in  $\alpha$ -iron by a line tension model parametrized on empirical potentials and first-principles calculations*. Phys. Rev. B, 2013. 87: P. 144106.
- [85] Caillard, D., *Kinetics of dislocations in pure Fe. Part I. In situ straining experiments at room temperature*. Acta Mater., 2010. 58.9: p. 3493.
- [86] Quenel, D.J., Sato, A. and Meshii, M., *Solution softening and hardening in the Iron-Carbon system*. Mater. Sci. Eng., 1975. 18: p. 199.
- [87] Kuramoto, E., Aono, Y. and Kitajima, K., *Thermally activated slip deformation of high purity iron single crystals between 4.2 K and 300 K*. Scripta Met., 1979. 13: p. 1039.
- [88] Brunner D, Diehl J. *The Effect of Atomic Lattice Defects on the Softening Phenomena of High-Purity  $\alpha$ -Iron*. Phys. Stat. Sol. A, 1997. p. 160.
- [89] Takeuchi, S., *Core structure of a screw dislocation in the b.c.c. lattice and its relation to slip behaviour of  $\alpha$ -iron*. Philos. Mag. A, 1979. 39: p. 661.
- [90] Koizumi, H., Kirschner, H.O.K. and Suzuki, T., *Kink pair nucleation and critical shear stress*. Acta Met. Mater. 1993. 41: p. 3483.
- [91] Caillard, D., Martin, J. L. and Cahn, R. W. (ed.), *Thermally activated mechanisms in crystal plasticity. Pergamon materials series*. Pergamon materials series, Amsterdam., 2003.
- [92] Gröger, R. and Vitek, V., *Explanation of the discrepancy between the measured and atomistically calculated yield stresses in body-centred cubic metals*. Philos. Mag. Lett. 2007. 87: p. 113.
- [93] Furubayashi E., *Behavior of Dislocations in Fe-3% Si under Stress*. J. Phys. Soc. Japan., 1969. 27: p. 130.

- [94] Kubin, L. P. and Louchet, F., *Analysis of softening in the Fe-C system from in situ and conventional experiments-I. In situ experiments*. Acta Met., 1979. 27: p. 337.
- [95] Ikeno, S. and Furubayashi, E., *Dislocation Behavior in Pure Niobium at Low Temperatures*. Phys. Stat. Sol.A, 1975. 27: p. 581.
- [96] Louchet, F., Kubin, L. P. and Vesely, D., *In situ deformation of b.c.c. crystals at low temperatures in a high-voltage electron microscope. Dislocation mechanisms and strain-rate equation*. Philos. Mag. A, 1979. 39: p. 433.
- [97] Caillard, D., *TEM in situ straining experiments in Fe at low temperature*. Philos. Mag. Lett., 2009. 89: p. 517.
- [98] Proville, L., Rodney, D. and Marinica, M. C., *Quantum effect on thermally activated glide of dislocations*. Nat. Mater., 2012. 11: p. 845.
- [99] Gordon, P. A., Neeraj, T. and Mendeleev, M. I., *Screw dislocation mobility in BCC Metals: a refined potential description for  $\alpha$ -Fe* Phil. Mag. Lett., 2011. 91: p. 3931.
- [100] Caillard, D., *Kinetics of dislocations in pure Fe. Part II. In situ straining experiments at low temperature*. Acta Mater., 2010. 58.9: p. 3504.
- [101] Barvinschi, B., Proville, L., and Rodney, D., *Quantum Peierls stress of straight and kinked dislocations and effect of non-glide stresses*. Mater. Sci. Eng., 2014. 22: p. 025006.
- [102] Ceperley, David M., and B. J. Alder. *Ground State of the Electron Gas by a Stochastic Method*. Phys. Rev. Lett., 1980. 45(7): p. 566.
- [103] Kohn W. and Sham, L. J., *Self-Consistent Equations Including Exchange and Correlation Effects*. Phys. Rev. 140., 1965. 4A: p. A1133.
- [104] Frederiksen, S. L., and Jacobsen, K. W., *Density functional theory studies of screw dislocation core structures in bcc metals*. Philos. Mag., 2003. 83: p. 365.
- [105] Ventelon, L., Willaime, F., and Leyronnas, P., *Atomistic simulation of single kinks of screw dislocations in  $\alpha$ -Fe*. J. Nucl. Mat., 2009. 386: p. 26.

- [106] Lennard-Jones, J. E., *Cohesion*. Proc. Phys. Soc., 1931. 43: p. 461
- [107] Chamati, H., Papanicolaou, N. I., Mishin, Y., and Papaconstantopoulos, D. A. *Embedded-atom potential for Fe and its application to self-diffusion on Fe(100)*. Surf. Sci., 2006. 600: p. 1793.
- [108] <http://lammmps.sandia.gov/>
- [109] Bangwei, Z., Yifang, O., Shuzhi, L., and Zhanpeng, J., *An analytic MEAM model for all BCC transition metals*. Physica B: Cond. Matt., 1999. 262(I:3-4): p. 218.
- [110] Daw, M. S., Foiles, S. M., and Baskes, M. I., *The embedded-atom method: a review of theory and applications*. Mater. Sci. Reports., 1993. 9: p. 251.
- [111] Ercolessi, F., and Adams, J. B., *Interatomic Potentials from First-Principles Calculations: The Force-Matching Method*. Europhys. Lett., 1994. 26(8): p. 583.
- [112] Rodney, D., Ventelon, L., Clouet, E., Pizzagalli, L., and Willaime, F., *Ab initio modeling of dislocation core properties in metals and semiconductors*. Acta Materialia., 2017. 124: p. 633.
- [113] Hirth, J. P., and Lothe, J., *Theory of Dislocations*, 2nd ed., Wiley, New York., 1982.
- [114] Bacon, D. J., Barnett, D. M., and Scattergood, R. O., *Anisotropic continuum theory of lattice defects*. Prog. Mater. Sci., 1980. 23, p. 51.
- [115] Shenoy, V. B., and Phillips, R., *Finite-sized atomistic simulations of screw dislocations*. Philos. Mag. A., 1997. 76: p. 367.
- [116] Pizzagalli, L., and Beauchamp, P., *First principles determination of the Peierls stress of the shuffle screw dislocation in silicon*. Philos. Mag. Lett., 2004. 84: p. 729.
- [117] Woodward, C., *First-principles simulations of dislocation cores*. Mater. Sci. Eng. A, 2005. 400-401: P.59.

- [118] Sinclair, J. E., Gehlen, P. C., Hoagland, R. G., and Hirth, J. P., *Flexible boundary conditions and nonlinear geometric effects in atomic dislocation modeling*. J. Appl. Phys. 1978. 49: p. 3890.
- [119] Liu, Y., Lu, G., Chen, Z., and Kioussis, N., *An improved QM/MM approach for metals*. Model. Simul. Mater. Sci. Eng., 2007. 15: p. 275.
- [120] Chen, Z., Lu, G., Kioussis, N., and Ghoniem, N., *Effect of the local environment on the mobility of dislocations in refractory bcc metals: Concurrent multiscale approach*. Phys. Rev. B., 2008. 78: p. 134102.
- [121] Segall, D. E., Strachan, A., Goddard III, W. A., Ismail-Beigi, S., and Arias, T. A., *Ab initio and finite-temperature molecular dynamics studies of lattice resistance in tantalum*. Phys. Rev. B., 2003. 6:, p. 014104.
- [122] Clouet, E., Ventelon, L., and Willaime, F., *Dislocation Core Energies and Core Fields from First Principles*. Phys. Rev. Lett., 2009. 102: p. 055502.
- [123] Ismail-Beigi, S., and Arias, T. A., *Ab Initio Study of Screw Dislocations in Mo and Ta: A New Picture of Plasticity in bcc Transition Metals*. Phys. Rev. Lett., 2000. 84: p. 1499.
- [124] Blase, X., Lin, K., Canning, A., Louie, S. G., and Chrzan, D. C., *Structure and Energy of the 90° Partial Dislocation in Diamond: A Combined Ab Initio and Elasticity Theory Analysis*. Phys. Rev. Lett., 2000. 84: p. 5780.
- [125] Cai, W., Bulatov, V. V., Chang, J., Li, J., and Yip, S., *Anisotropic elastic interactions of a periodic dislocation array*. Phys. Rev. Lett., 2001. 86(25): p. 5727.
- [126] Rodney, D., *Molecular dynamics simulation of screw dislocations interacting with interstitial frank loops in a model FCC crystal*. Acta Mater., 2004. 52: p. 607.
- [127] Bacon, D. J., Osetsky, Y., and Rodney, D., *Chapter 88. Dislocation-Obstacle Interactions at the Atomic Level*. Dislocations in solids, 2009. 15: p. 1.
- [128] Patinet, S., and Proville, L., *Depinning transition for a screw dislocation in a model solid solution*. Phys. Rev. B, 2008. 78: p. 104109.

- [129] Rodney, D., and Proville, L., *Stress-dependent Peierls potential: Influence on kink-pair activation*. Phys. Rev. B, 2009. 79: p. 094108.
- [130] Rodney, D., and Martin, G., *Dislocation pinning by glissile interstitial loops in a nickel crystal: A molecular-dynamics study*. Phys. Rev. B, 2000. 61: p. 8714.
- [131] Rodney, D., *Nuclear Instruments and Methods in Physics Research Section B: Beam Interactions with Materials and Atoms*. Phys. Res. Sect. B, 2005. 228(1-4): p. 100.
- [132] Swope, W. C., Andersen, H. C., Berens, P. H., and Wilson, K. R., *A computer simulation method for the calculation of equilibrium constants for the formation of physical clusters of molecules: Application to small water clusters*. J. Chem. Phys., 1982. 76: p. 637.
- [133] Henkelman G., Jóhannesson G., and Jónsson H., *Methods for Finding Saddle Points and Minimum Energy Paths*. Theor. Methods in Cond. Phase Chem. Springer, Dordrecht., 2002. 5: p. 269.
- [134] Sheppard, D., Terrell, R., and Henkelman, G., *Optimization methods for finding minimum energy paths*. The Journal of Chemical Physics., 2008. 128: p. 134106.
- [135] Peach, M., and Koehler, J. S., *The Forces Exerted on Dislocations and the Stress Fields Produced by Them*. Phys. Rev., 1950. 80(3): p. 436.
- [136] Leibfried, G., *Über den Einfluß thermisch angeregter Schallwellen auf die plastische Deformation*. Zeitschrift für Physik, 1950. 127(4): p. 344.
- [137] Bitzek, E., and Gumbusch, P., *Dynamic aspects of dislocation motion: atomistic simulations*. Mat. Sci and Eng. A., 2005. 400-401: p. 40.
- [138] Angelo, J. E., Moody, N. R., and Baskes, M. I., *Trapping of hydrogen to lattice defects in nickel*. Modell. Simul. Mater. Sci. Eng., 1995. 3: p. 289.
- [139] Mishin, Y., *Atomistic modeling of the  $\gamma$  and  $\gamma'$ -phases of the NiAl system*. Acta Metall., 2004. 52: p. 1451.

- [140] Olmsted, D. L., Hector Jr, L. G., Curtin, W. A., and Clifton, R. J., *Atomistic simulations of dislocation mobility in Al, Ni and Al/Mg alloys*. Modelling Simul. Mater. Sci. Eng., 2005. 13: p. 371.
- [141] Frenkel, J. and Kontorova, T., Phys. Z. Sowjetunion., 1938. 13: p. 1.
- [142] Joós, B., *Properties of solitons in the Frenkel-Kontorova model*. Solid State Commun. 1982. 42: p. 709.
- [143] Joós, B. and Duesbery, M. S., *Dislocation kink migration energies and the Frenkel-Kontorova model*. Phys. Rev. B., 1997. 55: p. 11161.
- [144] Braun, O. M. and Kivshar, Y. S., *Nonlinear dynamics of the Frenkel-Kontorova model*. Physical Reports., 1998. 306: p. 1.
- [145] Swinburne, T. D., Dudarev, S. L., Fitzgerald, S. P., Gilbert, M. R. and Sutton, A. P., *Theory and simulation of the diffusion of kinks on dislocations in bcc metals*. Phys. Rev. B., 2013. 87: p. 064108.
- [146] Scott, A., Encyclopedia of Nonlinear Science., 2004.
- [147] Dorn, J.E. et al., Trans. metall. Soc. AIME, 1964. 230: p. 1052.
- [148] Guyot, P., and Dorn, J. E., *A critical review of the Peierls mechanism*. Canadian Journal of Physics., 1967. 45(2): p. 983.
- [149] Queyreau, S., Marian, J., Gilbert, M. R., and Wirth, B. D., *Edge dislocation mobilities in bcc Fe obtained by molecular dynamics*. Phys. Rev. B., 2011. 84: p. 064106.
- [150] Monnet, G., and Terentyev, D., *Structure and mobility of the  $\frac{1}{2} \langle 111 \rangle (11\bar{2})$  edge dislocation in BCC iron studied by molecular dynamics*. Acta Mater., 2009. 57: p. 1416.
- [151] Gilbert, M. R., Queyreau, S., and Marian, J., *Stress and temperature dependence of screw dislocation mobility in  $\alpha$ -Fe by molecular dynamics*. Phys. Rev. B, 2011. 84: p. 174103.
- [152] Rassoulinejad-Mousavi, S. M. et al., Sci. Reports., 2008. 8: p. 2424.

- [153] Caillard, D., *Geometry and kinetics of glide of screw dislocations in tungsten between 95 K and 573 K*. Acta Materialia., 2018. 161: p. 21.
- [154] Marinica, M. C., Ventelon, L., Gilbert, M. R., Proville, L., Dudarev, S. L., Marian, J. and Willaime, F., *Interatomic potentials for modelling radiation defects and dislocations in tungsten*. Journal of Physics: Condensed Matter., 2013. 25(39): p. 395502.
- [155] Finnis, M. W. and Sinclair, J. E., *A simple empirical n-body potential for transition metals*. Phil. Mag. A, 1984. 50: p. 45.
- [156] Ackland, G. J. and Thetford, R., *An improved n-body semi-empirical model for body-centred cubic transition metals*. Phil. Mag. A, 1987. 56: p. 15.
- [157] Juslin, N. and Wirth, B. D., *Interatomic potentials for simulation of He bubble formation in W*. J. Nucl. Mater., 2013. 432: p. 61.
- [158] Wang, Y. R. and Boercker, D. B., *Effective interatomic potential for body-centered-cubic metals*. J. Appl. Phys., 1995. 78: p. 122.
- [159] Derlet, P. M., Nguyen-Manh, D. and Dudarev, S. L., *Multiscale modeling of crowdion and vacancy defects in body-centered-cubic transition metals*. Phys. Rev. B, 2007. 76: p. 5.
- [160] Ventelon, L., Clouet, E., Willaime, F. and Rodney, D., *Ab initio investigation of the Peierls potential of screw dislocations in BCC Fe and W*. Acta Mater., 2013. 61: p. 3973.
- [161] Garlick, R. G. and Probst, H. B., *Investigation of room-temperature slip in zone-melted tungsten single crystals*. Trans. AIME, 1964. 230: p. 1120.
- [162] Schadler, H. W., *Deformation behaviour of zone-melted tungsten single crystals*. Trans. AIME, 1960. 218: p. 649.
- [163] Li, H., Wurster, S., Motz, C., Romaner, L., Ambrosch-Draxl, C. and Pippan, R., *Dislocation-core symmetry and slip planes in tungsten alloys: ab initio calculations and microcantilever bending experiments*. Acta Mater., 2012. 60: p. 748.

- [164] Brunner, D., *Comparison of flow stress measurements on high-purity tungsten single crystals with the kink-pair theory*. Mater. Trans., 2000. JIM 41: p. 152.
- [165] Argon, A. S. and Maloof, S.R., *Plastic deformation of tungsten single crystals at low temperatures* Acta Metall., 1966. 14: p. 1449.

**Titre :** Statistiques du glissement des dislocations à basse température dans les métaux de symétrie cubique centrée.

**Mots clés :** Plasticité cristalline, mouvement saccadé, basse température, déformation plastique

**Résumé :** Les observations de microscopie électronique in situ effectuées par Daniel Caillard (CEMES, Toulouse) au cours de la déformation de cristaux de symétrie cubique centrée ont montré que les dislocations vis effectuaient des sauts de plusieurs distances inter-atomiques alors que la théorie standard de Peierls prédit des sauts de une seule distance inter-atomique. Nous avons étudié par simulation atomique le glissement d'une dislocation vis dans un cristal de fer pur.

Nous montrons que la propagation de décrochement le long de la dislocation induit un échauffement local qui favorise la nucleation de décrochements supplémentaires. L'accumulation de ces décrochements permet à la dislocation de parcourir plusieurs distances inter-atomiques. Ces simulations nous permettent de proposer une théorie pour l'explication des observations de D. Caillard.

**Title :** Statistics of dislocations at low temperature in pure metals with body centered cubic symmetry.

**Keywords :** Crystal plasticity, jerky motion, low temperature, plastic deformation

**Abstract :** In situ straining tests in high purity  $\alpha$ -Fe thin-foils at low temperatures have demonstrated that crystalline defects, called dislocations, have a jerky type of motion made of intermittent long jumps of several nanometers. Such an observation is in conflict with the standard Peierls mechanism for plastic deformation in bcc crystals, where the screw dislocation jumps are limited by inter-reticular distances, i.e. of a few Angstroms. Employing atomic-scale simulations, we show that although the short jumps are initially more

favorable, their realization requires the propagation of a kinked profile along the dislocation line which yields coherent atomic vibrations acting as traveling thermal spikes. Such local heat bursts favor the thermally assisted nucleation of new kinks in the wake of primary ones. The accumulation of new kinks leads to long dislocation jumps like those observed experimentally. Our study constitutes an important step toward predictive atomic-scale theory for materials deformation.

